DEFINING THE UNKNOWNS OF SONOLUMINESCENCE

Bradley P. BARBER[a], Robert A. HILLER[b], Ritva LÖFSTEDT[c], Seth J. PUTTERMAN[b], Keith R. WENINGER[b]

[a] *Lucent Technologies, Murray Hill, NJ 07974, USA*
[b] *Physics Department, University of California, Los Angeles, CA 90095, USA*
[c] *Institute for Theoretical Physics, University of California, Santa Barbara, CA 93106, USA*

ELSEVIER

AMSTERDAM – LAUSANNE – NEW YORK – OXFORD – SHANNON – TOKYO

ELSEVIER

Physics Reports 281 (1997) 65–143

PHYSICS REPORTS

Defining the unknowns of sonoluminescence

Bradley P. Barber[a], Robert A. Hiller[b], Ritva Löfstedt[c], Seth J. Putterman[b], Keith R. Weninger[b]

[a] *Lucent Technologies, Murray Hill, NJ 07974, USA*

[b] *Physics Department, University of California, Los Angeles, CA 90095, USA*

[c] *Institute for Theoretical Physics, University of California, Santa Barbara, CA 93106, USA*

Received November 1996; editor: A.A. Maradudin

Contents:

1. Why is sonoluminescence interesting? 68
2. How does one produce a sonoluminescing bubble? 70
3. How does one measure the bubble motion? 74
4. How does one describe the bubble dynamics? 80
5. Why is a small percentage of noble gas essential to stable, visible sonoluminescence? 92
6. What determines the ambient radius? 95
7. Why is water the friendliest fluid for sonoluminescence? 107
8. How energetic are the emitted photons? 116
9. How short are the flashes? 121
10. What is the light-emitting mechanism? 123
11. How spherical is the collapse? 129
12. How controllable are experiments on sonoluminescence? 136

References 141

PII S0370-1573(96)00050-6

Abstract

As the intensity of a standing sound wave is increased the pulsations of a bubble of gas trapped at a velocity node attain sufficient amplitude so as to emit picosecond flashes of light with a broadband spectrum that increases into the ultraviolet. The acoustic resonator can be tuned so that the flashes of light occur with a clocklike regularity: one flash for each cycle of sound with a jitter in the time between flashes that is also measured in picoseconds. This phenomenon (sonoluminescence or "SL") is remarkable because it is the only means of generating picosecond flashes of light that does not use a laser and the input acoustic energy density must be concentrated by twelve orders of magnitude in order to produce light. Light scattering measurements indicate that the bubble wall is collapsing at more than 4 times the ambient speed of sound in the gas just prior to the light emitting moment when the gas has been compressed to a density determined by its van der Waals hard core. Experiments indicate that the collapse is remarkably spherical, water is the best fluid for SL, some noble gas is essential for stable SL, and that the light intensity increases as the ambient temperature is lowered. In the extremely stable experimental configuration consisting of an air bubble in water, measurements indicate that the bubble chooses an ambient radius that is not explained by mass diffusion. Experiments have not yet been able to map out the complete spectrum because above 6 eV it is obscured by the cutoff imposed by water, and furthermore experiments have only determined an upper bound on the flash widths. In addition to the above puzzles, the theory for the light emitting mechanism is still open. The scenario of a supersonic bubble collapse launching an imploding shock wave which ionizes the bubble contents so as to cause it to emit Bremsstrahlung radiation is the best candidate theory but it has not been shown how to extract from it the richness of this phenomenon. Most exciting is the issue of whether SL is a classical effect or whether Planck's constant should be invoked to explain how energy which enters a medium at the macroscopic scale holds together and focuses so as to be emitted at the microscopic scale.

PACS: 78.60.Mq; 43.35.-c
Keywords: Sonoluminescence; Bubble dynamics; Bremsstrahlung

1. Why is sonoluminescence interesting?

The equations of fluid mechanics (Landau and Lifshitz, 1987) describe an extraordinarily wide range of phenomena. These include the behavior of sound waves and surface waves, the formation of shock fronts, the localization of energy in solitons (Dodd et al., 1982; Wu et al., 1984), the randomization of energy in the transition to turbulence, and pattern formation, such as observed in convection cells (Cross and Hohenberg, 1993). Among fluid phenomena sonoluminescence (SL), the transduction of sound into light is unique in that the energy enters the fluid at low energy and long wavelengths, where the equations of fluid mechanics apply, but the resulting fluid mechanical motion sets up a transformation of the sound energy into degrees of freedom, visible photons, which are not describable by the original equations of fluid mechanics. In sonoluminescence, the sound energy is concentrated by twelve orders of magnitude and emitted as a flash of light.

Fig. 1 displays the extraordinary range of length and time scales characterizing SL. Trace "b" is the sound field near the center of a flask containing partially degassed water, driven (sinusoidally) at its acoustic resonance (which is here about 26 kHz). The acoustic radiation pressure (King, 1934) of the sound field traps a gas bubble at the pressure antinode in the center of the flask where it pulsates in response to the pressure swings of the drive. These pulsations are displayed in trace "a", which shows

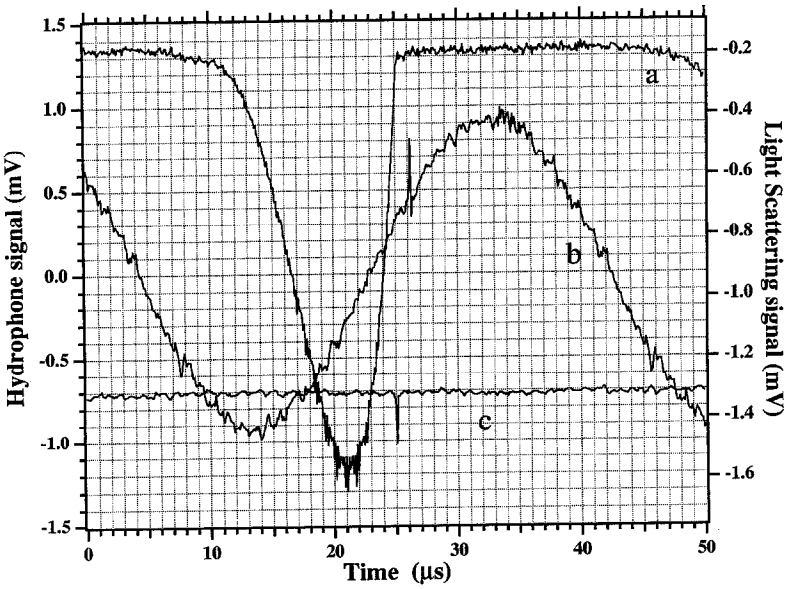

Fig. 1. Relative timing of sonoluminescence (c) from the stressed interior of a collapsing air bubble whose radius squared is proportional to the magnitude of the intensity of scattered laser light (a). The high pressures reached during the collapse launch an outgoing spike recorded by a microphone that measures the driving sound field (b) inside the acoustic resonator. The scale for SL has been offset and the phase of the 26 kHz sound wave has been shifted by 3 μs to correct for the phase delay introduced by the AC-coupled preamplifier. The needle microphone is located about one mm from the bubble, and this accounts for the 1 μs delay between the flash of light and the spike. The flash of SL is less than 50 ps long, and the spike is less than 20 ns wide. The maximum radius of the bubble is about 45 μm and the amplitude of the sound field is about 1.2 atm. This process repeats with each cycle of sound. For an air bubble in water each flash of SL yields about 2×10^5 photons.

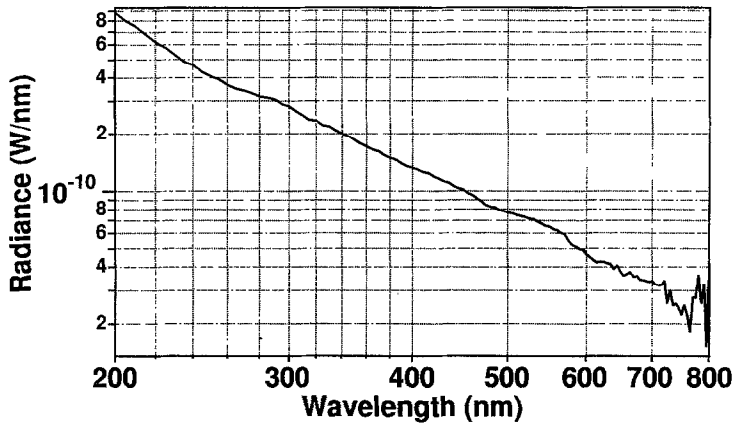

Fig. 2. Spectrum of light emitted by a sonoluminescing bubble of ^{4}He gas, which is formed from water with helium gas dissolved at a partial pressure of 150 mm. The high-energy cutoff at 6 eV (200 nm) is due to the transmission cutoff imposed by water. How far the energy focusing extends beyond 6 eV is a major unknown. The measured spectrum has been corrected for the attenuation of light by the flask and the water, and for the quantum efficiency of the photodetector and spectrometer. The resolution is 10 nm FWHM.

the amount of light scattered out of a laser beam trained on the bubble (Barber and Putterman, 1992). The larger the negative signal, the larger is the bubble radius. The expansion of the bubble from its ambient radius (~ 4.5 μm) occurs on hydrodynamic time scales during the rarefaction half-cycle of the pressure swing. It brings the bubble to its maximum radius of about 45 μm. The ensuing collapse accelerates the bubble wall to supersonic velocities and compresses the bubble's interior (Barber et al., 1994). By mechanisms yet unknown, the high stresses and high energy densities inside the bubble generated by this collapse result in the emission of a flash of light (in trace "c"). The high pressures built up inside the bubble during the collapse launch an outgoing acoustic pulse (Barber et al., 1997), which is the spike riding the sound field in trace "b". Plotted on this hydrodynamic timescale, the flash of light and the acoustic spike are deltafunctions and the collapsing radius is a theta function. To the best of our resolution, which has only established upper bounds, the light flash is less than 50 ps in duration and it occurs within 0.5 ns of the minimum bubble radius (Barber et al., 1992, 1997). The SL flashwidth is thus 100 times shorter than the shortest (visible) lifetime of an excited state of a hydrogen atom. Each flash is roughly spherically symmetric and contains about one million photons (Barber and Putterman, 1991). The outgoing acoustic spike is less than 20 ns wide and the collapse velocity is over 1.4 km/s (or four times the ambient speed of sound in the gas, $c_0 = 3.3 \times 10^4$ cm/s) (Barber et al., 1997). This violent bubble motion and resultant light emission repeat in clocklike synchronicity with the sound field; each acoustic cycle yields one flash of light, and the jitter in time between consecutive flashes can be made less than 50 ps (Barber et al., 1992). The unaided eye can easily see the sonoluminescing bubble as a steady starlike light.

Fig. 2 shows the spectrum (Hiller et al., 1992) of the light emitted by a helium bubble in water at 0°C with helium dissolved in it at a partial pressure of 150 Torr. The broadband, featureless spectrum extends into the ultraviolet; higher-frequency electromagnetic radiation cannot propagate through water. The extent of the energy focusing achieved in SL is estimated by comparing the average acoustic energy delivered to an atom of the fluid by the sound field, $\langle \rho v^2 \rangle \cdot (\text{volume/atom}) \approx$

4×10^{-12} eV/atom, where ρ is the density of water and v is the velocity amplitude in response to the sound wave, to the most energetic of the observed photons, which have an energy of 6 eV. Assuming that the light emission stems from a region of atomic dimensions, one is led to interpret SL as a process where the energy concentration spans twelve orders of magnitude (Barber et al., 1991). (Here we used a pressure amplitude of one atm, so that the rms Mach number, $M = v/c = 10^{-5}$, where the velocity of sound in water is $c = 1.482 \times 10^5$ cm/s at 20°C and 1.403×10^5 cm/s at 0°C.) Noting that 1 eV = 11 600 K and that spectral lines have yet to be observed we conclude that the region from which the broadband 6 eV radiation is originating is very hot and very stressed.

In order to study the properties of an audible sound field we have had to use photodetectors which are faster than those used in elementary-particle experiments. Not only is this mixing of macroscopic and microscopic regimes interesting physics, but an understanding of SL might reveal a useful paradigm for energy-concentrating phenomena, and since the wavelength of the outgoing light is larger than the light-emitting region inside the collapsed bubble (of radius ~ 0.5 μm) some type of photon correlation might be present in SL. Our attempts to characterize this phenomenon have led us to pose the following questions and experimental challenges which we will discuss, but not resolve, in this review.

- Why is SL so sensitive to the temperature of the fluid, the light intensity increasing a hundredfold when the temperature is decreased from 40°C to 0°C?
- Why is water the friendliest fluid for SL?
- Why are noble gases so essential for producing stable, bright bubbles? Why do pure diatomic gas bubbles jitter and give such dim light?
- What determines the radius of the SL bubble?
- What determines the upper and lower sound pressure thresholds between which one can observe SL?
- How can one measure a time-resolved spectrum of the light emission?
- Can one measure the spectrum of SL beyond the ultraviolet cutoff of water?
- What is the limit of the energy focusing that can be achieved with SL?
- What is the light-emitting mechanism?

2. How does one produce a sonoluminescing bubble?

An overview of the basic SL apparatus is shown in Fig. 3 (Gaitan, 1990; Hiller and Barber, 1995). An oscillating voltage across a piezoelectric ceramic (PZT) causes it to vibrate and acts as a transducer to drive the water-filled flask at an acoustic resonance. The lowest breathing mode of a spherical resonator is described by $\varphi = j_0(kr)$, where φ is the velocity potential such that $v = \nabla\varphi$ and j_0 is the spherical Bessel function. The wavenumber k is chosen to satisfy the pressure-release boundary condition presented by the air-glass interface, viz. $\varphi(R_f) = 0$, where R_f is the radius of the flask. This solution is perturbed slightly by the differences in acoustic impedance between the fluid and the glass. In this geometry, a gas bubble in the water will be forced to the pressure antinode at the center of the flask by the acoustic radiation pressure of a sufficiently intense sound field (Löfstedt et al., 1995). The second spherically symmetric resonance of the flask creates a spherical velocity-nodal shell which can trap many bubbles at once. This shell is located at about $0.7R_f$ and appears when $kR_f = 2\pi$. The corresponding resonance frequency ω_a is determined by $\omega_a/k = c$.

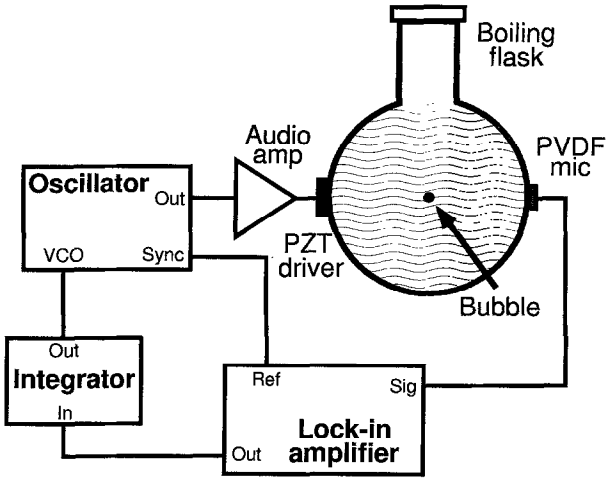

Fig. 3. Basic apparatus for generating and modelocking sonoluminescence. The amplified output of a sine-wave generator drives a water-filled flask at resonance so that a trapped bubble of gas pulsates at sufficient amplitude to generate light. The modelocking circuit tracks the resonance.

At the lowest acoustic drive level at which a bubble is trapped, the bubble will slowly dissolve away. At higher drive levels, the trapped bubble is stable against dissolution but emits no light. Still higher drive levels are the parameter space for stable SL: the bubble suddenly shrinks in size and emits light. Increasing the drive level leads to more intense light emission. Eventually an upper drive threshold is reached, at which pressure the sonoluminescing bubble will abruptly disappear (Gaitan, 1990; Barber and Putterman, 1991). Sometimes, the abrupt upper threshold is replaced by the tendency for the bubble to wander away from the center of the flask with increasing drive levels; whether this is a property of the specific resonator design is unknown.

The resonant frequency of the flask is determined by searching for peaks in the amplitude of the sound field in the flask by means of a microphone, or by tracking the phase difference between voltage and current of the PZT (Barber, 1992). Various spurious resonances, such as flexing modes of the glass flask do not trap a bubble. Variations in the ambient temperature of a few degrees Celsius correspond to shifts in the resonant frequency by 200 Hz which is larger than the width of the resonance of a typical flask. The drive frequency may be continuously adjusted to accommodate such changes in the resonance by using a mode-locking scheme, as shown in Fig. 3 (Hiller, 1995). Underlying the operation of such a method is the fact that the phase of the response of an oscillator relative to a sinusoidal drive shifts by π as the frequency is tuned through resonance. At low frequencies of drive the response is dominated by the spring constant so that it is "in" phase, whereas at high frequency the response is dominated by inertia and is therefore "out" of phase with the drive. The phase shift occurs over a frequency range determined by the damping coefficient of the oscillator. To maintain SL as the drive frequency drifts off resonance, the phase difference between the output of the signal generator, which drives the PZT, and the standing wave in the resonator, as measured by a PVDF microphone, is determined by means of a lock-in amplifier. This phase difference is integrated and used as the voltage-controlled oscillator input to the signal generator. The quality factor of a typical SL apparatus is between 300 and 1500 (Barber and Putterman, 1991). Typical voltages across the PZT required to drive the acoustic resonance and sustain a sonoluminescing bubble are 50 to 150

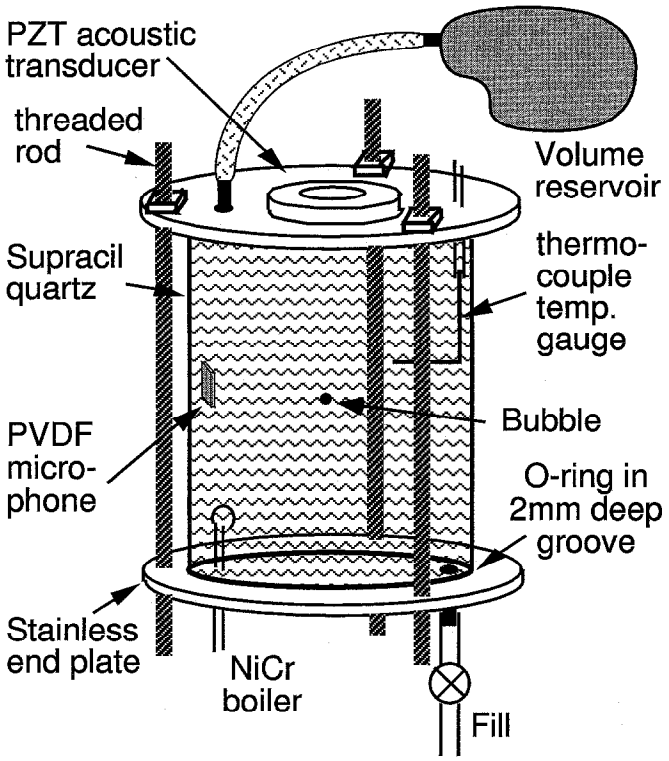

Fig. 4. Cylindrical resonator for obtaining sonoluminescence from a sealed system. This is important for controlling the composition and the partial pressure of the gas content in the resonator. The NiCr (toaster) wire is used to seed a bubble by boiling the liquid locally. The vaporous cavity fills with whatever gas is dissolved in the liquid and is at the same time yanked to the velocity node of the sound field where it emits light at a sufficiently high acoustic drive.

V (which can be generated easily, but expensively, with high voltage linear amplifiers). Alternatively, impedance-matching the capacitance-dominated PZT with inductors allows the SL cell to be driven with less than 10 V (Barber, 1992).

A spherical flask such as the one in Fig. 3 can be seeded with bubbles by simply poking the open surface. However, the quality of the resonance is very sensitive to the level of fluid in the neck. Achieving some degree of experimental reproducibility requires a sealed system, which allows the liquid and the gas contents to be controlled accurately. Such a system is shown in Fig. 4, where a sealed cylindrical resonator is driven by piezoelectrics mounted on the steel endcaps (Hiller et al., 1994). In this apparatus the free surface is eliminated by filling the system entirely; changes in density are accommodated by a variable volume which is provided by a polyethylene bag. The bubble is seeded by passing a brief current through a loop of NiCr wire, which boils the surrounding fluid, leaving vaporous bubbles, into which flows the gas dissolved in the fluid. These gas bubbles are then carried to the pressure antinode by acoustic radiation pressure, where they coalesce into a single bubble. The ambient fluid temperature is measured by means of thermocouple gauges.

The fill lines of the resonator are connected to the gas manifold shown in Fig. 5 (Battino et al., 1972; Hiller, 1995). The designated fluid is degassed to tens of millitorr of partial pressure of

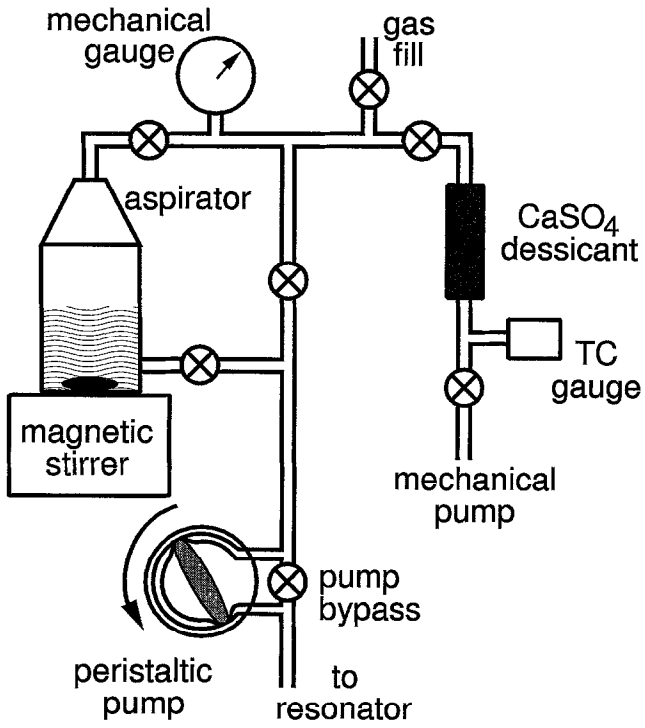

Fig. 5. Gas manifold apparatus used for the purpose of degassing water or another liquid and then preparing it with a desired partial pressure of a particular gas mixture.

gas (plus the vapor pressure) by means of a mechanical pump. A magnetic stirrer accelerates the degassing by creating turbulent voids which increase the area of the fluid/gas interface. The chosen gas mixture is prepared in a large reservoir, and admitted to the degassed fluid through the gas fill line at the chosen pressure. Stirring the fluid accelerates the establishment of equilibrium between the gas dissolved in the fluid and the gas pressure above it. Although equilibrium appears to be established in less than 5 min we stir for about 20 min. The fluid finally pumped into the SL resonator has a partial pressure of gas dissolved in it which is accurate to about 1/2 Torr.

The modal structure which can trap bubbles in the cylindrical cell in Fig. 4 are approximated by the pressure amplitudes

$$P_a = P'_a J_0(k_n r)\cos(2q\pi z/H)\cos(\omega_a t)$$

where H is the height of the cylinder and

$$\omega_a^2 = c^2\left(k_n^2 + \frac{4q^2\pi^2}{H^2}\right)$$

and the surface of the cylinder is taken as a pressure node, so that $J_0(k_n R_f) = 0$, and the z dependence has been chosen so that $z = 0$, $+H/2$, and $-H/2$, are all velocity nodes. This fixes q to be an integer,

as can be seen from the velocity potential, φ, which is related to the pressure by

$$P_a = -\rho \partial \varphi / \partial t.$$

3. How does one measure the bubble motion?

Underlying SL is a small bubble whose pulsations absorb the long-wavelength sound energy during half of the sound cycle and then quickly concentrate it so as to emit a flash of light. The dynamics of this bubble, in particular its radius as a function of time, $R(t)$, constitute an essential parameter in characterizing SL. The experimental impediments to overcome in measuring the radius include the wide range of timescales of the bubble motion ($\sim$ 10 μs for the absorption of energy to sub-nanosecond for the collapse) and the fact that the bubble's radius ranges from 50 μm at its maximum to 1/2 μm, the wavelength of visible light, at its minimum (Barber and Putterman, 1992). The features of SL which come to the experimentalist's aid in determining $R(t)$ include the flash of light which accompanies each cycle of the sound field. The flash can be used to set the zero of time for the purpose of averaging several acquisitions and reducing the noise level. As mentioned above, the light flash comes at the same point in every cycle and these cycles repeat with a clocklike synchronicity (Barber et al., 1992).

Mie scattering has proven to be a valuable and versatile technique for measuring $R(t)$ (van de Hulst, 1957; Dave, 1969; Kerker, 1969; Marston 1979, 1991; Wiscombe, 1980; Hansen, 1985; Gaitan, 1990; Barber and Putterman, 1992; Holt and Crum, 1992). In this approach laser light with a beam width larger than the bubble's radius is trained on the bubble. In the classical, or ray optics limit, the light scattered within a given angle is simply proportional to $R^2(t)$. Since the voltage on the photodetector is proportional to the intensity of the scattered light, the square root of this signal is proportional to R. This scattered light is also proportional to the difference in the dielectric constant at the gas-fluid interface presented by the surface of the bubble. Surprisingly, as the size of the bubble is increased, the ray optics limit is approached only very slowly. As shown in Fig. 6, for a bubble of radius 20 μm, the light scattered within a specific angle displays many diffraction peaks which can be seen straddling the classical limit (solid line). The signal is clearly very sensitive to angular alignment. Experimentally we converge on the classical limit by collecting the scattered light from a range of angles, typically 25° around 60° from the forward direction, which averages out the fringes, as shown in Fig. 6.

A Mie scattering apparatus is shown in Fig. 7 (Barber and Putterman, 1992). Light from a He-Ne or He-Cd laser irradiates the bubble. A filter which blocks the wavelength of the laser light is placed between the bubble and a photodetector, which is therefore sensitive only to the flash of SL. This serves as the trigger for the zero of time and enables us to average about 500 runs to obtain a final plot. The light scattered by the bubble in a large angle is collected by a lens and passes through a laser line pass filter (which blocks the broadband SL flash) onto a photodetector whose signal $V(t)$ is proportional to $R^2(t)$ plus the background level $\tilde{V}(t)$. The signal and the noise level are shown in Fig. 8. The noise level is measured by shining the laser light through the flask in the absence of a bubble. We presume that the noise is due to stray light and scattering from impurities. The radius is obtained by evaluating $\sqrt{|V(t) - \tilde{V}(t)|}$ which is proportional to the radius, as plotted in Fig. 9 for one cycle of the sound field.

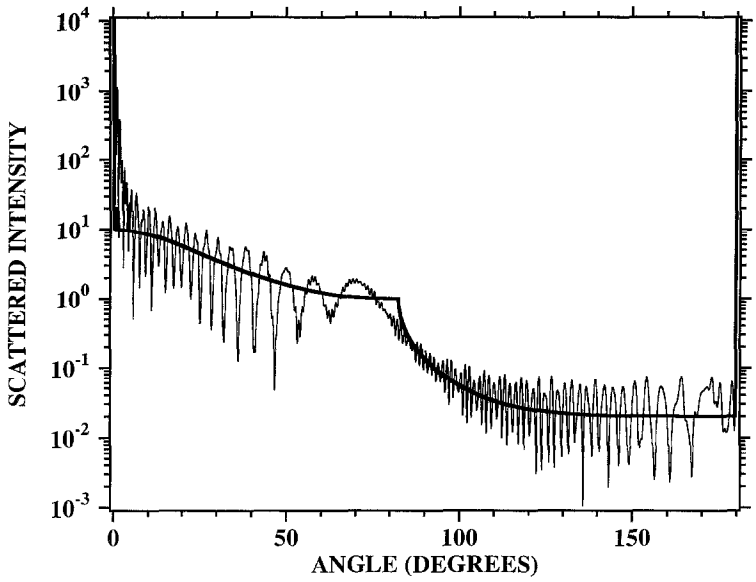

Fig. 6. Intensity of light as a function of angle of scattering. The exact Mie theory (jagged curve) and the WKB or ray optics limit (smooth curve) for a 20 μm air bubble in water illuminated by a He-Ne laser are compared. The intensity is normalized such that geometric reflection from a mirrorlike sphere gives an intensity of 1.

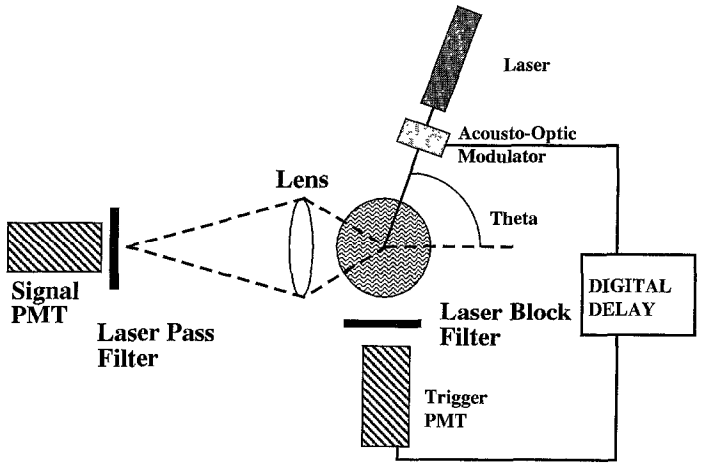

Fig. 7. Apparatus for Mie scattering measurements of a sonoluminescing bubble. By collecting light from a large solid angle the detected intensity becomes proportional to the square of the radius of the bubble. The flash of SL provides a trigger which sets the zero for time and which can be used in conjunction with a pulse delay generator to pick out various portions of the cycle.

Apparent in Fig. 9 are four different timescales of the bubble motion: t_A is the slow expansion of the bubble in response to the rarefaction of the indicated sound field ($\sim$ 15 μs), t_B is the turnaround time at the maximum bubble radius, R_m, which is due to inertia of the bubble ($\sim$ 5 μs), t_C is the runaway collapse of the bubble wall, which leads ultimately to the flash of light (the time for the bubble to collapse from $\frac{1}{2}R_m$ to R_c, the minimum radius is on the order of 1/2 μs), and t_D is

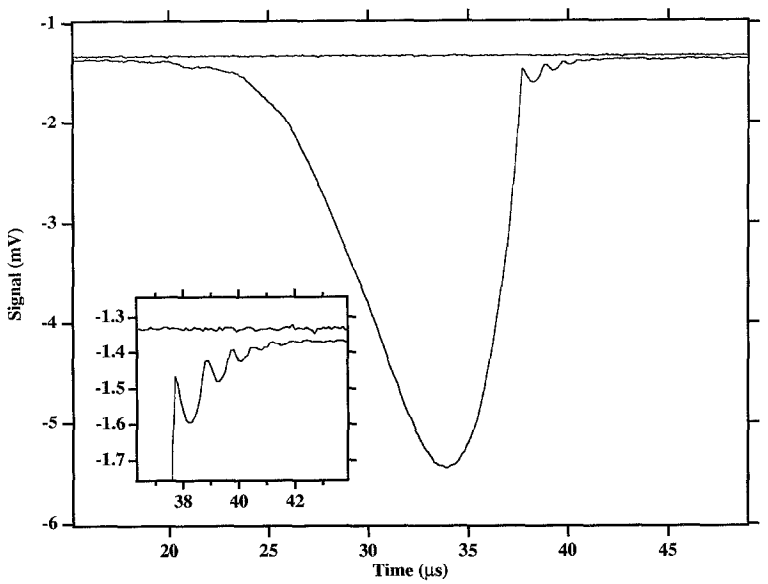

Fig. 8. Signal $V(t)$ and noise level $\tilde{V}(t)$ for light scattered by a sonoluminescing bubble during one cycle of the driving sound field. The inset blows up the difference between signal and noise. These data show more detail than Fig. 1 because it is the average of 512 as compared to 32 sweeps.

the order 1 μs period of the breathing resonance oscillations of the bubble around its ambient size, $R_0(P)$ which is the size of the bubble when it is in static mechanical equilibrium with a gas pressure P on the inside. For $P = P_0$ (which is usually 1 atm) we will simply write $R_0 = R_0(P_0)$. The total pressure P will be due to the externally imposed static pressure P_0 plus the acoustic pressure. It turns out that in the region of the afterbounces P/P_0 is about 2.

A fifth timescale which cannot be obtained from this graph governs the approach to the minimum radius (the time to go from R_0 to R_c). The region of interest can be expanded by using an acousto-optic modulator to select the appropriate portion of the cycle (Barber and Putterman, 1992). By deflecting the laser beam from the bubble during the portion of the cycle when the bubble is near its maximum radius (i.e., when it scatters the most light), one can operate the photomultiplier tube at a higher gain without exceeding its anode current limit. The blowups, Fig. 10, are scaled to the ambient radius, $R_0(P)$, which is the radius approached as the oscillations die out. According to this data the timescale t_E is between 5 and 10 ns. The absolute calibration of such blowups relies on fixing the value of the radius at one instant by a comparison with the larger picture, Fig. 9. The large picture in turn is calibrated by matching it to the theoretical Rayleigh-Plesset equation, discussed in the following section. Suffice it to say here that in view of the wide range of timescales characterizing the SL bubble motion, this fit is highly constrained. For this data one finds $R_m = 38$ μm so that $R_0 \approx 4.0$ μm (Barber and Putterman, 1992).

Alternative measurements of R and $\dot{R}$ at certain points in time can be obtained by fitting data to structure in Mie scattering (Lentz et al., 1995) and by interfering scattered and unscattered light (Delgadino and Bonetto, 1996). By backlighting the bubble Tian et al. (1996) obtained R from video images. Whether these techniques can improve on the calibrations obtained from hydrodynamics

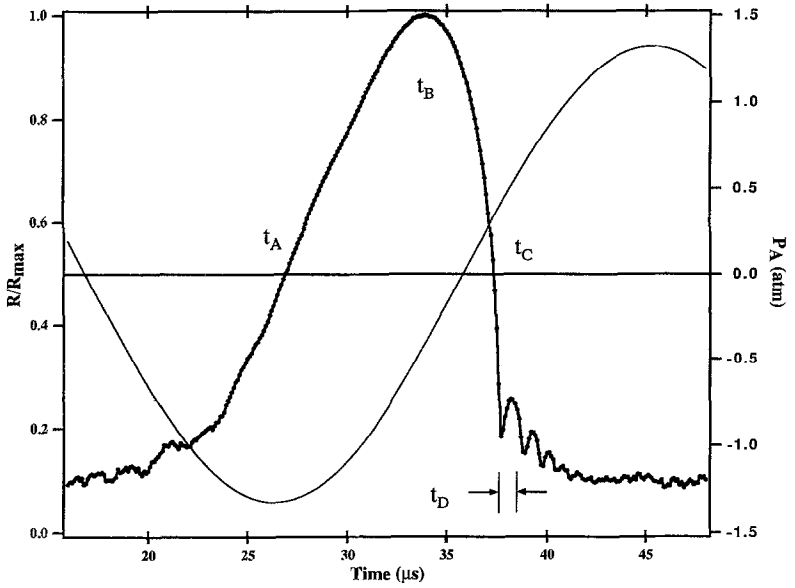

Fig. 9. The radius $R(t)$ scaled to the maximum radius R_m during one cycle of the sound field. If $V(t)$ is the signal on the photodetector and $\tilde{V}(t)$ is the noise level, this plot is given by $\{|[V(t) - \tilde{V}(t)]|/V_m\}^{1/2}$, where V_m is the maximum voltage. Note that for a SL bubble $R_m/R_0 \approx 10$, where R_0 is the ambient radius which is the radius the bubble would have in the absence of a driving pressure. The driving sound field is superimposed. This figure is constructed from the data in Fig. 8, for an air bubble in water. A comparison to the Rayleigh-Plesset equation of bubble dynamics indicates that for these data $R_0 = 4.0$ μm, and the amplitude of the sound field is 1.35 atm.

remains to be seen. Altough all of these methods lack the bandwidth of the Mie scattering technique described in this section, the video images point the way towards the direct detection of deformations in the shape of the bubble.

The measurements shown in Figs. 8–10 are made possible by the nanosecond response time of the photomultiplier tube used to detect the scattered light. However, this response time is still not fast enough to avoid convolving light scattered from different times during the rapid final collapse to the minimum radius, shown in Fig. 10. To determine more accurately this key interval of time leading up to the flash of light, we replaced the CW laser used above with the short flashes of a titanium-sapphire laser (Barber et al., 1997). This laser produces 200 fs wide pulses with a repetition rate of 76 MHz, which corresponds to about 13 ns between flashes. Now the instant at which the light was scattered by the bubble is precisely labelled by the pulse of laser light, and the integrated response of the photomultiplier tube can be attributed to a precise moment in time. Fig. 11 shows the scattered light and the noise level using this apparatus. The width of the peaks is due to the PMT's finite response time (5 ns), which is shorter than the time between consecutive laser pulses (13 ns), so there is no spillover of the tube response from one pulse to the next. The height of the peaks is proportional to the square of the instantaneous radius of the bubble. The SL flash again serves as a temporal reference point in the alignment of many traces.

The traces, such as in Fig. 11, are acquired on a digital oscilloscope with a bin separation of 0.5 ns. The integrated area of each peak is ascribed to the bin corresponding to the time difference between the maximum of the peak and the flash of SL. As data is acquired at different phases relative to the

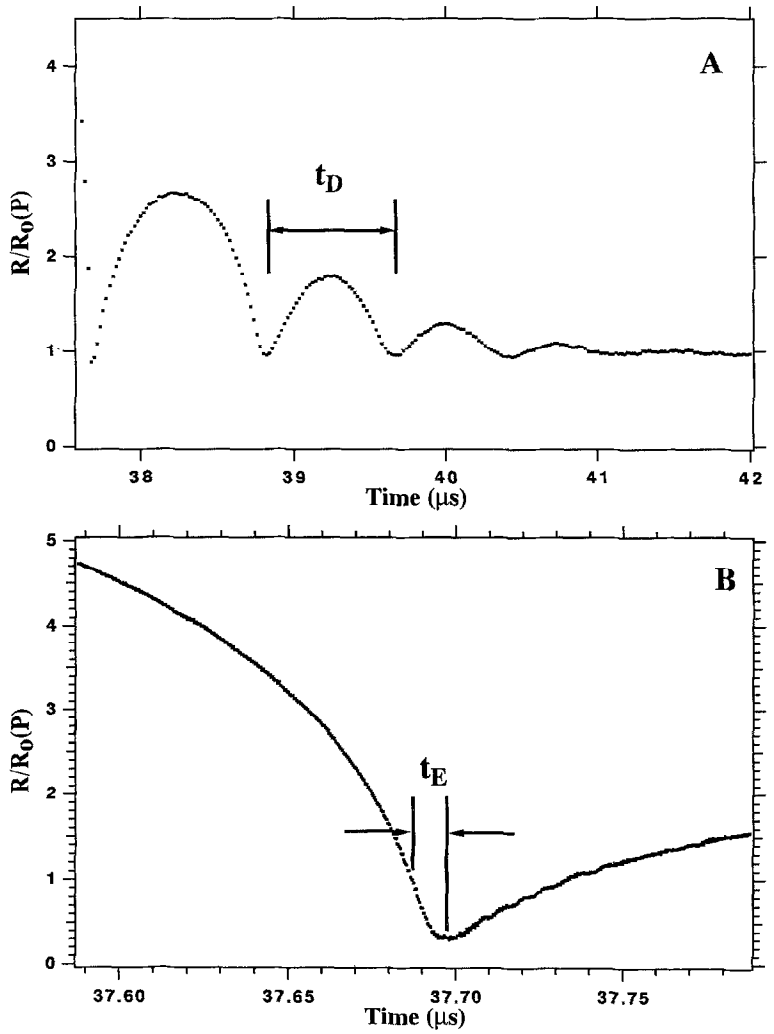

Fig. 10. Detail of the bubble motion $R(t)$ near the minimum radius R_c, taken with continuous laser illumination. These curves, (A) and (B), are taken at the same gain level of the photodetector, which is higher than the gain level used to obtain Fig. 9. The observation that $R_c/R_0(P) \leq 1/8$ indicates that the van der Waals hard core of the gas plays a role in limiting the collapse of the bubble. The breathing period is t_D and the time to go from the ambient radius to the collapse radius is t_E.

SL flash (note that the repetition rate of the laser is not commensurate with the frequency of the sound field), the graph in Fig. 12 is obtained. The calibration of these traces proceeds in the same way as in the CW laser scattering. The complete sound cycle is matched to the theoretical equation, and the blowups are calibrated by using the value of the radius at a point on the large picture.

From Fig. 12 we can conclude that the bubble is collapsing inward at Mach 4, relative to the ambient speed of sound in the gas, and that the acceleration which brings the bubble to a halt at its minimum radius exceeds 10^{11} g (Barber et al., 1997). In addition, as shown in Fig. 13, the SL light

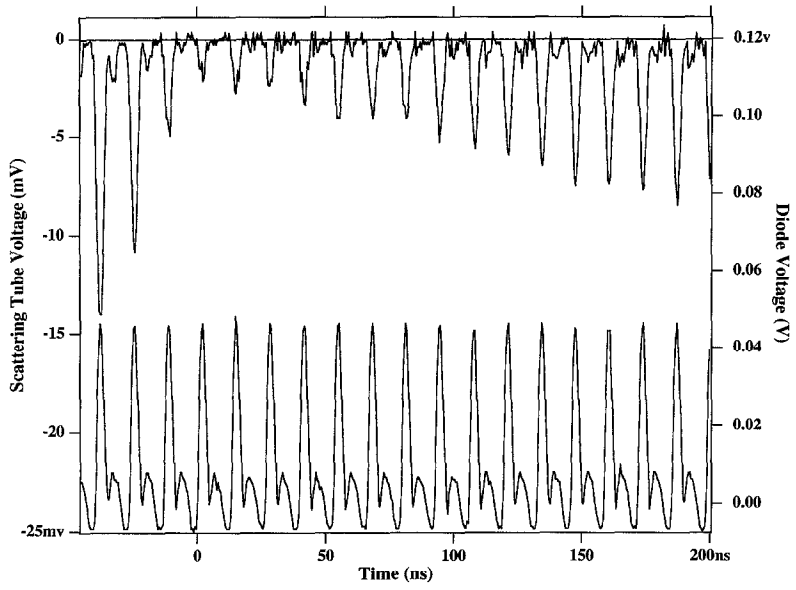

Fig. 11. Pulsed light scattering from a collapsing bubble as probed by 200 fs pulses of light with a repetition rate of 76 MHz (upper trace). The scattering data are generated by a single sweep. The noise floor is obtained from 512 averages. Essential to this method is that the response of the detector return to the noise floor between pulses. In this way each peak can be ascribed to a single, precisely timed scattering event. Shown on the lower trace is the output of the photodiode that tracks the timing of the laser pulses.

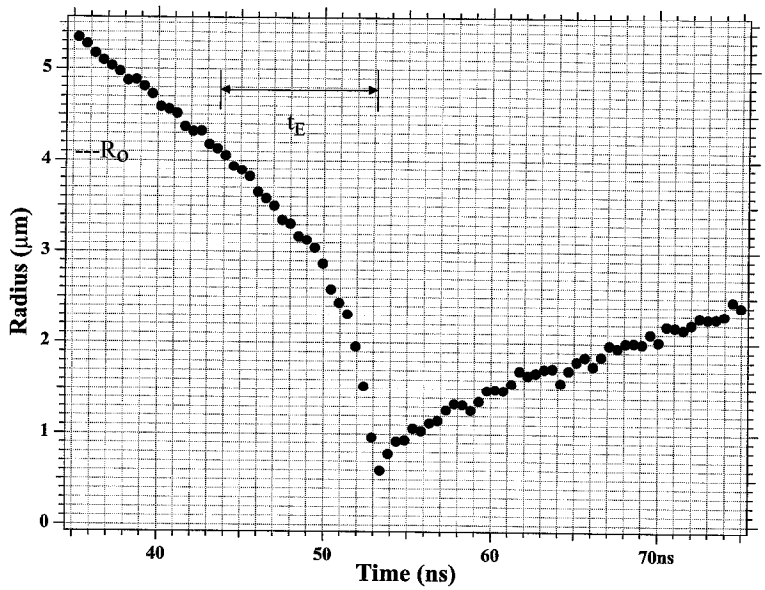

Fig. 12. Radius of a sonoluminescing bubble (1% xenon in oxygen at 150 mm) as the moment of collapse is approached. These points are obtained by averaging together many traces of the type shown in Fig. 11, for various phases of the laser relative to the flashes of SL. According to these data the bubble is collapsing over 4 times the ambient speed of sound in the gas. For this bubble $R_0 \approx 4.1$ μm, $P_a' \approx 1.45$ atm.

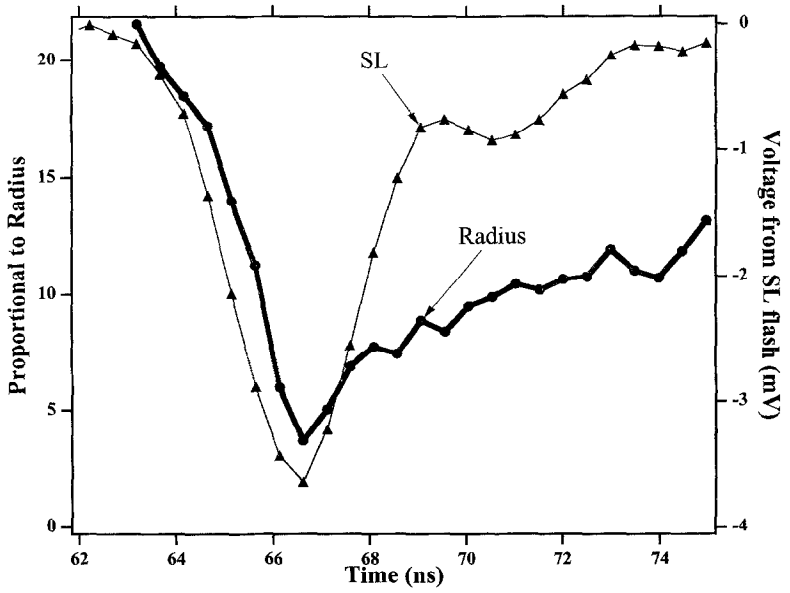

Fig. 13. Flash of SL and light scattering as resolved by the same photomultiplier tube. Each radius measurement is ascribed to that point in time when the response shown in Fig. 11 is a maximum. Thus for comparison the flash of SL must be ascribed to that point in time when the response to the flash is a maximum. As shown by these data the flash occurs within 500 ps of the minimum radius. This improves on the 8 ns resolution of Barber and Putterman (1992) (see their Fig. 4) and the 100 ns resolution of Lentz et al. (1995) (see their Fig. 11).

flash is localized to within 0.5 ns of the minimum. In this experiment the light flash was acquired with the same photodetector that acquired the scattered light and as with the individual scattering peaks of laser light, the time of the flash in Fig. 13 must be ascribed to the location of its maximum. (Using CW scattering led to an incorrect interpretation of the light coming a few ns before the minimum bubble radius R_c (Barber and Putterman, 1992).) The fastest known timescale characterizing SL is the width of the flash (< 50 ps) and this time scale is not resolved or apparent in this light scattering data.

Laser scattering from a non-light-emitting bubble ("bouncing") bubble is more difficult because there is no intrinsic trigger like the SL light flash. The synchronous output of the sine-wave generator, which drives the PZT, serves as a trigger with 10 ns jitter. While this is not nearly enough resolution to characterize the timescales of the SL bubble motion, it suffices to describe the slower bouncing bubble motion (Barber and Putterman, 1992).

4. How does one describe the bubble dynamics?

Except for an interval of time of about 200 ns when the bubble is near its minimum radius, R_c, the speed of the bubble wall, $\dot{R}(t)$, is less than one-tenth of the ambient speed of sound of gas in the bubble and less than one-fortieth of the speed of sound in water. Thus, during 99.5% of the acoustic cycle, one would expect low Mach number hydrodynamics to provide an accurate description of the motion. This expectation is indeed met, and these solutions indicate how the bubble absorbs energy

from the sound field and then begins its runaway collapse. Already in 1917, Rayleigh (1917) made major analytic progress in finding and interpreting the equations which apply in this circumstance. His starting point was fluid mechanics for a barotropic equation of state so that pressure, P, is a function only of the density, ρ. These equations (Landau and Lifshitz, 1987) are

$$\frac{\partial \rho}{\partial t} + \nabla \cdot \rho \boldsymbol{v} = 0 \tag{1}$$

and

$$\frac{\partial \rho v_i}{\partial t} + \frac{\partial}{\partial r_j}[P(\rho)\delta_{ij} + \rho v_i v_j + \tau_{ij}] = 0, \tag{2}$$

where $\boldsymbol{v}(r,t)$ is the velocity, and the viscous stress tensor is given by

$$\tau_{ij} = -\eta\left(\frac{\partial v_i}{\partial r_j} + \frac{\partial v_j}{\partial r_i} - \frac{2}{3}\delta_{ij}\nabla \cdot \boldsymbol{v}\right), \tag{3}$$

where η is the shear viscosity. These equations apply to both the gas in the bubble and the surrounding fluid; the only adjustment is to use the appropriate equation of state for the pressure and value for the shear viscosity. At a spherically symmetric interface the surface tension σ leads to a discontinuity in the perpendicular component of stress:

$$P_g(R,t) - P(R,t) - \frac{4\eta\dot{R}}{R} = \frac{2\sigma}{R} \tag{4}$$

where P_g is the pressure in the gas, P is the pressure in the fluid, and viscous effects lead to $\tau_{rr} = -4\eta\dot{R}/R$, the viscous effects due to the gas being negligible. The center of the bubble is at the origin of the spherical coordinates. To close the equations also requires use of the kinematic boundary condition $v_r(R,t) = \dot{R}(t)$.

In the limit where the imposed sound field $P_a(r,t)$ has a small Mach number, such that $|P_a/\rho c^2| \ll 1$, where c is the speed of sound in the fluid (c_g will denote the speed of sound in the gas), and the Mach numbers and accelerations of the bubble are small,

$$\frac{\dot{R}}{c} \ll 1, \quad \frac{R\ddot{R}}{c^2} \ll 1, \quad \frac{\dot{R}}{c_g} \ll 1, \quad \frac{R\ddot{R}}{c_g^2} \ll 1,$$

and the wavelength of the sound field, $\lambda = 2\pi/k$, is large compared to the bubble radius, $kR \ll 1$, one is led to the leading order Rayleigh-Plesset equation (Rayleigh, 1917; Plesset, 1949; Noltingk and Neppiras, 1950; Prosperetti, 1984; Prosperetti et al., 1988; Löfstedt et al., 1993)

$$R\ddot{R} + \frac{3}{2}\dot{R}^2 = \frac{1}{\rho}(P_g(R) - P_0 - P_a(0,t)) - \frac{4\eta\dot{R}}{\rho R} - \frac{2\sigma}{\rho R} + \frac{R}{\rho c}\frac{\mathrm{d}}{\mathrm{d}t}(P_g - P_a). \tag{5}$$

The left-hand side of this equation represents the inertia of the accelerating bubble in response to the net force on it, which, as on the right hand side, is due to the difference in pressures inside and

outside it. At leading order the damping is due to viscous effects and the radiation of sound into the fluid by the bubble's motion. When next-order terms in a Mach number expansion (Prosperetti, 1984; Löfstedt et al., 1993) are included in the inertial terms, the left-hand side of (5) becomes

$$R\ddot{R}\left(1-\frac{2\dot{R}}{c}\right)+\frac{3}{2}\dot{R}^2\left(1-\frac{4\dot{R}}{3c}\right).$$

For small Mach numbers these corrections are obviously small. But also when the Rayleigh-Plesset equation is used beyond its region of applicability so that $\dot{R}/c \sim O(1)$, these terms present the problem that the effective mass becomes negative. Although these corrections provide a slightly more accurate model for small Mach numbers, we will continue to use Eq. (5) to describe the bubble motion. The externally imposed (sinusoidal standing wave) sound field at the bubble is

$$P_a(0,t) = P_a' \cos(\omega_a t) \tag{6}$$

where P_a' includes the response of the resonator to the drive.

The Rayleigh-Plesset equation needs to be supplemented with an equation of state for the gas, so that it becomes a closed equation for $R(t)$. For rapid changes in the bubble radius we will use the adiabatic equation of state (Löfstedt et al., 1993)

$$P_g(R) = \frac{P_0 R_0^{3\gamma}}{(R^3-a^3)^\gamma}, \quad T_g(R) = \frac{P_0 R_0^{3(\gamma-1)}}{(R^3-a^3)^{\gamma-1}} \tag{7}$$

where $\gamma = C_P/C_V$, the ratio of specific heats, and we have allowed for the possibility that the collapse is sufficiently strong that the hard core radius of the bubble contents, a, is probed. This radius is related to the van der Waals excluded volume, b, by $\frac{4}{3}\pi a^3 = \mathcal{N} b$, where $\mathcal{N}$ is the number of moles in the bubble and for air $b = 0.04\ \ell/\text{mole}$. R_0 is the radius at which the pressure inside the bubble is the ambient pressure, $P_0 = 1$ atm, so that for air $R_0/a = 8.54$. For slow motion we will assume an isothermal equation of state, $P_g(R) = P_0 R_0^3/R^3$; $T_g(R) = T_0$, where T_0 is the ambient temperature. (In general the subscript "g" will denote properties of the gas and the subscript "0" will denote properties of the gas at ambient conditions.)

We typically use the isothermal equation of state for radii larger than the ambient radius, and the adiabatic equation of state for smaller radii. The crossover timescale τ between the two equations of state may be evaluated by calculating the diffusive penetration depth in the gas. If this depth is comparable to the radius of the bubble, the contents will be isothermal; if it is much smaller than 1/3 the radius of the bubble, the adiabatic equation of state is more appropriate. The expression for the diffusive penetration depth (Prosperetti, 1984) is

$$\delta_T = \left(\frac{\kappa_g \tau}{\pi \rho_g C_g}\right)^{1/2}.$$

At ambient density and at an ambient radius of a few microns, the timescale for the crossover is microseconds. The resonant breathing frequency of such bubbles corresponds to this ambiguous regime.

A typical fit of the RP equation to data is shown in Fig. 14 (Barber and Putterman, 1992). The sensitivity of the fit is demonstrated in Fig. 15. Here the fitting parameters, viz. R_0 and P_a, are

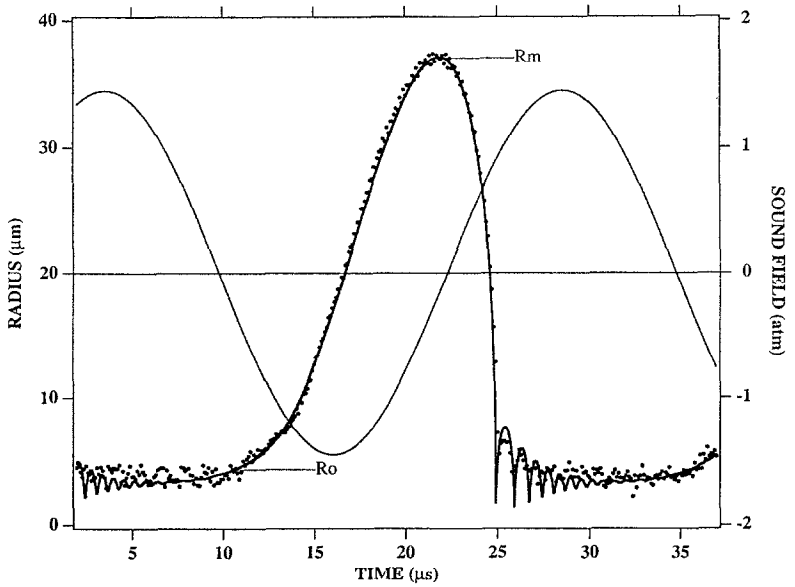

Fig. 14. Radius of a 3 mm xenon bubble as a function of time for one cycle of the sound field. When the acoustic pressure is negative the bubble expands. This is followed by a collapse and ringing before the bubble sits dead in the water waiting for the next cycle. According to a calibration of the data by Rayleigh-Plesset equation (solid line) the ambient radius is 4.3 μm and the driving pressure is 1.45 atm.

varied. Surface tension is typically taken as 50 dyne/cm, and fits generally use an effective damping $\eta \approx 4\eta_{\text{water}} \approx 0.04$ g/cm s due to impurities in the water. In Fig. 14 it is apparent that the fit to the afterbounces is not in very good agreement with the experimental data. The expanded data, Fig. 16, however, shows a good fit to the RP equation. To obtain accurate experimental measurements of these afterbounces, use of the acousto-optic modulator is essential; the PMT cannot resolve the magnitude of the relatively small bounces after being exposed to scattered light from the expansion of the bubble to its maximum size.

The RP equation enables us to calculate the various timescales governing the SL bubble's dynamics (Löfstedt et al., 1993). To characterize the expansion of the bubble from its ambient radius to the maximum radius, we expand the RP equation around the maximum rarefaction of the drive. The expansion is found to be accurately linear in time (Apfel, 1986; Löfstedt et al., 1993), with a slope

$$\dot{R}_A = \left(\frac{2}{3}\frac{P_a' - P_0}{\rho}\right)^{1/2} \tag{8}$$

corresponding to a Mach number relative to the ambient speed of sound in gas $M = 0.01$ for typical $P_a' \approx 1.4$ atm. The time scale t_A is therefore given approximately by

$$t_A \approx (R_m - R_0)/\dot{R}_A \tag{9}$$

and we note that the slope given by (8) is in good agreement with Fig. 14. Due to the inertia of its expansion the bubble continues to grow even after the net pressure acting on it is no longer negative.

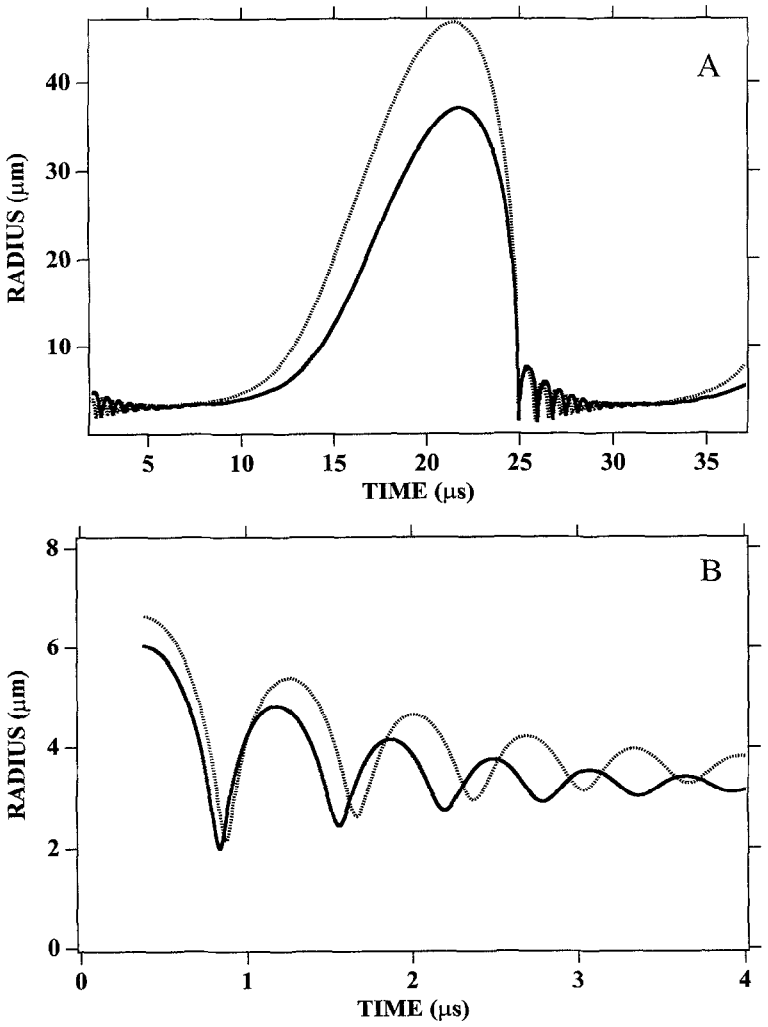

Fig. 15. Sensitivity of solutions to the Rayleigh-Plesset equation. In (a) solutions with the same R_0 but drive pressures differing by 10% are compared. In (b) the amplitude and phasing of the afterbounces are compared for the same drive amplitude but ambient radii differing by 10%. A comparison of light scattering data to the Rayleigh-Plesset equation yields a fit to R_0 accurate to 0.25 μm and to P_a' accurate to 0.05 atm.

This is the timescale t_B associated with its turnaround at the maximum radius. Expanding the RP equation around this radius yields

$$t_B \approx \left(\frac{\rho R_m^2}{P_0}\right)^{1/2} \tag{10}$$

which is on the order of 5 μs (again in good agreement with Fig. 14). If this timescale is comparable to the time t_- required for the sound field to go from $-P_0$ to zero, then the bubble will find itself perched at its maximum radius with a vacuum on the inside and P_0 on the outside. So if

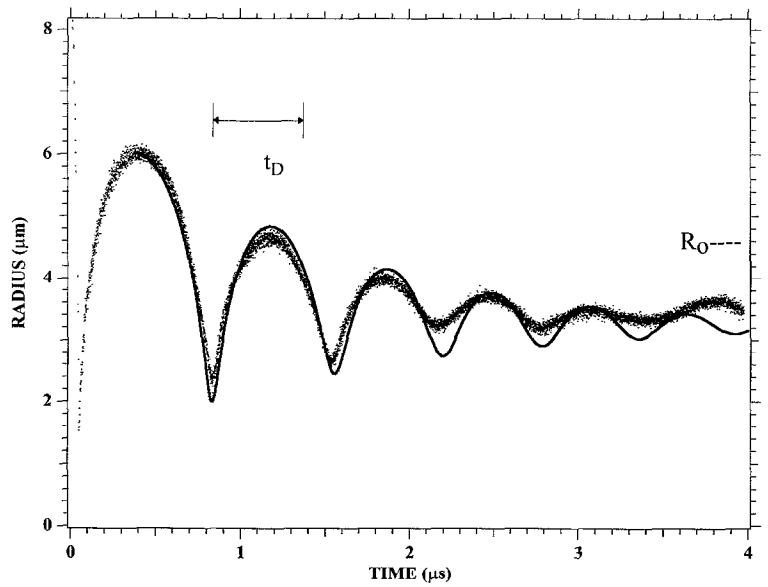

Fig. 16. Comparison of data and fit to the Rayleigh-Plesset equation for the afterbounces of a 3 mm xenon bubble. To account for impurities in the water we interpret the viscosity as an effective damping and take its value as 0.04 g cm/s (four times the tabulated viscosity of pure water), and for surface tension the value 50 dyne/cm is taken.

$$t_B \sim t_- = (1/\omega_a)\sin^{-1}(P_0/P_a') \tag{11}$$

the bubble at $R = R_m$ will be unstable against the collapse, which was first calculated by Rayleigh (1917). The time required for the bubble to collapse from its maximum radius to its minimum radius can be evaluated by first transforming (5) to obtain (Löfstedt et al., 1993)

$$\frac{\mathrm{d}}{\mathrm{dt}}\left(\frac{1}{2}R^3\dot{R}^2 + \frac{P_0R^3}{3\rho} - \frac{1}{\rho}\int P_g(R)R^2\,\mathrm{d}R\right) = 0 \tag{12}$$

which applies when damping and surface tension are negligible. Integrating this equation from R_m, where $\dot{R} = 0$, to R, and noting that unless R is within a percent of the hard core a the back pressure of the gas is negligible, yields

$$\frac{1}{2}R^3\dot{R}^2 + \frac{P_0(R^3 - R_m^3)}{3\rho} = 0. \tag{13}$$

For values of $R < R_m/2$ we have to about 10% accuracy

$$\dot{R} = -(2P_0/3\rho)^{1/2}R_m^{3/2}/R^{3/2} \tag{14}$$

so that the time to go from $R_m/2$ to R_0 is

$$t_C \approx \frac{R_m}{10\sqrt{P_0/\rho}} \tag{15}$$

and the time to go from R_0 to the minimum radius is

$$t_E \approx \frac{\sqrt{6}\,R_0^{5/2}}{5R_m^{3/2}(P_0/\rho)^{1/2}}. \tag{16}$$

For typical parameters $t_C \approx 500$ ns and $t_E \approx 8$ ns, also in good agreement with experiment (Barber and Putterman, 1992; Löfstedt et al., 1993). This calculation involves only the approximations that the Mach number relative to the speed of sound in the fluid is small, $\dot{R}/c \ll 1$, so that the radius of the bubble must be larger than about $3a$. For such radii one can also easily verify that the damping effects are small and that P_g can be neglected. Even when $\dot{R}/c \ll 1$ it is possible that $\dot{R}/c_g \sim 1$. In this limit (12) still applies but the equations of state (7) become a very poor description of the gas inside the bubble (Greenspan and Nadim, 1993; Löfstedt et al., 1993); in particular the gas becomes nonuniform so that $P_g(r,t) \neq P(R(t))$.

A linearization of (5) around the ambient radius R_0 yields the dispersion law for the (adiabatic) radial pulsations of a free bubble with a frequency (Prosperetti, 1984)

$$\omega_0(P) = [3\gamma P/\rho R_0^2(P)]^{1/2} \tag{17}$$

so that $t_D \approx 2\pi/\omega_0(P)$. Approximating P with P_0 and $R_0(P)$ with R_0 yields $t_D \sim 1.3$ μs for $R = 4.5$ μm. The difference between this estimate and the actual period (~ 0.75 μs) can be accounted for by the factor:

$$\omega_0(P)/\omega_0 = [R_0/R_0(P)]^{5/2} = (P/P_0)^{5/6}$$

where P is the total pressure acting on the ringing bubble and $R_0(P)$ is the asymptote in Fig. 16.

Finally, one can also use the RP equation to estimate the time for the bubble to turn around at its minimum radius by expanding (5) around R_c. Using the parameters appropriate to SL, one finds a timescale of about a hundred picoseconds (Löfstedt et al., 1993). However, this short timescale clearly lies outside of the validity of the hydrodynamic approximations which led to the derivation of the RP equation. Such calculations serve only to show that these approximations are violated, and that while the RP is rich in mathematical implications at these parameters, it misses the physics essential to SL.

As the bubble collapses the increasing pressure in the interior becomes a pressure source for an outgoing acoustic wave. To lowest order in the Mach number relative to the fluid, the scattered field takes the form (Löfstedt et al., 1993),

$$P_{\text{scatt}}(r,t) = \rho\left(\frac{2R\dot{R}^2 + R^2\ddot{R}}{r}\right)_{t-(r-R)/c}. \tag{18}$$

Using the RP equation for $R(t)$, one can readily reproduce the acoustic spike, depicted in Fig. 1, trace "a" (Barber et al., 1997). In particular the spike is a compression, it is delayed by the time that it takes the pulse to travel the 1 mm from the bubble to the microphone, and the spike width is due to the response of the microphone to the nanosecond bubble dynamics. A blow-up of the spike is shown in Fig. 17. Based upon the calibration of the manufacturer (Precision Acoustics), the peak has an amplitude of 3 atm at 1 mm from the bubble. The initial amplitude of the outgoing acoustic spike may be obtained by correcting for the spreading and damping of the high frequency waves as they travel from the bubble wall (at 0.5 μm) to the microphone.

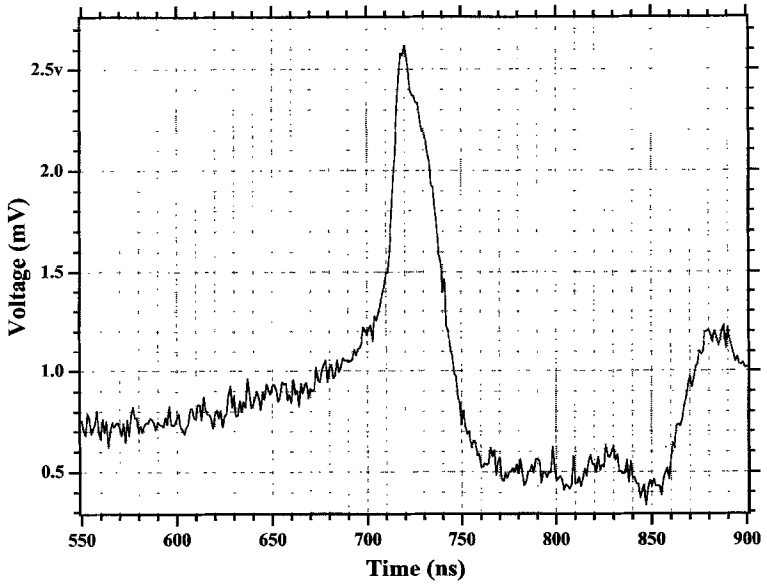

Fig. 17. Response of a PVDF needle hydrophone to the short pulse of sound emitted by the collapsing bubble. This is the spike shown on trace (b) of Fig. 1 with an expanded timescale. The rise time of 10 ns is instrument limited and indicates the presence of frequencies greater than 30 MHz. (Hallaj et al. (1996) report the measurement of a 5 ns risetime that is still instrument limited.) According to the calibration of the hydrophone, the signal at 1 mm from the bubble is about 3 atm. Correcting for geometric dispersion the amplitude at the point of emission (0.5 μm) is over 6000 atm. The attenuation of sound is also considerable for high frequency pulses. For instance a 300 MHz pulse is reduced in amplitude by a factor of 10000 after having travelled 1 mm. Inclusion of this effect would substantially increase the estimate of the launching amplitude of the outgoing pulse.

Interpreting Eq. (12) as an energy equation (Noltingk and Neppiras, 1950; Löfstedt et al., 1993), one can show that the quantity of energy absorbed by the bubble from the sound field during its expansion is $\frac{4}{3}\pi R_m^3 P_0$. About half of this energy is radiated as sound during the bubble's collapse, and the rest is dissipated by the viscosity. In fact, by equating the energy absorbed to the energy radiated at the minimum, one can obtain an analytic estimate of the bubble's minimum radius, with reasonable accuracy. The energy of the radiated light from the brightest bubble represents only 0.01% of the acoustic drive input. However, the energy radiated as light is comparable to the acoustic energy dissipated in the resonator, *in the absence of a bubble*, by the shear viscosity. To see this consider the ratio of the energy stored in the bubble to the energy stored in the sound field in the flask (Löfstedt et al., 1993)

$$\frac{E_b}{E_a} = \frac{P_0 R_m^3}{\rho M^2 c^2 R_f^3}. \tag{19}$$

The ratio of the rate at which these quantities dissipate is then

$$\frac{\dot{E}_b}{\dot{E}_a} = \frac{P_0 R_m^3}{2\pi M^2 \omega \eta R_f^3} \tag{20}$$

which is order 10^4! The huge rate at which bubbles scatter sound energy is the reason why bubbles make outstanding contrast agents for acoustic radiology (Feinstein, 1989; de Jong et al., 1992; D'Arrigo et al., 1993).

A key feature of the SL bubble dynamics is the asymmetry of the expansion and collapse (Löfstedt et al., 1993). The origin of this asymmetry is the inertia of the bubble which allows it to expand even after the net pressure acting on it is no longer negative. This overshoot of the bubble expansion (as described by Eq. (10)) implies that when the bubble reaches its maximum size, the external sound field has already turned compressive, and thus there is no force to resist the bubble wall's runaway collapse into its evacuated interior. This asymmetry sets the arrow of time for the SL process by leading to such a fast collapse that the radiation damping then causes the bubble to sit dead in the water waiting for the next cycle.

An empirical criterion for SL derives from the observation that the collapse toward the minimum radius for a sonoluminescing bubble attains Mach 1, relative to the ambient speed of sound in air, at its ambient radius (Barber et al., 1994). From Rayleigh's equation (1917) for the collapse (14), this condition can be written as

$$\frac{\dot{R}(R_0)}{c_g} \approx \left[\frac{2}{3\gamma}\frac{\rho_0}{\rho}\left(\frac{R_m}{R_0}\right)^3\right]^{1/2} \approx \mathrm{O}(1). \tag{21}$$

Solving this equation for the expansion ratio of maximum radius to ambient radius gives $R_m/R_0 \approx 10$ as the condition for SL. This condition is lent additional support by "waterfall" plots of the bubble dynamics as a function of drive pressure (Fig. 18) (Barber et al., 1994). At low drive levels, a stably-trapped, but non-light-emitting, "bouncing" bubble obeys the RP equation, and its motion throughout the acoustic cycle is well-described by low Mach number hydrodynamics. The expansion ratio is about 3, and thus the criterion for SL is not met. At a certain drive level, the lower threshold, the bubble suddenly shrinks, the expansion ratio increases, and the bubble begins to emit light. As shown in Fig. 19, which is a detail of Fig. 18, the lower threshold for SL is related to the sudden change in the ambient size in the bubble, a parameter which is undetermined by the RP equation.

Interaction with the standing wave sound field also determines the time averaged force of trapping of the bubble (King, 1934; Löfstedt and Putterman, 1991; Löfstedt et al., 1995)

$$\boldsymbol{F}_a = -\langle V \boldsymbol{\nabla} P_a \rangle \tag{22}$$

where V is the volume of the bubble. For small oscillations the acoustic radiation (or Bjerknes) forces are second-order effects in the drive amplitude (Bjerknes, 1906). For an SL bubble, the time averaged force is dominated by the expansion of the bubble, which is when the volume is largest and the drive pressure passes through an ascending node (Löfstedt et al., 1995). In this way (22) becomes, to a good approximation

$$F_a = \tfrac{1}{24}\pi R_m^3 P_a' k_z^2 z \tag{23}$$

where k_z is the z component of the sound field and z is the distance of the bubble from the pressure antinode. The force is directed toward the pressure antinode. It is remarkable that the great nonlinearity of the bubble motion leads to a radiation force that is linear in the external drive. This force must balance the force of buoyancy due to gravity which acts in the z direction

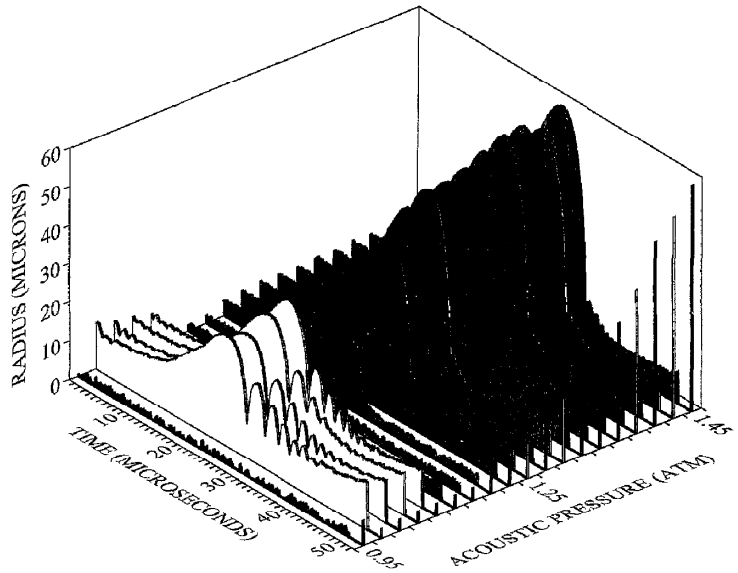

Fig. 18. Bubble radius verus time for about one cycle of the imposed sound field as a function of increasing drive level. The shaded area represents the light emitting region. The relative intensity of the emitted light as a function of drive level is indicated by the vertical lines. For the unshaded region, the air bubble is trapped, but no light is emitted. At drive levels below the unshaded region the bubble dissolves over a long time scale ($\sim$ 1 s). The lowest amplitude sweep (no bubble present) indicates the noise level.

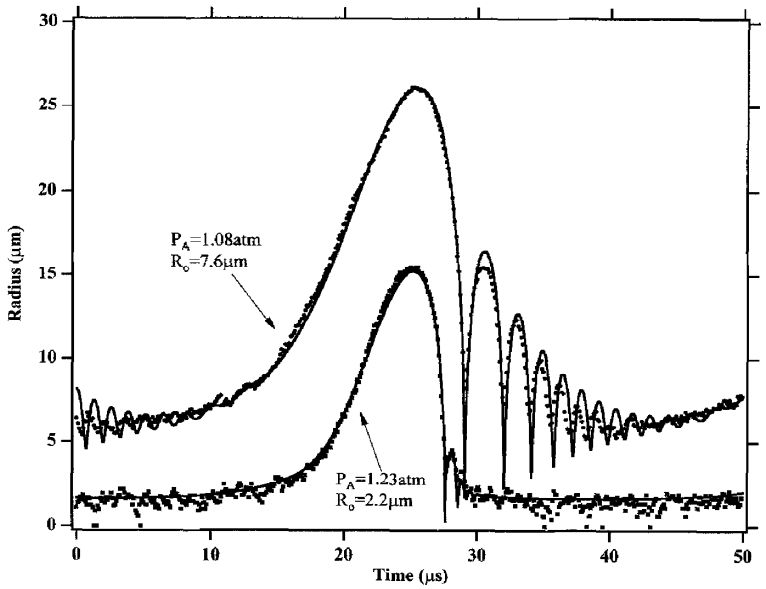

Fig. 19. Plot of radius versus time for bubble motion just above and below the threshold for the onset of sonoluminescence. Note that the expansion ratio R_m/R_0 increases from 3.5 to 9 as the system goes from a non-light-emitting bubble to an SL bubble.

$$F_b = \rho g \langle V \rangle \approx \tfrac{1}{3}\pi R_m^3 \rho g. \tag{24}$$

The distance of the bubble from the velocity node then is

$$\langle z \rangle \approx 8\rho g / P_a' k_z^2 \tag{25}$$

which is typically less than 1 mm. The motion around this average is reduced by an additional factor of $P_a'/2\pi\rho c^2$. If the sound field is turned off, the bubble radius drops to R_0 and the bubble floats up with the terminal velocity

$$v_F = \frac{2R_0^2 g}{9\eta/\rho} \tag{26}$$

which for typical values is 5×10^{-3} cm/s.

In general the role of surface tension in SL bubble dynamics is small and for this reason it was neglected in the above discussions. However for sufficiently small bubbles, surface tension becomes a sizable correction to the ambient properties of the bubble (Löfstedt et al., 1995). For instance the frequency of ringing of a bubble becomes

$$\omega_0 = (3\gamma P_0 / \rho R_{0\sigma}^2)^{1/2} \tag{27}$$

where the radius $R_{0\sigma}$ of the bubble when it is in mechanical equilibrium with the externally imposed pressure P_0 is determined by

$$P_g(R_{0\sigma}) = P_0 + \frac{2\sigma}{R_{0\sigma}} \tag{28}$$

so that to a very good approximation

$$\Delta R_\sigma = R_0 - R_{0\sigma} = 2\sigma/3P_0 \approx 0.35\ \mu\text{m}. \tag{29}$$

In particular the expansion of the bubble, which commences when the net pressure acting on it is negative, can be delayed because the negative pressure of the acoustic drive must overcome both the ambient pressure and the extra pressure due to surface tension. The criterion for expansion becomes

$$|P_a(t)| > P_0 + \frac{2\sigma}{R(P_a \approx -P_0)} \tag{30}$$

where $R(P_a = -P_0)$ is the radius of the bubble when the net external pressure goes through zero (i.e. when $P_a \approx -P_0$). At negative net pressure stationary mechanical equilibrium is impossible and the bubble wall acquires a velocity. Substituting for R in (30) yields the magnitude of the rarefaction that must be exceeded so that the bubble rapidly expands

$$|P_a| > P_0 + \frac{2\sigma}{R_0}\left(\frac{2\sigma}{R_0 P_0}\right)^{1/2}. \tag{31}$$

For 2 μm bubbles this threshold is increased by 35%. The maximum velocity of bubble expansion (see Eq. (8)) is similarly reduced to:

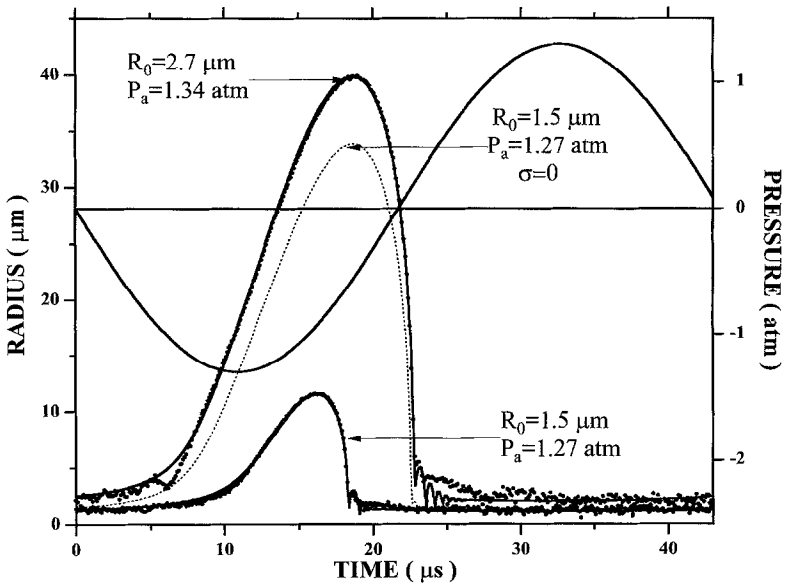

Fig. 20. Radius versus time for 1% xenon in nitrogen bubbles at 150 mm partial pressure of solution. Shown is the transition to SL from a small bubble whose dynamics are dominated by surface tension. The dashed line is a solution to the Rayleigh-Plesset equation with surface tension set equal to zero. It differs dramatically from the actual motion of the small ($R_0 = 1.5$ μm) bubble, which does, however, match the same equation when surface tension is included.

$$\dot{R} \approx \sqrt{\frac{2}{3}\frac{P_a' - P_0 - (2\sigma/R_0)(2\sigma/R_0P_0)^{1/2}}{\rho}}. \tag{32}$$

This effect is displayed in Fig. 20 which shows the light scattering measurements of a bubble formed from a 1% xenon-doped nitrogen mixture in water at a partial pressure of 150 mm (Löfstedt et al., 1995). According to this data the surface tension for this small bubble ($R_0 = 1.5$ μm) reduces R_m from 35 μm to 10 μm. It should be clear that surface tension can suppress the onset of light emission in these bubbles because the critical expansion ratio is not reached. In addition surface tension is associated with hysteresis in the ramping up and down of the acoustic drive pressure (Löfstedt et al., 1995). For example the transition to SL for a 0.1% xenon in nitrogen bubble at 150 Torr is shown in Fig. 21. Note that SL is separated from the non-light-emitting regime by a region where there is no steady-state bubble motion. Within the non-SL region an upward sweep in drive amplitude marches from bubble to bubble regardless of the rate of increase of the acoustic pressure. However, an infinitesimal step to lower P_a' will cause the bubble to disappear. Nor can such a bubble be reseeded at the drive level at which it disappeared; to recover the stable small bubble, one must start with a lower-amplitude bubble and increase the drive level.

The Rayleigh-Plesset equation of bubble dynamics shows how the bubble takes energy from the sound field and then accelerates to a velocity comparable to the speed of sound. At that point more complete equations of state (or microscopic theories) and nonlinear dynamics must be employed. Furthermore, the ambient radius R_0 and the allowed range of acoustic drives P_a are not determined a priori by this equation.

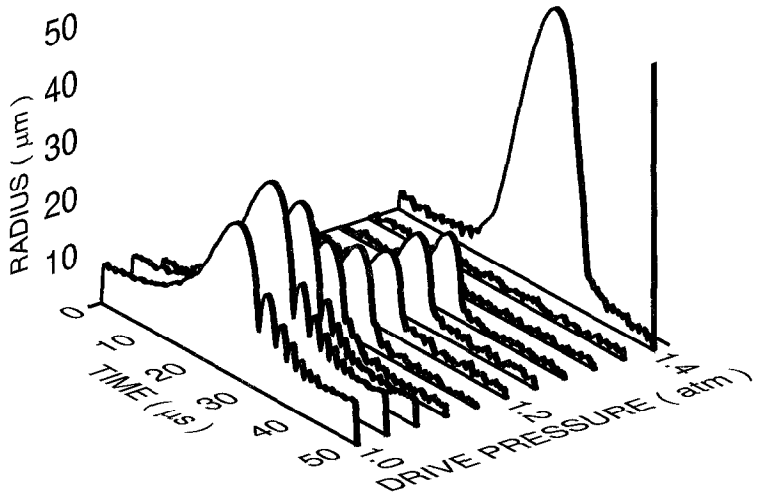

Fig. 21. Transition to SL for a 0.1% xenon in nitrogen bubble at 150 mm. These radius versus time curves were taken as a function of increasing drive level. With this system bubbles cannot be seeded between 1.1 and 1.35 atm. Those states must be approached from the lower amplitude, bouncing bubble regime.

5. Why is a small percentage of noble gas essential to stable, visible sonoluminescence?

To learn about SL we initially tried to expand the available parameter space by obtaining light from air bubbles in non-aqueous fluids such as alcohols and low-viscosity silicone oils (Weninger et al., 1995). The difficulties faced in this endeavor led us instead to search for light emission from water with gases other than air dissolved in it (Hiller et al., 1994; Hiller and Putterman, 1995). This led to the design of the sealed acoustic resonator and gas manifold system described in Figs. 4 and 5 (Hiller et al., 1994; Hiller, 1995).

The first experiments in this line of research used pure nitrogen gas, since it comprises 80% of air. To our surprise neither pure N_2 nor pure O_2 nor an 80 : 20 mixture of the two yielded a stable or visible signal. After convincing ourselves that there were no problems with the vacuum transfer system, we realized that air is 1% argon, and indeed, as shown in Fig. 22, a small amount of noble gas is essential for the activation of stable bright (i.e. visible to the eye) SL (Hiller et al., 1994). The effect of doping nitrogen with argon as a function of partial pressure is shown in Fig. 23.

It should be emphasized that when we speak of a gas mixture of a certain composition, we are referring to the mixture dissolved in the water. As of yet, we have not been able to determine the contents of the bubble. For instance, we cannot experimentally rule out the possibility that a 1% argon in nitrogen solution in water at 150 mm yields a bubble that is filled with pure argon. Of course such a scenario would violate the theoretical predictions of diffusion, the applicability of which will be discussed in the next section.

In Fig. 23 we see that at high and low partial pressures the SL intensity from a 1% argon in nitrogen mixture decreases (Hiller et al., 1994). As the saturation concentration of this mixture is approached, the light emission disappears; by contrast, pure argon bubbles yield SL at all partial pressures, although such bubbles are the most stable near 3 mm.

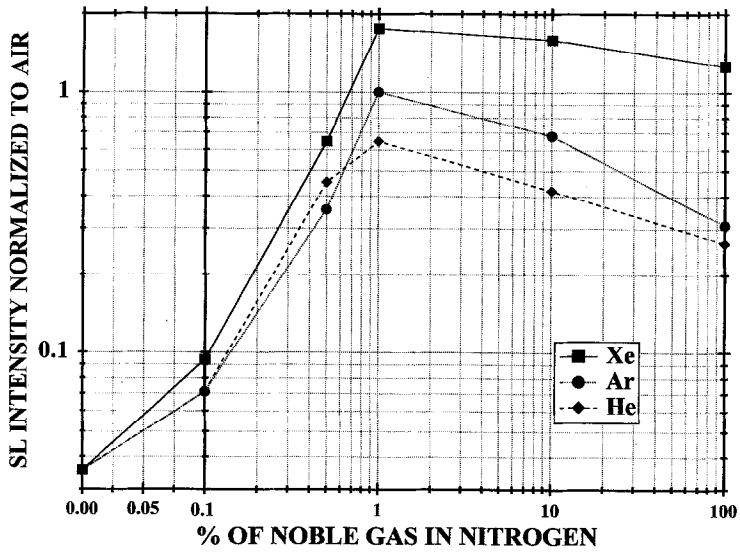

Fig. 22. Intensity of light emission from a sonoluminescing bubble in water as a function of the percentage (mole fraction) of noble gas mixed with nitrogen. The gas mixture was dissolved into water at a pressure head of 150 mm. The data are normalized to the light emission of an air bubble in 24°C purified water with a resistance greater than 5 MΩ cm dissolved at 150 mm. Such an air bubble emits about 2×10^5 photons per flash.

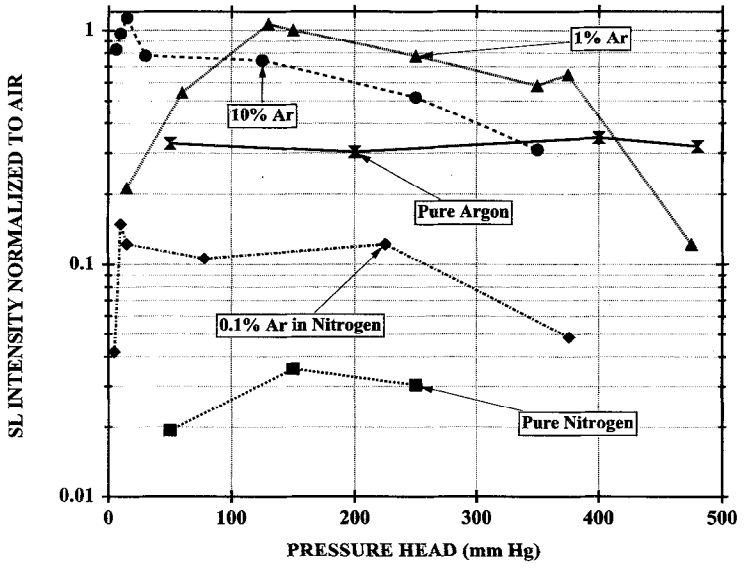

Fig. 23. Intensity of SL from an argon-doped nitrogen bubble as a function of the degree of saturation of the gas in the water. To observe SL from an air bubble requires some degree of degassing but a pure argon bubble can glow at concentrations approaching saturation. Since tap water is saturated with air it will not yield SL, but if tap water is pressurized to about 5 atm the concentration of air falls to 20% (which is comparable to a 150 mm solution at 1 atm) and SL can then be observed.

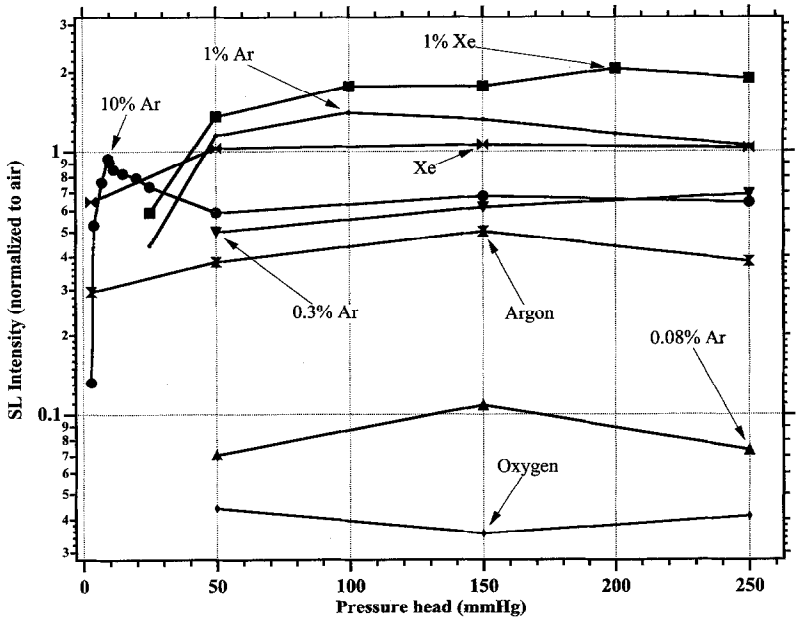

Fig. 24. Sonoluminescence from noble-gas doped-oxygen bubbles. The enhancement effect in oxygen is very similar to that which occurs in nitrogen.

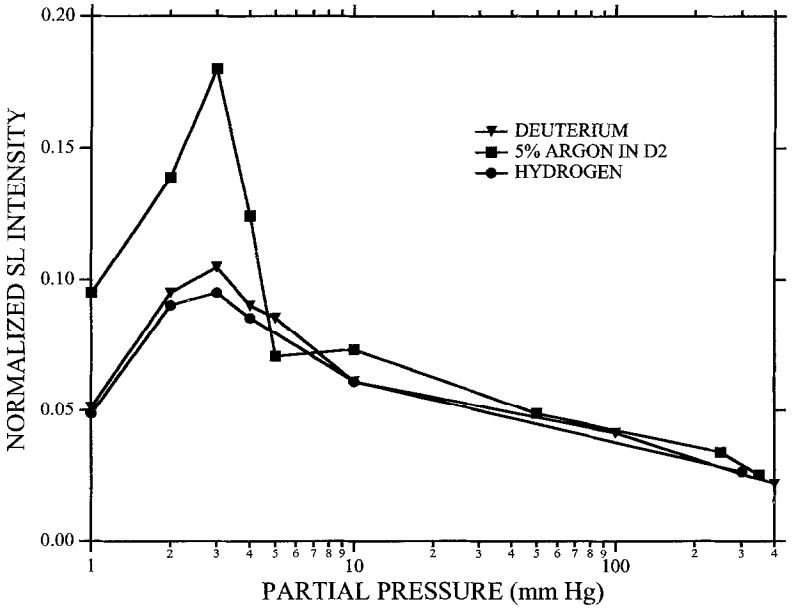

Fig. 25. Sonoluminescence from hydrogenic bubbles and argon-doped deuterium. Hydrogenic bubbles are very unstable, and they do not exhibit the enhancement effect displayed by oxygen and nitrogen.

As shown in Fig. 24 we have found that the noble gas doping effect also works for oxygen (Chow et al., 1996). This indicates that we are here dealing with the physics of atoms and plasmas as opposed to, say, effects of chemical reactions (Griffing, 1952; Suslick and Flint, 1987; Verrall and Sehgal, 1987; Lohse et al., 1996), or the properties of gas scintillators (Birks, 1964; Tornow, 1996). With regard to gas discharge physics an analogy can perhaps be found in the Penning effect (Penning and Addink, 1934) where various gas mixtures can dramatically alter discharge characteristics. However, with SL the gas compressions approach solid densities, and the system is far from the parameter space where the Penning effect is usually studied.

The enhancement effect observed with N_2 and O_2 is not observed with H_2 or D_2 as shown in Fig. 25 (Barber et al., 1995). These bubbles are very dim and unstable. It may turn out that as higher degrees of water and gas purity are achieved, and in particular any air leaks from the gas manifold system are removed, the bubbles of hydrogen and deuterium will be even dimmer than shown in Fig. 25. An outstanding question remains how to enhance SL from hydrogenic gases. There is of course a large parameter space to probe, including the ambient temperature, the ambient pressure, the partial pressure, and the possibility of adding surfactants to the water. As of yet, the brightest and most stable room-temperature bubble appears to be a 1% mixture of xenon in oxygen at a partial pressure of 150 Torr.

6. What determines the ambient radius?

For given experimentally controllable parameters, such as the drive pressure, the ambient temperature, the gas and fluid composition, Nature determines the ambient radius (Löfstedt et al., 1995). It is not in the experimentalist's power to scale up the size of the SL bubble. In fact, it is not yet theoretically possible to predict the size of the SL bubble, or the range of drive pressures for which SL exists. Since the transition to SL is accompanied by a change in the ambient radius, it is clearly an important object of study.

Simple diffusion theory does predict a stable, stationary value for the ambient radius (Eller and Flynn, 1965; Fyrillas and Szeri, 1994; Löfstedt et al., 1995). This value is determined by requiring a balance between the gas flow into and out of the bubble during its oscillatory cycle. A gas-fluid interface achieves thermodynamic equilibrium when a certain partial pressure of gas is dissolved in the fluid; this partial pressure, at least in the dilute gas limit, is proportional to the pressure of the gas above the fluid. Consider now the oscillation of the SL bubble. When the bubble expands, the pressure of the gas inside it goes down, and gas will flow out of the surrounding fluid into the bubble. When the bubble size is smaller than a certain radius, the gas pressure is higher than would be in equilibrium with the surrounding fluid, and gas will flow out of the bubble interior into the surrounding fluid. A steady-state size of the bubble is achieved if these flows of mass are balanced. Thus, diffusion theory predicts a distinct ambient radius for a fixed acoustic drive amplitude and fixed concentration of gas dissolved in the fluid.

Mathematically, this picture is expressed by the diffusion of equation of gas in the fluid (Landau and Lifshitz, 1987),

$$\frac{\partial C}{\partial t} + \frac{\dot{R}R^2}{r^2}\frac{\partial C}{\partial r} = D\nabla^2 C \tag{33}$$

where $C(r,t)$ is the concentration of gas in the fluid, D is the diffusion constant for gas in the fluid ($\sim 2\times 10^{-5}$ cm^2/s for air in water), and the convective term takes into account the pulsations of the bubble. This equation is subject to the boundary condition at the bubble wall

$$C(r=R) = C_0 P_g(R)/P_0 \tag{34}$$

where $C(r,t)$ is the saturated concentration of gas dissolved in the fluid at 1 atm (for air in water $C_0/\rho_0 \approx 0.02$ where $\rho_0 \approx 1.3\times 10^{-3}$ g/cm^3 (Battino et al., 1984)). This boundary condition expresses Henry's law for the fluid-gas interface (Fermi, 1936). The concentration of gas in the fluid at infinity, $C(r=\infty) = C_\infty$, is determined by the preparation of the fluid, $C_\infty/C_0 = P_\infty/P_0$ where P_∞ is the partial pressure of the gas in solution as is established by the methods discussed in Section 2.

A solution of (33) for steady-state motion determines the ambient radius which would be in equilibrium with a given partial pressure of gas dissolved in the fluid (Fyrillas and Szeri, 1994; Löfstedt et al., 1995)

$$C_\infty = \frac{1}{T_a}\int_0^{T_a} \frac{C_0 P_g(R)}{P_0}\mathrm{d}\tau' \tag{35}$$

where T_a is the acoustic period and

$$\tau(t) \equiv \int^t R^4(t')\,\mathrm{d}t'. \tag{36}$$

This result applies in the limit where the diffusive penetration depth is small compared to the maximum radius or $\delta_D = \sqrt{2D/\omega_a} \ll R_m$.

Since the integral in (35) is dominated by the maximum size of the bubble, C_∞ is determined by that part of the motion when the bubble is isothermal (Löfstedt et al., 1993). Using the isothermal equation of state one finds that the bubble which is in diffusive equilibrium with the surrounding fluid obeys (Löfstedt et al., 1995)

$$\frac{C_\infty}{C_0} \approx 3\left(\frac{R_0}{R_m}\right)^3. \tag{37}$$

A comparison of this formula (or more precisely Eqs. (35), (36)) with the ambient size of low drive "bouncing" bubbles shows that diffusion determines the size of these bubbles as in Fig. 26.

However, if we return to the waterfall plot of the transition to SL, it is clear that both the bouncing bubble and the SL bubble cannot be in diffusive equilibrium at the same partial pressure. Yet this is precisely what is found for air bubbles in water. In Fig. 27 is plotted the phase of the SL light emission relative to the driving sound field (Barber et al., 1995). The 150 Torr air bubble in water shows no jitter on such a plot, indicating that it is stably maintained at that partial pressure. For this bubble the transition to SL is accompanied by the appearance of an as yet undetermined mass flow process that enables the system to violate Eq. (37) by a factor of about 50.

Given the expansion ratio of about 10 : 1 which is characteristic of SL, one finds from Eq. (37) that SL bubbles should be in diffusive equilibrium at around 3 Torr. This turns out to be the partial pressure where pure noble gas bubbles are stable, as is also indicated in Fig. 27 (Barber et al., 1995).

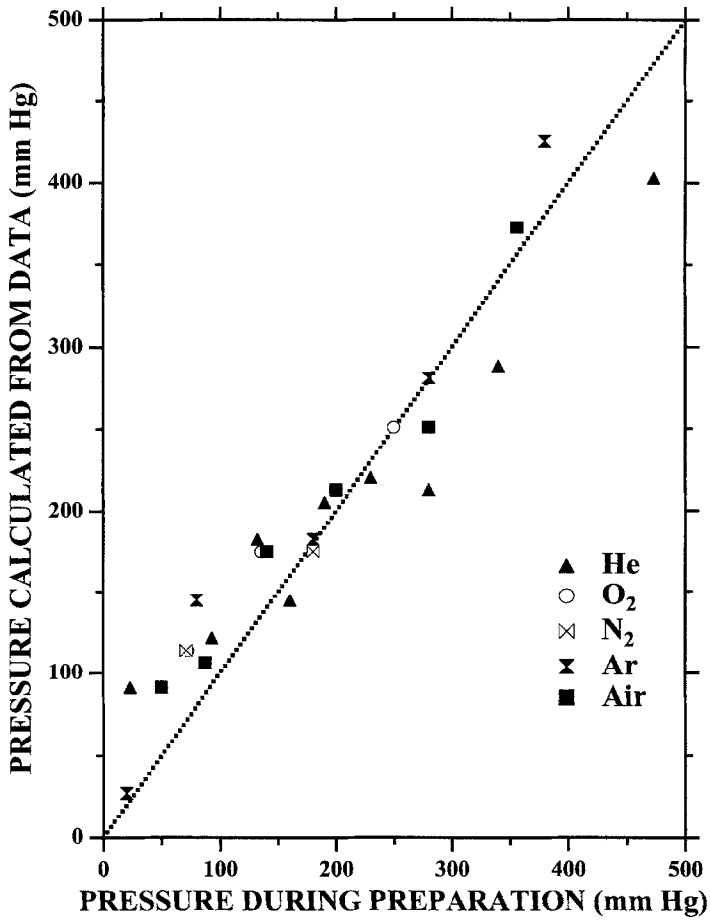

Fig. 26. Static versus diffusive equilibrium partial pressures. The abscissa shows the pressure at which gas has been stirred into the water, and the ordinate shows the pressure calculated from the application of the diffusion equation to the measured low amplitude, steady state bubble motion.

At this partial pressure there is no bouncing bubble, in agreement with the predictions of diffusion. All trapped noble gas bubbles are light emitting at 3 mm! At higher partial pressures noble gas bubbles can be driven to high enough amplitude to make light, but the bubble motion is unstable (see Figs. 27 and 28). We interpret the phase jitter of the pure noble gas bubbles at higher partial pressures as obeying the diffusion equation. At these higher partial pressures, the bubbles grow in size with every cycle of the drive in accordance with the diffusion equation, until they somehow become unstable and split off microbubbles (Barber et al., 1995), suddenly shrinking in size, as evidenced by the rapid glitches of Fig. 27. (This process has been called "recycling" by Holt and Gaitan (1996).) These phase glitches also show up as fluctuations in the light intensity of these noble gas bubbles, as shown in Fig. 28. The timescales of the growth of the bubble is however still in accord with the diffusion equation which can be used to calculate the amount of mass to flow into a bubble during one cycle of the drive (Löfstedt et al., 1995):

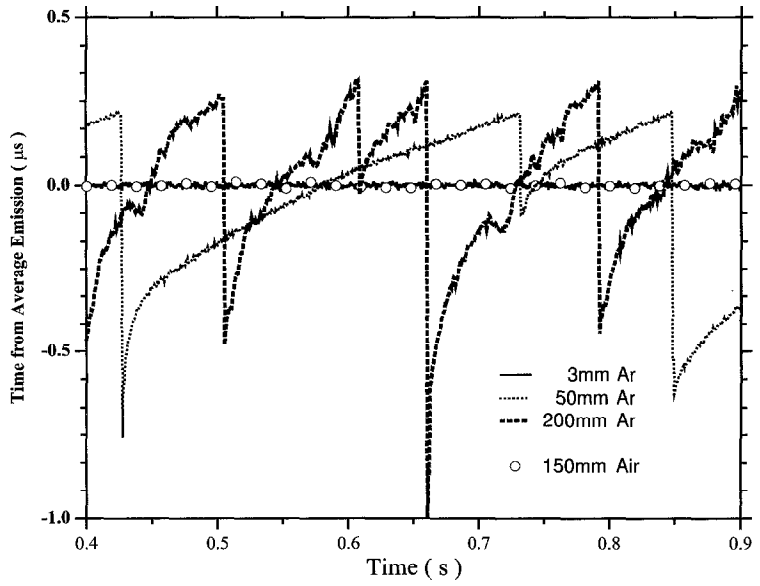

Fig. 27. Phase of light emission from an argon bubble. Shown is the time during the acoustic cycle at which light is emitted for 200, 50, and 3 mm argon bubbles. A data point was collected every tenth acoustic cycle. An air bubble at 150 mm is also shown for reference. Note that an air bubble is stable at partial pressures where diffusion is disobeyed, but argon bubbles are most stable where diffusion is obeyed.

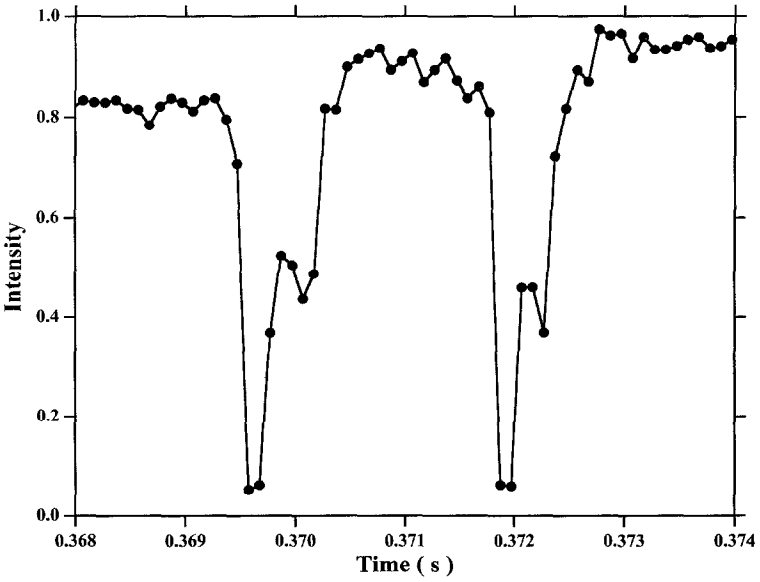

Fig. 28. Intensity of light emission from an argon bubble as a function of time at a partial pressure of 150 mm. Each cycle of the motion is captured. Large changes in the light intensity occur on the time scale of a single acoustic cycle.

$$\frac{\Delta M}{M} \approx \frac{3}{2}\left(\frac{T_a D}{R_0^2}\right)\frac{C_\infty - C_\infty(D)}{C_0}\frac{C_0}{\rho_0}\frac{R_m}{R_0} \approx 10^{-4} \tag{38}$$

where ρ_0 is the ambient density of the gas and $C_\infty(D)$ is the calculated equilibrium concentration from Eq. (34). To obtain this result one must supplement Eq. (33) with the rate of mass flow across the wall of the bubble due to diffusion,

$$\left(\frac{\mathrm{d}M}{\mathrm{d}t}\right)_D = 4\pi R^2 D\left(\frac{\partial C}{\partial r}\right)_{r=R}. \tag{39}$$

The time scales calculated from (38) are in qualitative agreement with the glitching rate displayed in Fig. 27.

Any theory of the ambient radius has to reconcile the stability of a sonoluminescing air bubble at 150 Torr and the stability of pure noble gas bubbles at 3 Torr, which is consistent with mass diffusion. Our logical, but unproven, deduction is that there is some unknown non-diffusive mass flow mechanism controlling the size of the sonoluminescing air bubble in water. The mass discrepancy might be accounted for by gas discharged along with the outgoing shock as the bubble reaches its most stressed point in time (Löfstedt et al., 1995), or, following quite the opposite reasoning, the hydrodynamic pulsations of the bubble might set up a macroscopic mass convection cell that breaks the spherical symmetry (Gould, 1973; Asaki et al., 1993). In any case the discharge must compensate for the diffusional influx given by (38).

Ethane bubbles were also found to give light at low partial pressures where the 10 : 1 expansion ratio is in diffusive equilibrium with the surrounding fluid. However, as the partial pressure is reduced below these levels, the ethane bubbles can sustain a 17 : 1 expansion ratio and again violate mass diffusion arguments (Barber et al., 1995). These radius-time curves are displayed in Fig. 29. The waterfall plot for ethane at 2 mm is shown in Fig. 30. All of these bubbles are light-emitting.

A consideration of waterfall plots (Löfstedt et al., 1995) of gas bubbles of various compositions reveals that the transition to light emission can occur after the (non-diffusive) decrease in size of a bouncing bubble as shown in Fig. 31. This graph is a detail of the waterfall plot of Fig. 32 which shows the transition to SL in a 5% argon in nitrogen mixture dissolved at 150 mm. The same situation can be seen for a 1% xenon in nitrogen bubble as shown in Figs. 33 and 34.

The diffusion equation enables us to calculate the time it would take a quiescent gas bubble in a fluid to dissolve away. This timescale (Epstein and Plesset, 1950)

$$t_D \approx \frac{1}{2}\frac{\rho_0 R_0^2}{D(C_0 - C_\infty)} \tag{40}$$

is about 1/3 s for a 5 μm air bubble in undersaturated water. One can compare this timescale with the "turn-on" times for sonoluminescing bubbles shown in Fig. 35 (Löfstedt et al., 1995). This is the time it takes the seeded bubble to start to glow. Pure noble gas bubbles start to glow immediately, even before they have reached the pressure antinode of the resonator. Noble-gas doped nitrogen bubbles turn on gradually (with time scales comparable to Eq. (40)) to reach their final steady intensity. An argon-doped nitrogen bubble driven near its upper threshold also shows modulations on the time scale of Eq. (40) as shown in Fig. 36. The time scale for a sonoluminescing air bubble to respond to an increased drive level is also measured in seconds as shown in Fig. 37, but the turnoff which acompanies a large boost in drive can occur over a hundred times faster than this time. When the

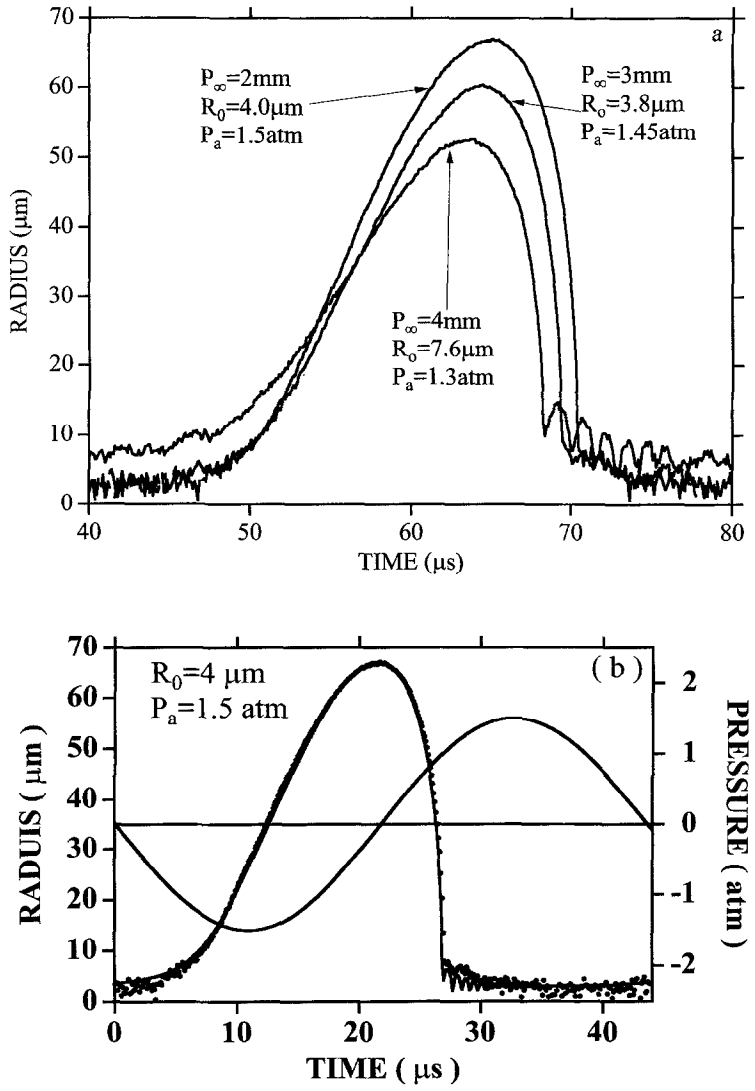

Fig. 29. Radius versus time curves for an ethane bubble at various partial pressures. In (a) are shown 2, 3, and 4 mm bubbles aligned with their proper phases relative to the sound field. The parameters for the 4 mm bubble obey diffusion whereas the 17 : 1 expansion ratio of the 2 mm (see (b), (c)) bubble is inconsistent with the steady state diffusion equation. In (b) the driving sound field is also displayed. The intensity of SL from these bubbles is so weak that its use as a trigger for the acquisition of traces yields spurious signals. To minimize this false triggering and allow for averaging of data a joint gate set by the SL flash and a 100–500 ns window, determined by the phase of the sound field at which SL should occur, was employed.

sound field is switched off the bubble returns to its ambient radius with the decay time of the sound field (5–10 ms) and then dissolves into the surrounding fluid as shown in Fig. 37C. Note that the bouncing bubble decays in about 1/3 of a second whereas the SL bubble decays in about 1/10 s. The difference in these times is consistent with the R_0^2 dependence in (40) but the absolute rates are

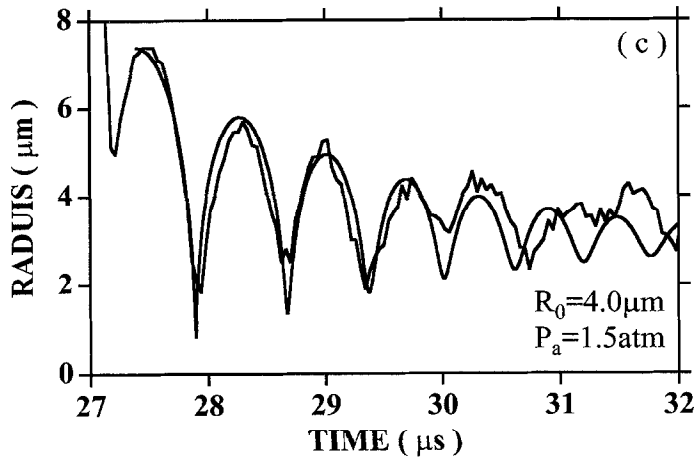

Fig. 29. Continued

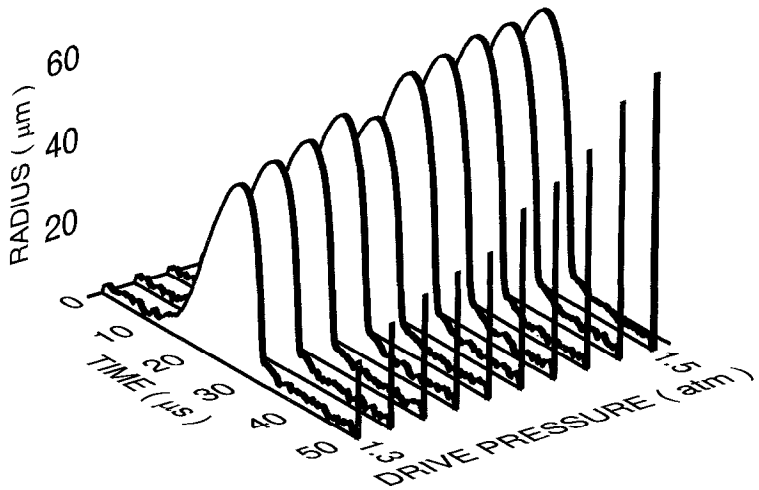

Fig. 30. Waterfall plot for a 2 Torr ethane bubble. The height of the vertical bars is proportional to the intensity of the emitted light. Note that all trapped bubbles emit light.

about twice as fast as the simplest diffusion approximation.

When the effects of surface tension are included, Eq. (37) is still the correct estimation of the consequences of the diffusion equation, however, R_0 is no longer the radius of the bubble when it is in equilibrium with the ambient pressure. The equilibrium radius is now $R_{0\sigma}$ as determined by Eq. (28). In terms of this quantity the scaling law (37) can be written in the equivalent form

$$\frac{C_\infty}{C_0} = 3\left(1 + \frac{2\sigma}{R_{0\sigma}P_0}\right)\frac{R_{0\sigma}^3}{R_m^3}. \tag{41}$$

A detailed comparison of the diffusion equation to the behavior of a 5% argon in nitrogen bubble at 150 Torr is shown in Fig. 38A. At low drive levels the measured and calculated ambient radii are in fairly good agreement. But as the drive level is increased the measured radius displays a

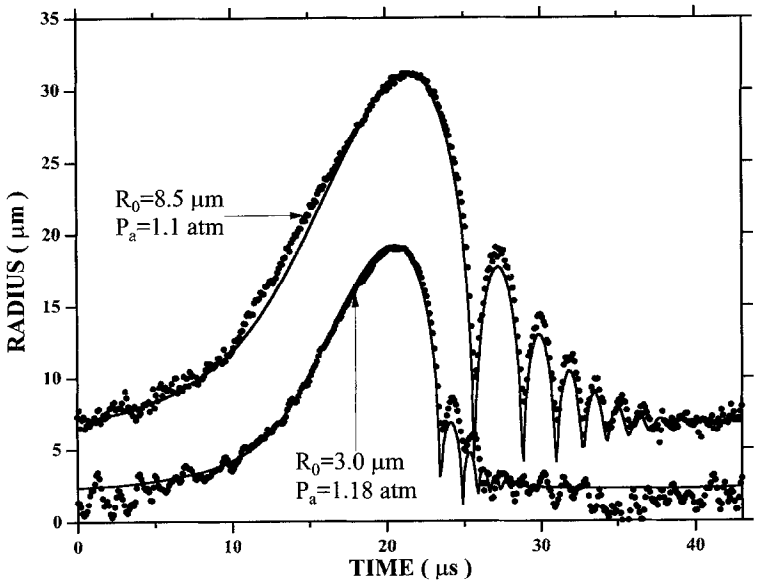

Fig. 31. Radius versus time for an argon-doped nitrogen bubble. As the drive is increased the larger bubble abruptly shrinks, and the expansion ratio increases. This bifurcation due to a non-diffusive mass flow mechanism occurs here below the transition to SL. The bubble has 5% argon in nitrogen and the gas is dissolved into the water at 150 mm.

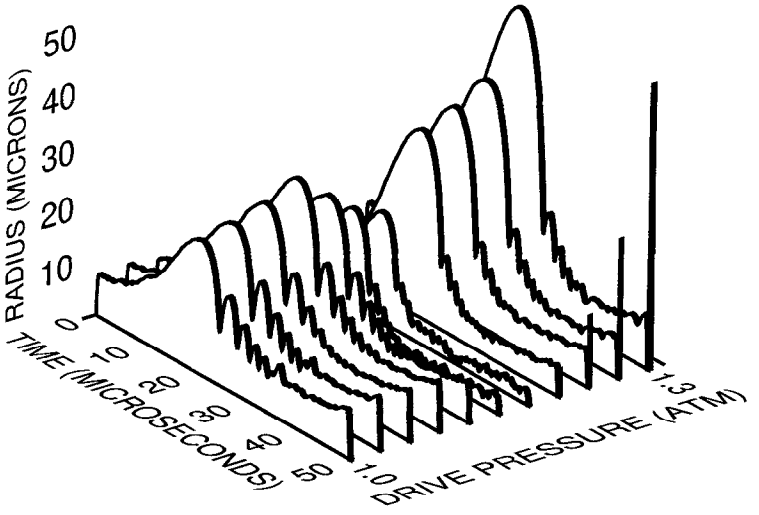

Fig. 32. Transition to SL for a 5% argon in nitrogen bubble. The vertical bars indicate the relative intensity of SL.

marked deviation from the requirements of diffusion. There is a drop and subsequent increase in R_0. The thick solid line indicates those bubbles which yield light. It is important to appreciate that the deviation from diffusive equilibrium already occurs for non-light-emitting bubbles. The maximum temperature reached when these bubbles collapse is about 1000 K. At such relatively low temperatures only a handful of nitrogen molecules are dissociated so that (at least for the bouncing bubble) an

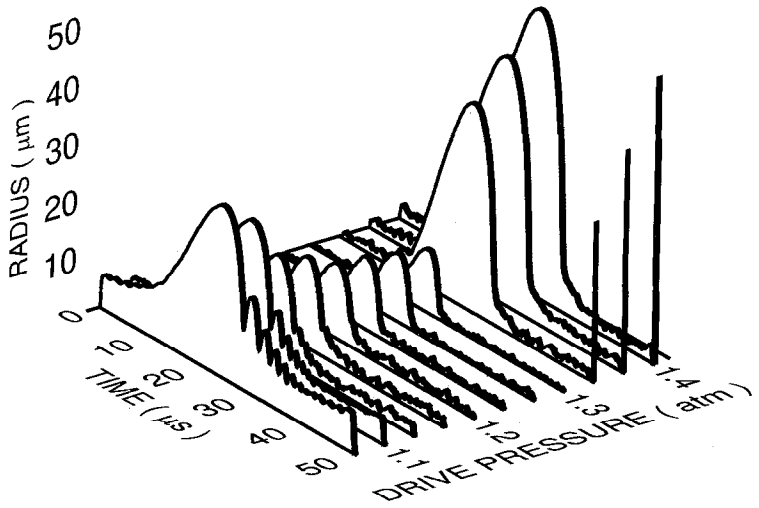

Fig. 33. Waterfall plot showing the transition to SL for a 1% xenon-doped nitrogen bubble The relative intensity of SL is indicated by the vertical lines. The transition to SL occurs only after the force of surface tension on the small bubbles is overcome by the driving sound field. The partial pressure of solution is 150 mm.

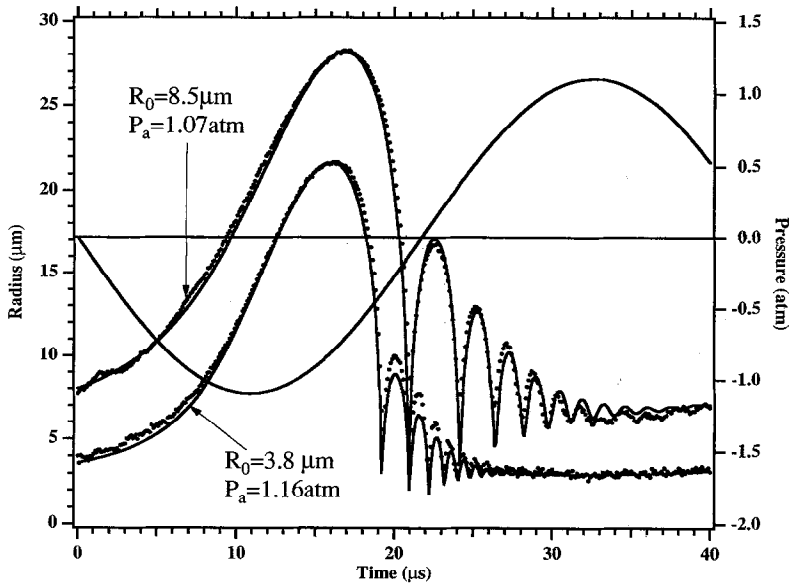

Fig. 34. Effect of anomalous mass flow on the radius of a 1% xenon in nitrogen bubble as the drive level is increased.

understanding of the non-diffusive mechanism lies outside chemistry (compare with Lohse et al. (1996)). We suggest that the additional mass flux originates with the outgoing acoustic spike (Figs. 1, 17) launced by the collapsed bubble. This spike is observed for both the SL and bouncing bubbles.

The curves which yield the equilibrium ambient radii for given sound field and concentration of gas in the water are calculated from the diffusion equation by substituting a solution to the RP equation

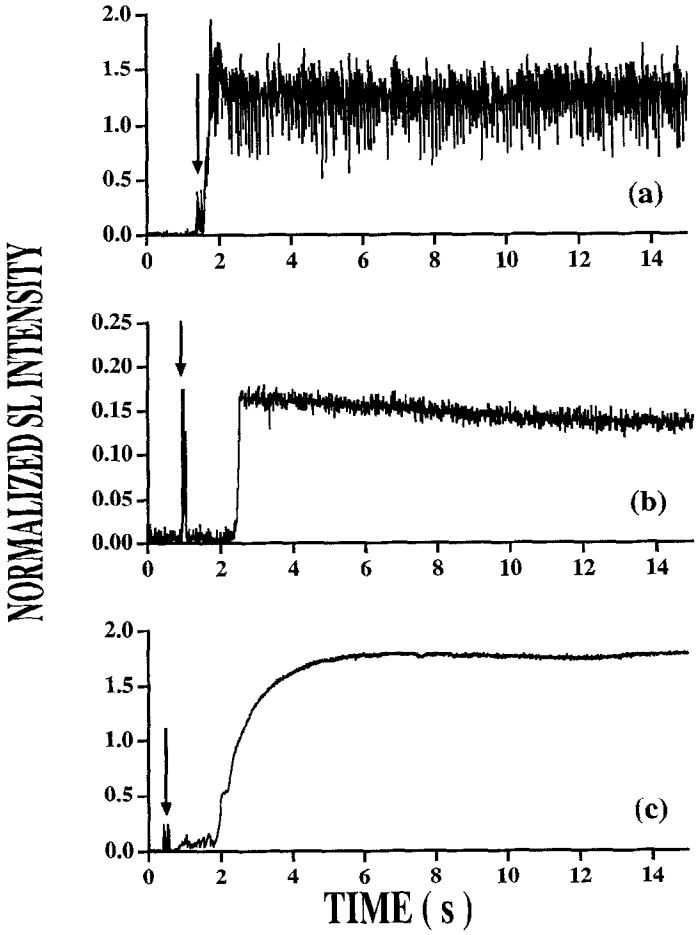

Fig. 35. Turn-on times for SL. Shown is the light intensity (normalized to an air bubble in water) as a function of time after seeding a bubble into an acoustically driven resonator. In (a) a pure xenon bubble at high drive levels lights up almost instantaneously. In fact, these bubbles are glowing as they leave the NiCr wire on their way to the velocity node of the sound field. (b) and (c) show the response of a xenon-doped nitrogen bubble. An arrow indicates a flash of light from an LED that is activiated by the current through the nichrome wire. This is the moment at which the bubble is seeded. Note the plethora of time scales that characterize the bubble driven at a high amplitude (c).

into Eq. (35) (Church, 1988, Crum and Cordry, 1994; Brenner et al., 1996). These curves are shown in Fig. 39 for drive pressures between 0.9 and 1.2 atm. For given C_∞/C_0 one picks off an equilibrium R_0. Since multiple solutions are possible, the issue of stability becomes important. It turns out in fact that the calculated equilibrium points plotted in Fig. 38, even at low amplitude where experiment and diffusion agree, are unstable according to diffusion. When the slope in Fig. 39 is negative, a fluctuation that increases the bubble radius brings it to a higher expansion ratio and thus further away from equilibrium with the surrounding gas fluid mixture, so that more gas will flow in causing the bubble to grow even larger. So for these bubbles the non-diffusive mechanism not only determines the size but also the stability even at low drive levels. For comparison, in Fig. 38B also are plotted the first stable solutions to the diffusion equation together with experimental values.

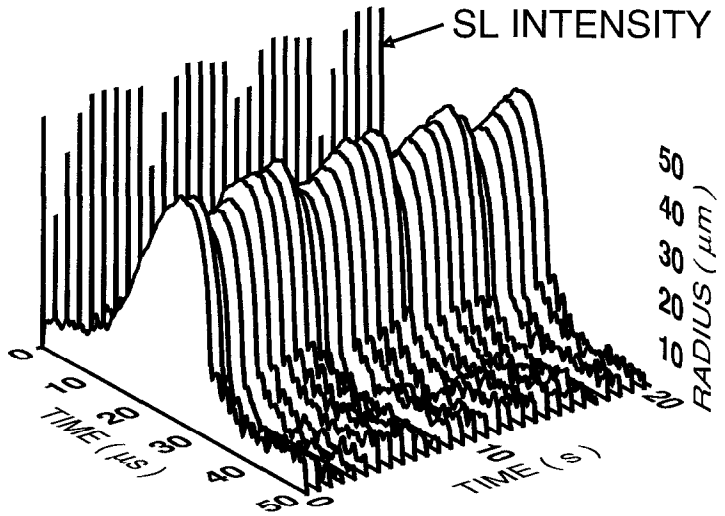

Fig. 36. SL intensity and bubble radius as a function of time for a nitrogen bubble with 5% argon at 150 mm. At a drive level just below the upper threshold of SL this bubble shows a variation on a long time scale of the order of 4 s. The acoustic frequency is 23 kHz.

For bubble radii under about 8 μm the cause of this instability is the surface tension as shown in Fig. 40 which compares bubbles with and without surface tension. For bouncing bubbles there remains the issue of whether multiple equilibria can be observed and why diffusively unstable bubbles are observed at low drive levels. An experiment aimed at observing multiple equilibria will have to be run in very pure water because as seen from the dashed line in Fig. 39 a realistic choice of damping washes out many of the wiggles. Also note that use of the isothermal equation of state for the slower parts of the cycle (as was used here) reduces the chances for multiple equilibria (This should be compared to Brenner et al. (1996) who used the adiabatic equation of state for the whole cycle.) Regarding the instability, it is important to realize that the corresponding growth rate is very slow. The time constant for exponential growth is

$$\left[\frac{D}{2R_0}\frac{\mathrm{d}(C_\infty/C_0)}{\mathrm{d}R_0}\left(3\frac{C_\infty}{C_0}\right)^{1/3}\frac{C_0}{\rho_0}\right]^{-1} \tag{42}$$

which for a 7 μm bubble at 1 atm is about 1/2 min. Finally, as we have emphasized, the onset of the non-diffusive mass flow mechanism will affect these comparisons.

According to the graphs in Fig. 41A multiple equilibria are also possible in the SL regime. Here there are two categories of such equilibria. We see that at $C_\infty/C_0 = 0.004$ there are two intersections with the response at 1.3 atm, with bubbles with ambient radii of 2.1 and 4.6 μm. The smaller bubble is strongly dominated by surface tension and is diffusionally unstable with a short time constant. The larger bubble is in fact the one observed in experiments. The other category is a true stable multiple equilibrium as can be seen where this partial pressure intersects the 1.4 atm drive level response at $R_0 = 7.0$ and 7.2 μm. These multiple equilibria again wash out at higher levels of damping, leaving one stable equilibrium state in the parameter range of interest. Furthermore, as shown in Fig. 41B the radius-time curves for these bubbles are not typical of SL. The afterbouncing rings through until

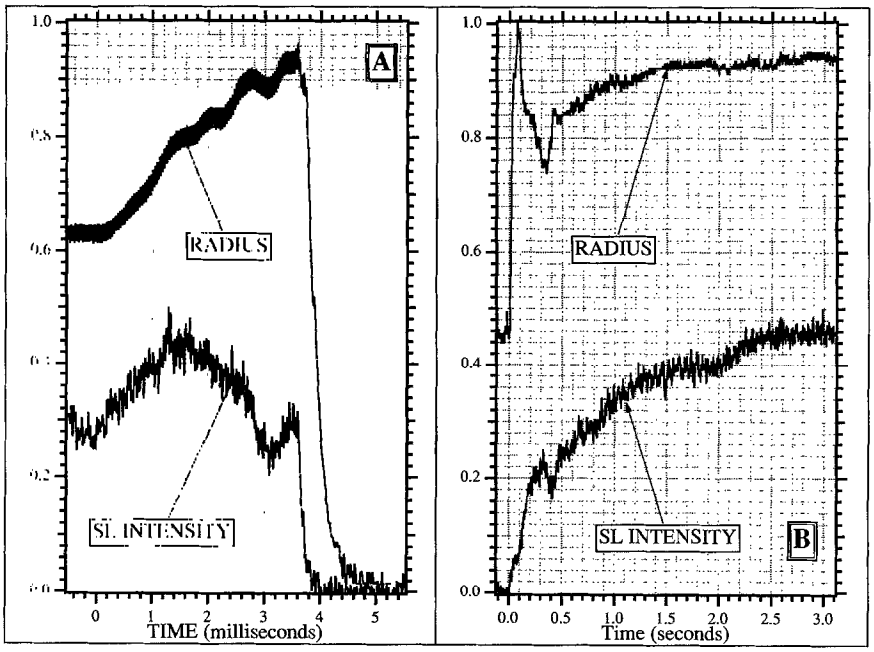

Fig. 37. Dynamic response of the intensity of sonoluminescence and of the bubble radius to a sudden change in the drive level. In (A) the drive is boosted above the upper threshold and after becoming brighter for a short time, the bubble disappears. In (B) the drive is boosted from weak to strong SL. After "gagging" (which can also be seen in (A)) the bubble achieves a new steady state during a long time scale measured in seconds. The signal has been averaged with a time constant of 100 μs for (A) and 10 ms for (B). Strictly speaking the results labeled "radius" are proportional to the product of R_m and the duration of the expansion. In (C) and (D) is plotted the square of the ambient radius as a function of time after the sound field is turned off. After an acoustic time of about 5–10 ms the bubble drops to its ambient radius and then dissolves. The bouncing bubble (D) (7 μm) dissolves in about 1/3 s and the SL bubble (C) (4 μm) dissolves in about 1/10 s. The 50% deviation of these times from Eq. (40) might be accounted for by surface tension and incresed resolution.

the next acoustic cycle. It is in fact the variation in the afterbounce resonances that accounts for the calculated multiple equilibria. As a rule the SL bubbles are sitting dead in the water as the next cycle begins. (The transition to SL for the systems studied to date is therefore not explained in terms of multiple diffusive equilibria, in constrast to the conclusions of Crum and Cordry (1994) and Brenner et al. (1996).)

Consider again the noble gas bubbles which are experimentally stable at 3 mm where diffusion theory also allows for an equilibrium bubble with an expansion ratio large enough for SL. A waterfall plot of such a bubble of argon is shown in Fig. 42. The experimental data for R_0 and P_a for this argon bubble are compared to the 150 mm, 5% argon in nitrogen bubble in Fig. 43. In the region of SL the data for these two systems are remarkably similar and in good experimental agreement with the parameters calculated from diffusion theory for a pure argon bubble. This again suggests that some rectification process that concentrates one of the gases in the bubble may exist (Löfstedt et al., 1995); however, the requirements of diffusion theory apply to each gas separately, and the general issue remains.

In conclusion, the stability and size of light emitting air bubbles (and higher amplitude bouncing

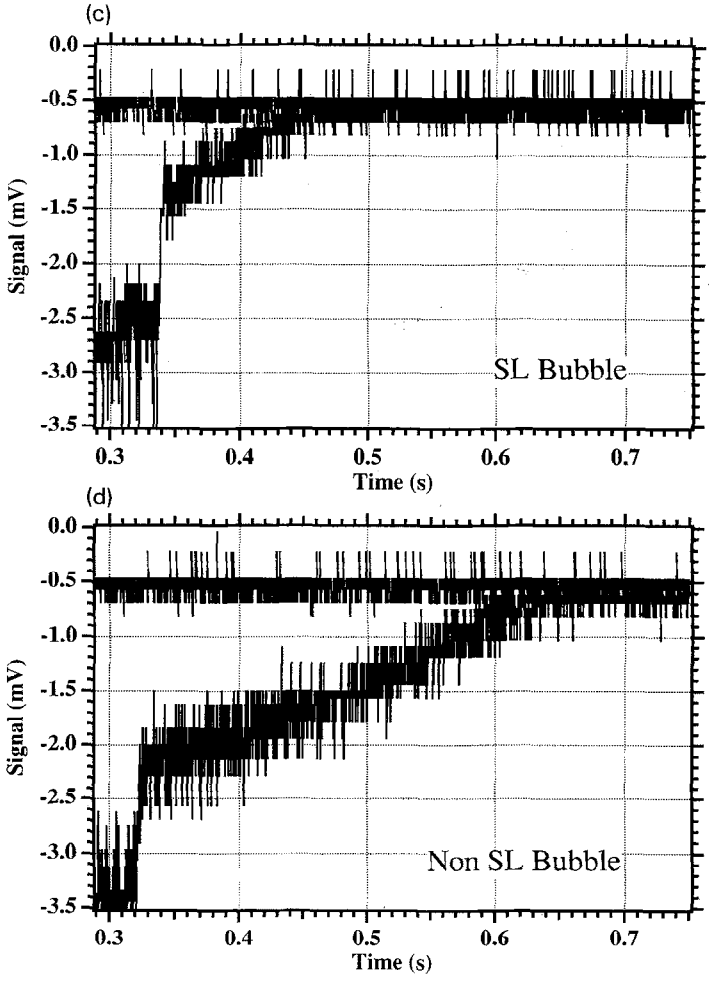

Fig. 37. Continued

bubbles) requires that a non-diffusive mass flow mechanism operates during each cycle of the sound field. The stability of light emitting noble gas bubbles at 3 mm is consistent with diffusion. At higher partial pressures the motion is also consistent with diffusion from cycle to cycle but after many cycles a "catastrophic" non-diffusive event occurs, such as a piece of the bubble splitting off. Although the diffusion equation permits multiple stability, experiments in water have not observed this effect. Whether other regions of parameter space will suppress the nondiffusive effects so as to make these states physically accessible remains to be seen.

7. Why is water the friendliest fluid for sonoluminescence?

One's ability to observe SL in a non-aqueous fluid is greatly enhanced by the use of xenon as the dissolved gas (Weninger et al., 1995). Pure helium and pure argon bubbles do not give light in

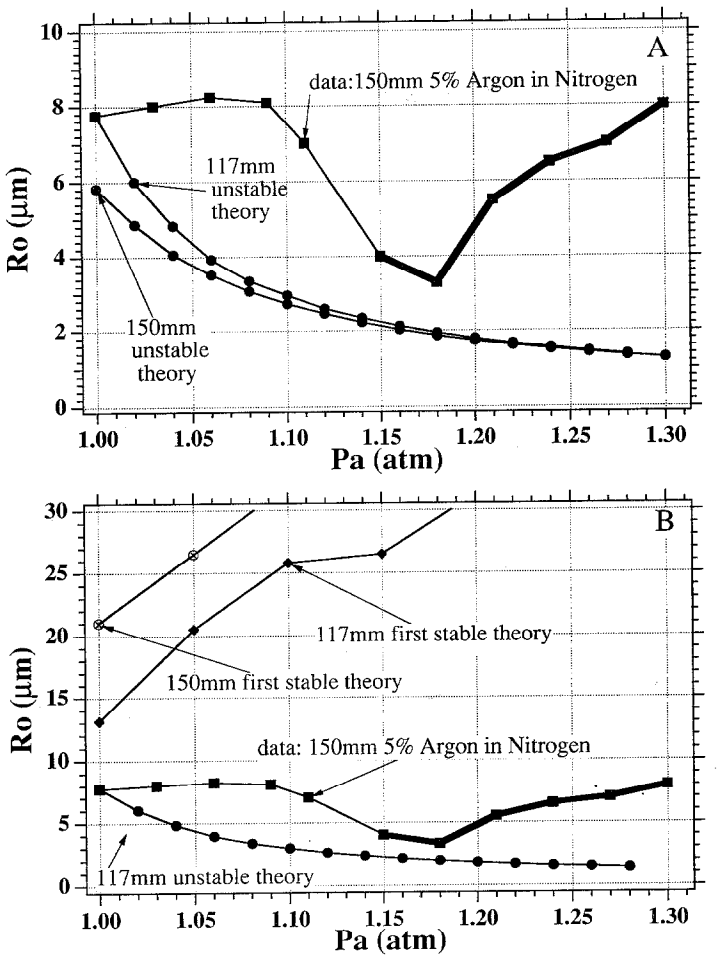

Fig. 38. Measured and calculated values of the ambient radius at which a 5% argon in nitrogen bubble at 150 mm would be in diffusive equilibrium, as a function of increasing drive level. In (A) is plotted the first (unstable) theoretical equilibrium point for 117 mm and 150 mm. The bubbles which make light are indicated with the thick solid line. In (B) is plotted the first theoretically stable equilibrium point. The deviation from the diffusion equation for this "air type" bubble is dramatic. At low drive levels, where bubbles do not make light, the deviation is much less and tends to zero. Similar measurements of the phase diagram of SL for air bubbles in nearly saturated water have been made by Holt and Gaitan (1996).

these fluids. Even in the xenon gas arrangement, the light emission is not nearly as stable as, say, air bubbles in water. In the non-aqueous fluids which we have studied (Fig. 44) the bubbles tend to jitter spatially a few mm around the pressure antinode which traps them. The phase of the light emission with respect to a trigger from the synthesizer that generates the sound field is typically spread over a few hundred nanoseconds, about a hundred times the phase wander for air bubbles in water. Yet another difference between the SL bubbles in non-aqueous fluids and air bubbles in water is that the maximum drive at which bubbles in non-aqueous fluids emit light is not well defined. Sometimes these bubbles simply stop emitting light after a short time (without being destroyed) and in other cases increasing drive amplitudes cause the bubbles to change their location in the resonant sound

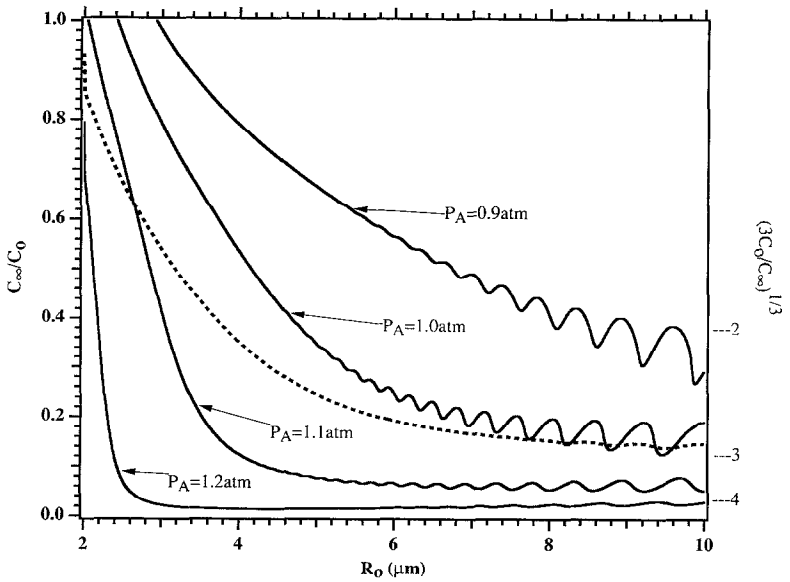

Fig. 39. Equilibrium concentrations as a function of ambient radius for various drive levels ranging from 0.9 to 1.2 atm. For the solid lines the viscosity is 1 centistokes and the surface tension is 70 dyne/cm. The dashed line has been calculated with a viscosity of 4 cSt and a surface tension of 50 dyne/cm. The wiggles indicate the presence of multiple equilibria, and the negative slopes are unstable if diffusion were the dominant process. These graphs have been calculated for $\gamma = 1.4$; the isothermal equation of state has been used for radii larger than the ambient radius and the adiabatic equation of state otherwise. On the right axis is plotted $(3C_0/C_\infty)^{1/3}$ which according to the scaling law Eq. (37) is the theoretically predicted value of R_m/R_0. This figure was calculated for an acoustic frequency of 26 kHz.

field while maintaining the same level of light emission. This tendency to wander away from the pressure antinode at increased drive is also achieved in non-light-emitting helium bubbles in silicone oil (Löfstedt et al., 1995), xenon bubbles in water at temperatures close to 0°C, and air bubbles in water at static pressures less than one atm (Barber, 1994). Fig. 45 shows measurements of the light emission from xenon bubbles in 1-butanol for various partial pressures and temperatures; note the breaks in the curve such as at −5°C for 250 mm partial pressure. Fig. 46 shows the light emission curves for xenon in ethanol.

These experiments display another general but as yet unexplained feature of SL, viz. that it produces more light at low temperatures (Barber et al., 1994). This was first observed for air in water as shown in Fig. 47, where cooling the water from 40°C to −6°C results in an increase in the light emission of over a factor of 100 (the increased emission is correlated with an increase in the maximum value of sound level that can be imposed on the SL bubble without destroying it). It seems to be fortunate happenstance for the discovery of SL that room temperature is not 20°C hotter. In fact, it seems that a static (ambient) pressure of one atmosphere also provides the most stable SL (as shown for an ethane bubble in Fig. 48). Our goal in decreasing the ambient pressure, P_0, was to increase the energy amplification characteristic of SL (Barber et al., 1991). The drive level required for SL, P_a', scales to the ambient pressure, and the acoustic energy density is proportional to the square of the drive level. At 1/4 atm of static pressure, the observation of SL would involve an energy focusing an order of magnitude greater than estimated in Section 1. The lowest ambient pressure at which SL

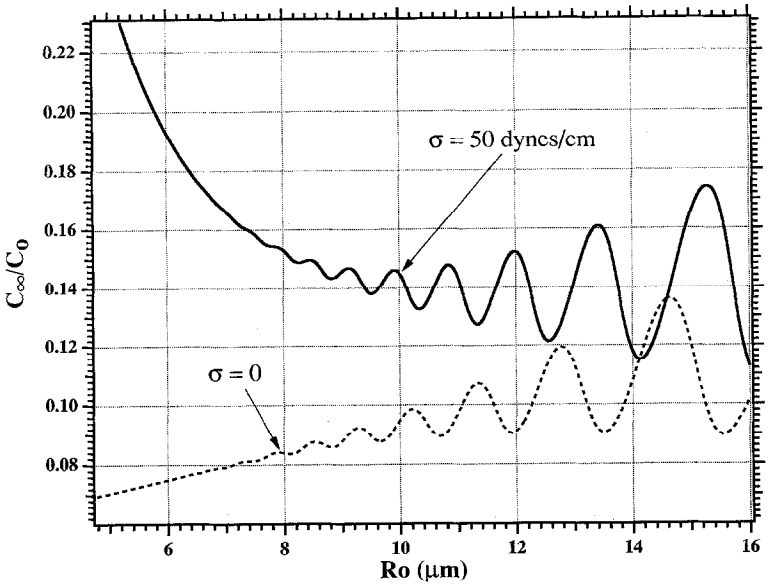

Fig. 40. Equilibrium concentrations for given radii showing the effect of surface tension. These curves are calculated from RP and the diffusion equation. The dashed line is for zero surface tension. The drive level is 1 atm and the viscosity is 4 cSt.

has been successfully observed is 1/3 atm (Barber, 1994). At these reduced pressures the bubble becomes not just dim but also poorly behaved. This observation suggests that SL from diatomics or non-aqueous fluids might be stabilized by increasing the static pressure. The experiment remains to be done.

Fig. 49 shows the dramatic reduction in SL that acompanies the addition of tiny amounts of impurity (butanol) to the standard air bubble in water (Weninger et al., 1995). In fact the strength of SL from such a fluid mixture is less than from an air bubble in the pure butanol, which as shown in Fig. 50 also yields a very faint signal.

The high solubility of xenon in nonaqueous fluids implies that diffusion processes lead to large fluxes of gas into and out of the bubble during each cycle. These oscillatory fluxes have an amplitude that is generally larger than the anomalous mass flow (38), and are given by (Löfstedt et al., 1995)

$$\left(\frac{\Delta M}{M}\right)_D \approx \frac{C_0}{\rho_0}\frac{\sqrt{DT_a}}{R_0}. \tag{43}$$

Since the solubility of xenon in butanol is 10^{-2} mole fraction as compared to air in water which is 1.3×10^{-5} mole fraction, one finds that $C_0/\rho_0 \approx 2.4$, which is so large that according to the diffusion equation, 20% of the gas in a xenon bubble in butanol must flow in and out during each cycle (for air in water the oscillatory mass flux is under a percent). Perhaps this effect accounts for the extreme jittering of these bubbles. However, gases with a lower solubility (such as helium for which C_0/ρ_0 is a factor of ten smaller) and presumably greater stability from the perspective of diffusion, do not yield SL from butanol, and so there is no simple interpretation of the role of the diffusion equation in SL from non-aqueous fluids.

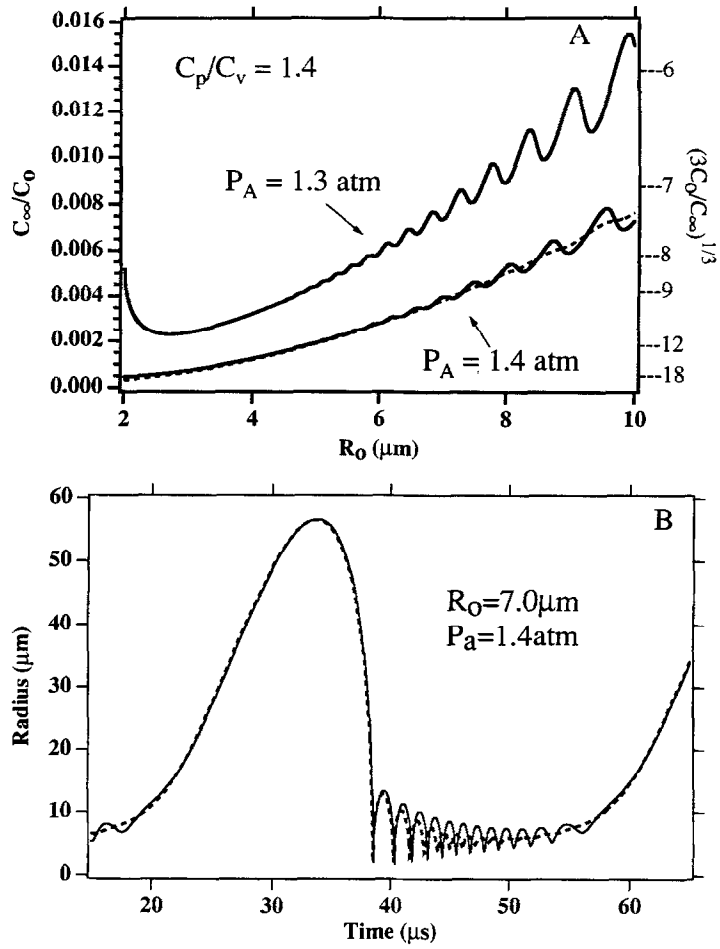

Fig. 41. (A) Equilibrium concentrations as a function of radii as calculated from diffusion for bubbles with SL parameters. Note that an increased viscosity (dashed line = 4 cSt, solid lines = 1 cSt) diminishes the multiple equilibria. On the right axis is plotted the expansion ratio as calculated from the scaling Eq. (37). The surface tension is 70 dyne/cm for the solid lines and 50 dyne/cm for the dashed line. (B) Calculated radius-time curve in the region of multiple equilibria for a 7.0 μm bubble driven at 1.4 atm at 30 kHz. Although the expansion ratio is about 8 : 1 the oscillations of this bubble persist until the next acoustic cycle. Such an effect has not yet been observed for an SL bubble. The solid line is for 1 cSt and the dotted line is calculated for 4 cSt. The ratio of the heat capacities is 1.4.

The wealth of parameters which characterize SL in these experiments tend to rule out a number of simple phenomenological correlations. For instance, the solubility of gases in fluids (Battino et al., 1984; Pollack et al., 1984; Fogg and Gerand, 1991) does not appear to be of crucial importance because the solubility of xenon in dodecane is over a thousand times greater than the solubility of air in water. Similar remarks apply to the fluid's vapor pressure, which for dodecane is 10^4 times smaller than for ethanol, and to the fluid's dielectric constant, which is 80 for water, 25 for ethanol and 2.3 for silicone oil. The relative insensitivity of SL to chemistry suggests that helium gas dissolved in liquid argon could constitute a simple and thus paradigmatic system for the study of SL. Unfortunately our

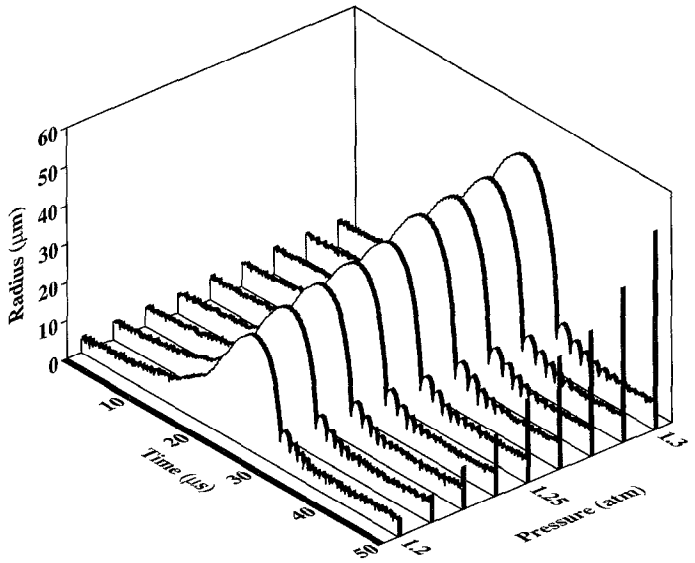

Fig. 42. Waterfall plot of an a 3 mm argon bubble in water. All of these bubbles emit light; the relative SL intensity is indicated by the vertical bars. At one pressure step above the highest level shown the bubble blinks and dies, and at one pressure step below the lowest drive level the bubble dissolves.

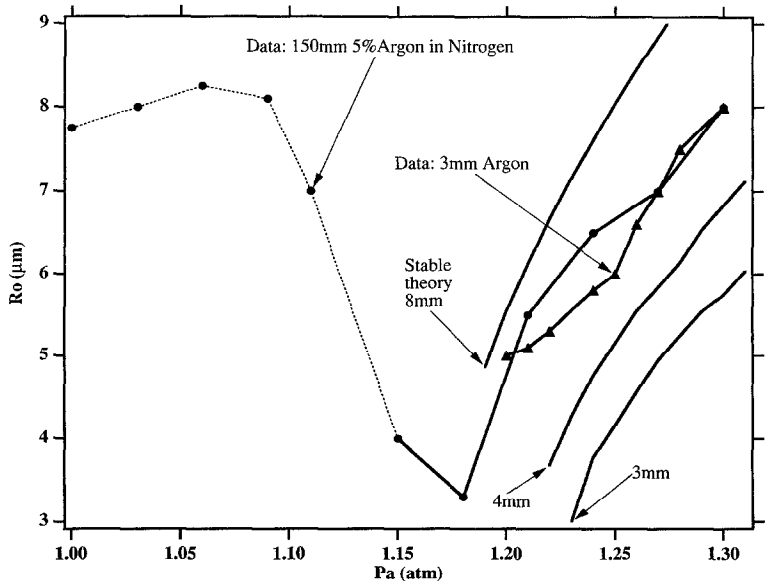

Fig. 43. A comparison of measured drive levels and ambient radii for a 3 mm argon bubble and a 150 mm 5% argon in nitrogen bubble. In the region of SL the bubble parameters overlap, and furthermore are in reasonable agreement with diffusion theory applied to a pure argon bubble. For the theory the frequency is taken to be 23 kHz, $\gamma = 5/3$, surface tension is 50 dyne/cm and kinematic viscosity is 0.04 cm^2/s. Note that for the 3, 4, 8 mm theory plots there is no solution below the lowest value plotted.

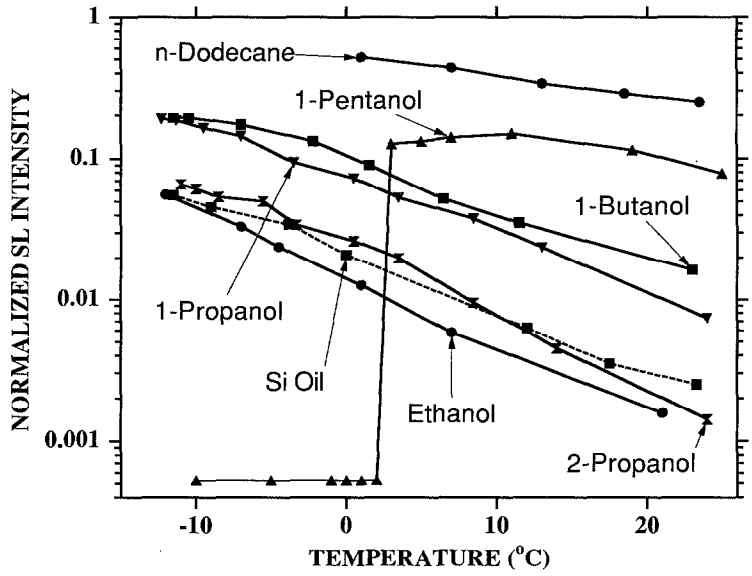

Fig. 44. Intensity of SL from a single xenon bubble trapped in various fluids as a function of temperature (normalized to 150 mm air in water at room temperature). These are the largest signals that can be observed for 30 s or longer. For 1-pentanol below 1°C non-light-emitting bubbles can be sustained. By sweeping the drive level a signal of 1–2 mV (0.1 normalized) can be attainced for about 50 ms.

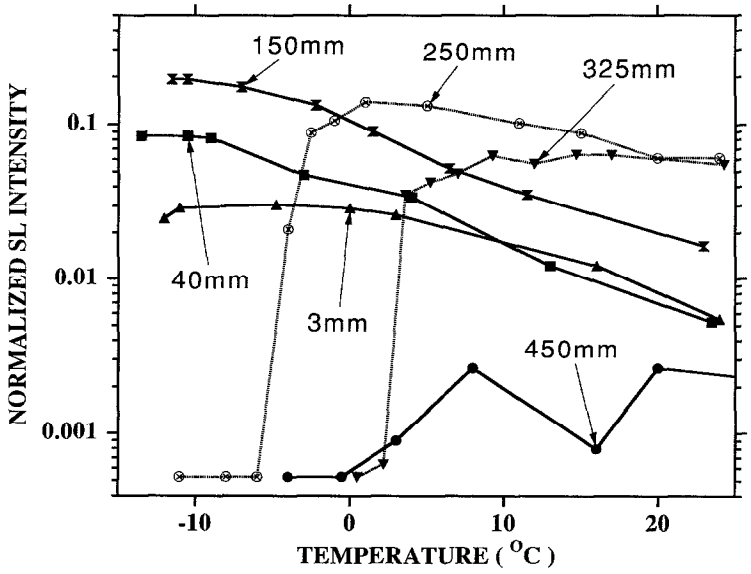

Fig. 45. Intensity of SL for a single xenon bubble in 1-butanol as a function of partial pressure and temperature. For the 250 mm and 325 mm curves at cold temperature the same comments given for 1-pentanol in Fig. 44 apply.

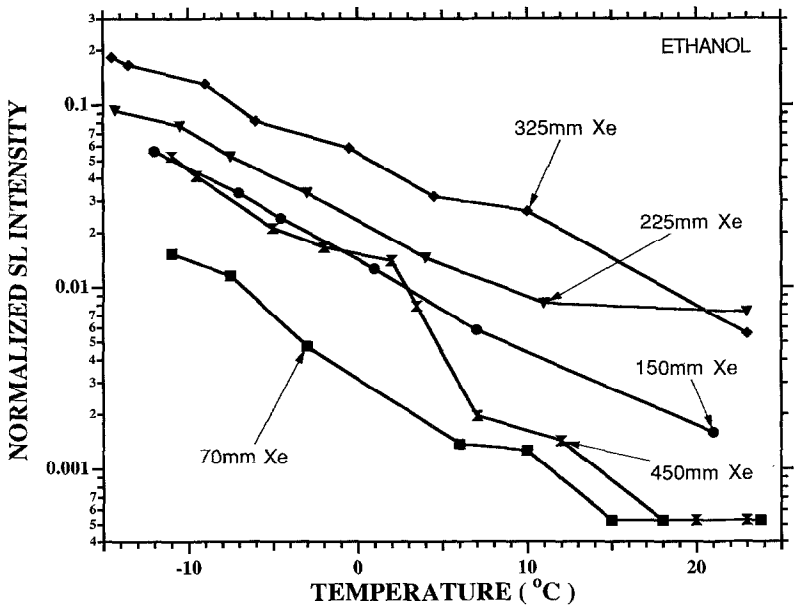

Fig. 46. Intensity of SL from xenon in ethanol.

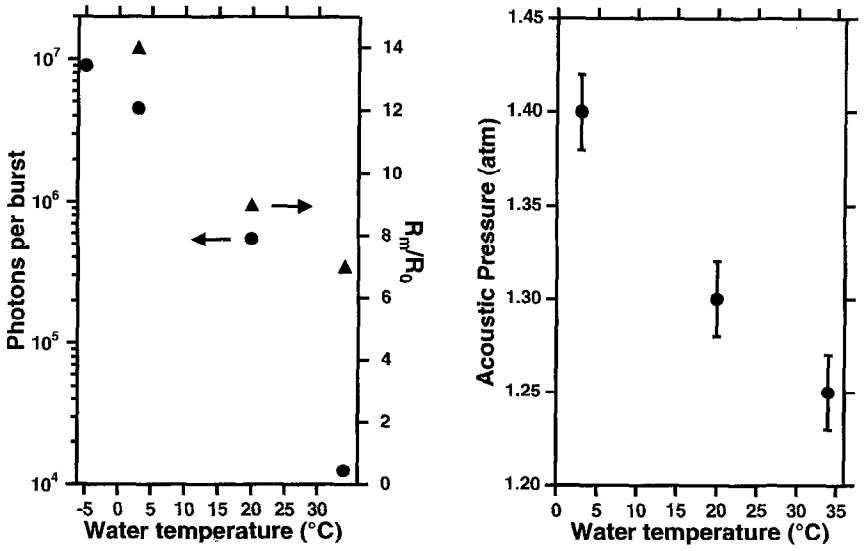

Fig. 47. Intensity of SL from an air bubble in water as a function of temperature (A) and the acoustic pressure (maximum drive levels at which SL is stable) for which these intensities are achieved (B). The increase in light output as the ambient temperature is lowered is correlated with the higher drive level at which SL can be maintained.

grasp of theory does not enable us to predict whether such an experiment would work. If it were attempted, a 3 mm partial pressure solution of helium in liquid argon would be the logical starting point of the search through that portion of parameter space.

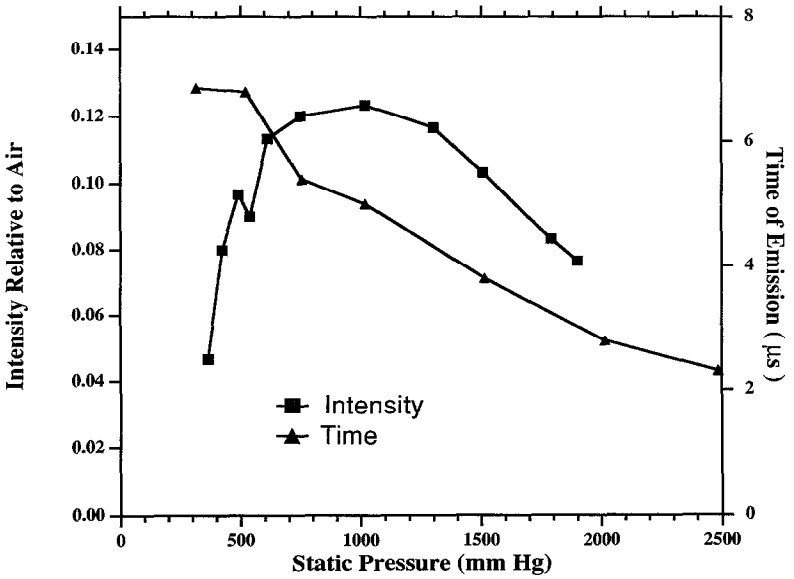

Fig. 48. Intensity of SL for an ethane bubble (dissolved into water at a partial pressure of 2 mm) as a function of the ambient (static) pressure. Also shown is the phase of emission of SL. The earlier time of emission at higher pressure is due to the fact that those bubbles spend less time at the maximum radius. At a static pressure of 4–5 atm "tap" water can display stable SL. Although tap water is saturated as it comes out of the faucet it becomes degassed relative to $C(P_0)$ as P_0 increases.

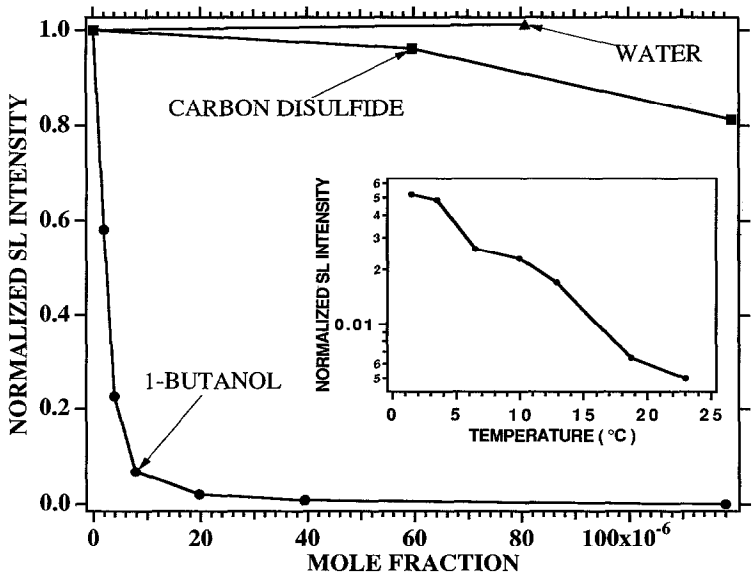

Fig. 49. Intensity of SL as a function of impurity concentration in the water.

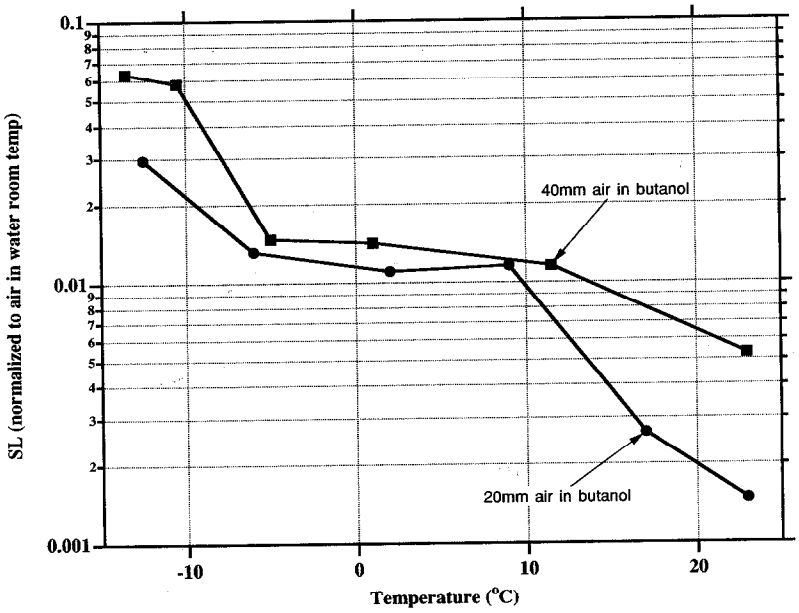

Fig. 50. SL from an air bubble in butanol as a function of ambient temperature.

8. How energetic are the emitted photons?

Fig. 51 displays the uncalibrated spectrum of a helium bubble in water, taken with an ARC 0.275 m spectrometer with a 1200 lines/mm grating blazed at 300 nm and a Hamamatsu R2027 photomultiplier tube (Hiller et al., 1992, 1994, 1995; Gaitan et al., 1996). The key features are

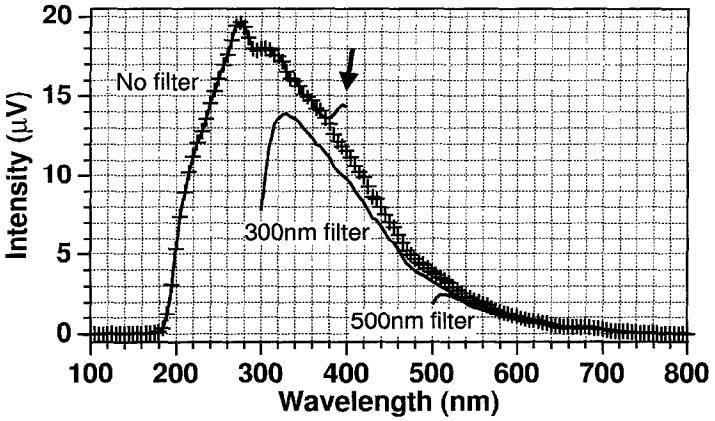

Fig. 51. Raw data showing the uncalibrated spectrum of light emitted by a sonoluminescing bubble of helium in water. Note that the spectral response turns on at about 185 nm (6.5 eV). Due to the broadband nature of the emission, order-sorting filters must be used to suppress second-order diffraction peaks. The arrow points to the onset of a deviation in the spectrum from its real value that would occur if such filters were not used. Here this effect sets in at about 380 nm. The physical spectrum is reconstructed from data taken with no filter as well as filters which cut off light below 300 nm and 500 nm. The actual spectrum must be corrected for the response of the grating, photodetector, and transmission through water and quartz.

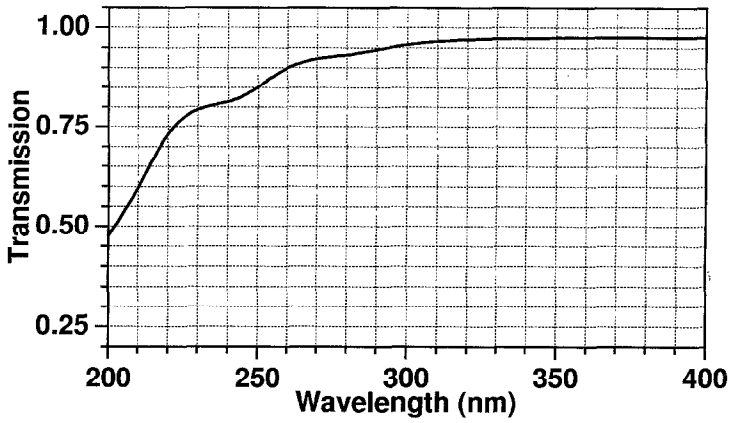

Fig. 52. Transmission of light through water and one wall of the GM quartz flask. Data which are corrected for transmission uses this curve.

already apparent in this plot: the broad band nature of the light (i.e. no spectral lines at the 10 nm FWHM resolution employed), and the persistence of a signal down to a wavelength of 190 nm which is up to an energy almost 6.5 eV. The loss of signal at this wavelength is in part due to the fall off in response of the grating at the diffraction angle corresponding to this wavelength. The fundamental cause for the cutoff of the spectrum at this point is due to the attenuation of light travelling through water. Water does not become transparent again until well into the X-ray regime (Robinson Painter et al., 1969). To obtain values for the spectral radiance which are corrected for the response of the grating, mirrors and photodetector, we use calibrated sources (quartz-tungsten-halogen and deuterium lamps). Even if water would not cut off light in the far UV there still would be no established procedure for calibrating the spectrum below 200 nm. It is also important to use order-sorting filters to suppress second-order scattering by the grating. The arrow in Fig. 51 shows the onset of a signal due to second-order scattering when such a filter is not used. Estimates of the effect of transmission through water and the resonator walls on the spectra are obtained by measuring the attenuation of light focused to pass through the center of the resonator. These correction factors, when used, are shown in Fig. 52. The noise level was reduced by acquiring data with a lock-in amplifier synchronized to the acoustic frequency, which is also the rate at which the SL light emission turns on and off. Putting all these effects together yields typical calibrated spectra for SL, as shown in Fig. 53 for helium dissolved at 150 mm at various temperatures.

The spectrum from various noble gases at room temperature and and 0°C are shown in Figs. 54 and 55 (Hiller et al., 1994). In these experiments the gas is dissolved in water at a partial pressure of 3 mm. Fig. 56 shows the spectrum from noble-gas-doped nitrogen mixtures. It is apparent that the long wavelength limit of virtually all of these gases is similar, but the bubbles with xenon yield a decreasing emission as 200 nm is approached. The broad spectral peak exhibited by xenon may be indicative of the light-emitting mechanism but it may also be due to an enhanced attenuation of the UV light in and near the bubble for this system. The spectral density of a xenon bubble increases slightly in the ultraviolet at lower drive as shown in Fig. 57. The spectrum of xenon in ethanol and butanol is shown in Fig. 58 together with the spectrum of an ethane bubble in water, Fig. 59 (Weninger et al., 1995). Aside from the similarity of these spectra to those already shown

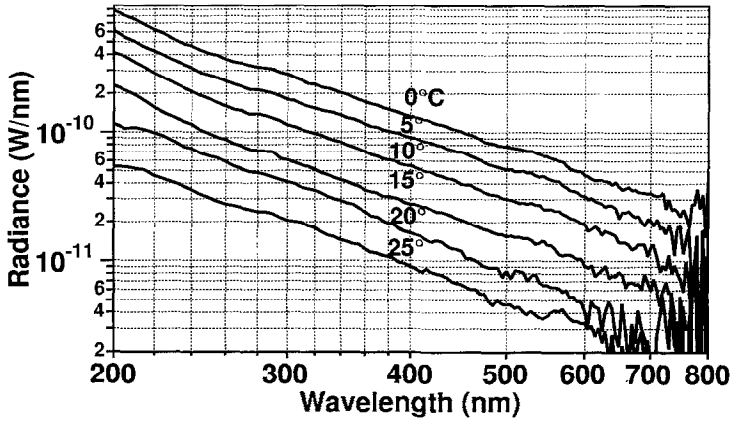

Fig. 53. Corrected spectra for a 150 mm bubble of helium in water at various temperatures.

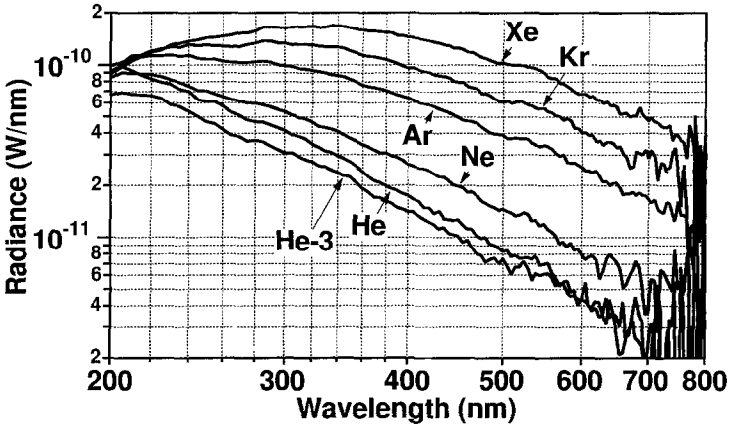

Fig. 54. Room temperature spectra of various noble gases in a cylindrical "supracil" resonator. No transmission corrections have been used. The gases have been dissolved at 3 mm.

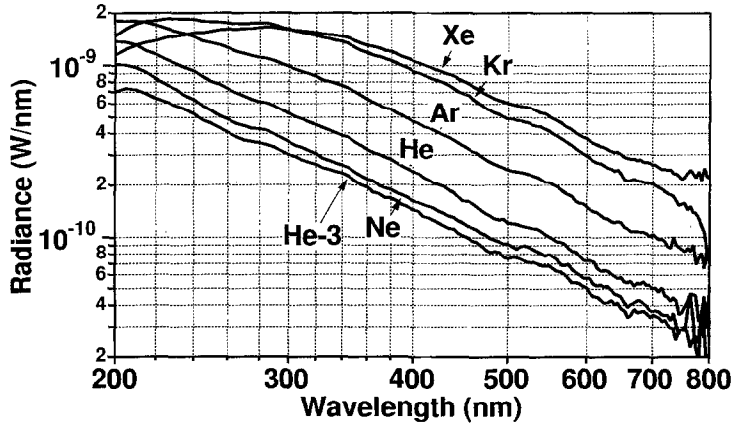

Fig. 55. Freezing point spectra of various noble gases in water. The gases have been dissolved at 3 mm, and the spectra are not corrected for transmission.

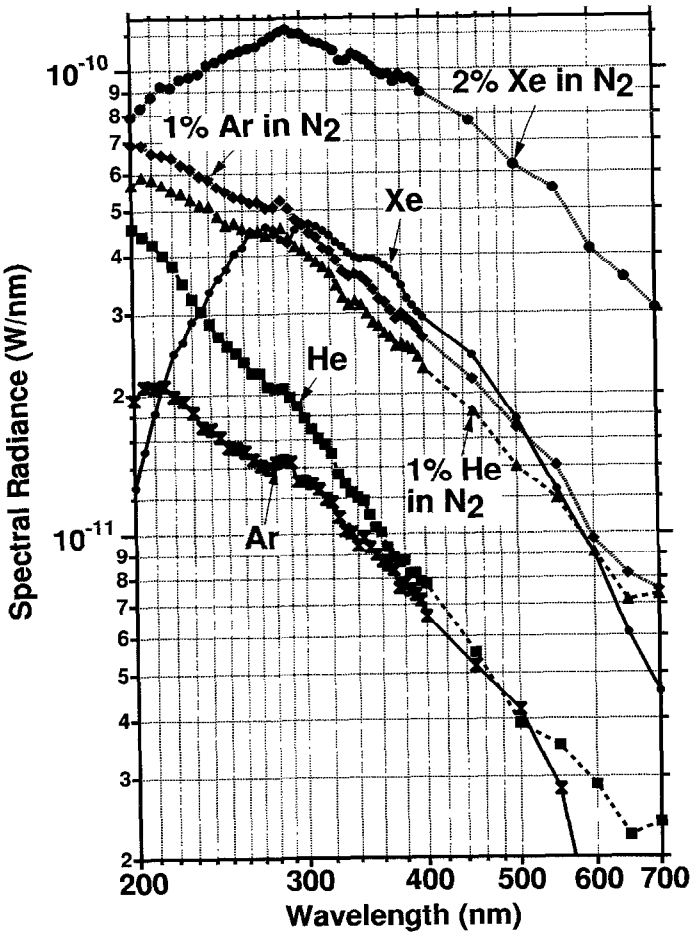

Fig. 56. Spectrum of SL for various gas mixtures dissolved into water at 150 mm and $T = 24°C$. Data have been corrected via use of Fig. 52. Note that although helium is dimmer than xenon it has a greater spectral density in the ultraviolet.

it is noteworthy that the Swan lines are absent (Suslick and Flynt, 1987). These are lines that are emitted by excited states of carbon molecules.

The similarity of the spectra raises the possibility that each spectrum in fact has the same shape, but its position on the wavelength axis is scaled. Then each measurement simply displays a different window of the same spectrum. In this case one can ask where the spectrum of, say, He at 20°C would reach its maximum so as to have the same energy as xenon-doped nitrogen at 0°C. That value turns out to be over 150 eV. The existence of such energetic photons cannot be ruled out experimentally at this time, because a technique for measuring the spectrum beyond the cutoff of various fluids has not yet been developed.

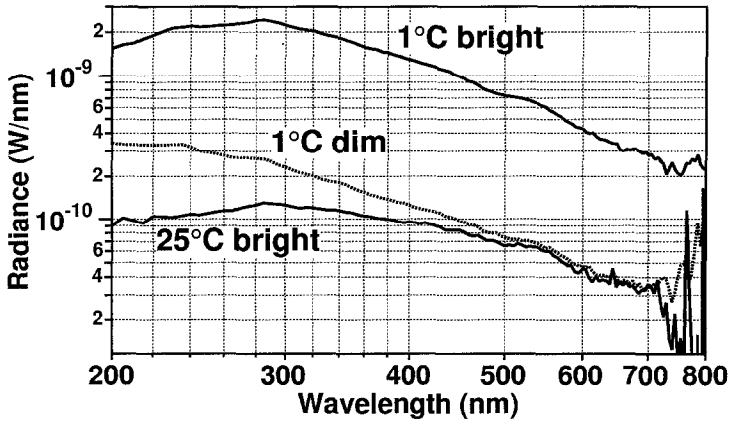

Fig. 57. Spectrum of 2% xenon in nitrogen dissolved at 150 mm showing the variation of the spectral density with drive level.

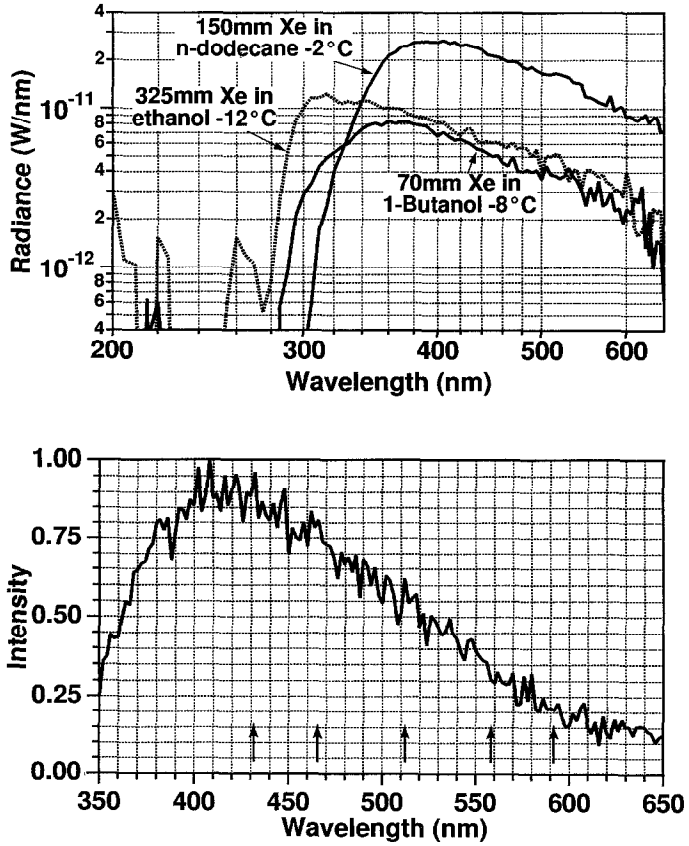

Fig. 58. Spectrum of xenon in various organic liquids. The lower graph (xenon in dodecane) was obtained at a resolution of 1 nm and shows no evidence of the Swan lines which are emitted by excited carbon molecules. These lines have been observed in experiments designed to measure transient SL.

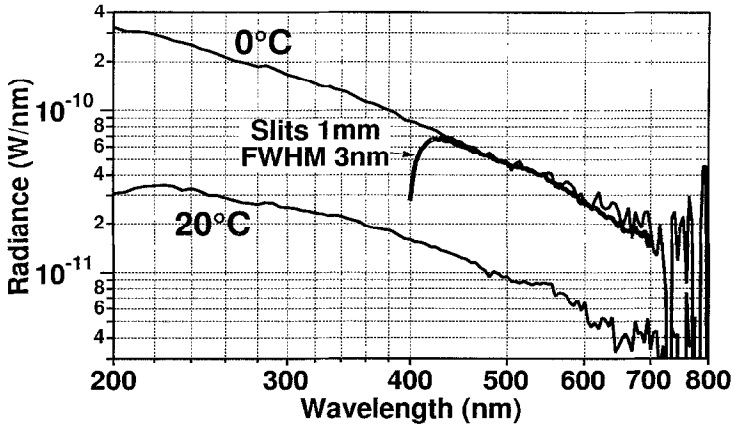

Fig. 59. Spectrum of a 2 mm ethane bubble in water.

9. How short are the flashes?

The fastest time scale for sonoluminescence is more than ten times shorter than the shortest time scale of 500 ps (Barber et al., 1997) that has been resolved in the bubble motion. This very short time scale is the width of the individual flashes of sonoluminescence (Barber and Putterman, 1991). Fig. 60 displays a comparison of the response of a microchannel-plate photomultiplier tube with a rise time of 170 ps to a flash of SL and a flash of purple light from a 34 ps laser pulser (Barber et al.,

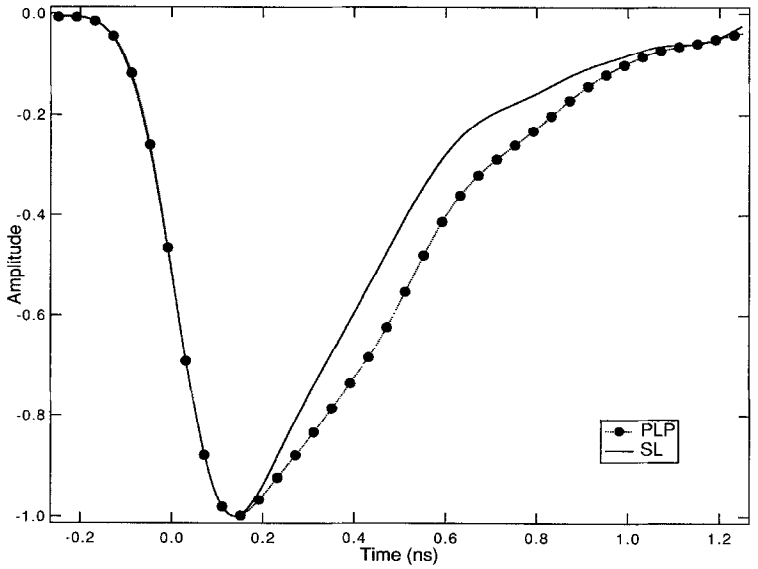

Fig. 60. Voltage versus time at the output of a two-stage microchannel-plate photomultiplier tube with a rated rise time of 172 ps. The solid line shows the response to SL, and the dashed line is the response to 410 nm pulses of 34 ps duration from a laser. These curves correspond to the recording of about 25 photoelectrons. After passing through the delay line and 20 dB attenuator a single photoelectron corresponds to a peak amplitude of 2 mV. A comparison of the graphs indicates that the flash of SL is shorter than 50 ps and furthermore the faster return towards zero of the SL signal indicates that the laser has some after-ringing. The reason for the quick turnoff of SL is unknown.

1992). On the graph the rise-times of the two responses are indistinguishable. Typically the measured rise time for the pulser is about 172 ps and for SL it is about 172–176 ps. From this comparison one can set an upper bound of 50 ps on the duration of the flashes of SL. It is interesting to note that the PMT response to the SL flash returns towards zero more rapidly than the response to the laser pulser. This occurs because the turn-off for SL is clean whereas the pulser is characterized by after ringing. To acquire these traces one must face the difficulty that the oscilloscope requires a trigger that is 20 ns in advance of the signal and that for SL there is no such advance trigger. To overcome this problem, the signal from the photodetector is split into a trigger pulse and a signal pulse. The signal is sent through a high bandwidth delay line so as to arrive after the trigger. The average of many such acquisitions is shown in the figure.

In view of the large parameter space for SL it would be valuable to have a means of resolving the flash width and measuring its value in various situations. To this end a streak camera should be able to resolve the width down to about 2 ps (Barber, 1992). There are two ways to apply this device. One is to collect enough light so that a single sweep catches enough photons to resolve the flash. The difficulty here is to overcome chromatic aberration or, if mirrors are used, to overcome various geometric distortions. The other method is to overlay many acquisitions. Here the problem faced is that the camera must be triggered prior to the arrival of the light. Now it is the light and not an electrical signal that must be delayed. If a signal is recorded at the resolution of the camera, it is essential to distinguish it from dark noise by dispersing it in time with a prism or an optical fiber. The noise will not disperse.[1]

If enough light from a bubble could be collected so that the flashes could be resolved by a streak camera, then it might be possible to measure a time-resolved spectrum of SL. Such data would show whether the UV portion of the spectrum preceded the red portion and would thus yield important information about the light-emitting mechanism and the energy focusing process.

If the output of the photodetector is sent to a time interval meter the jitter in the time between flashes of light can be measured (Barber et al., 1992). As shown in Fig. 61 the standard deviation of the time between flashes is shorter than 50 ps, which in fact is about equal to the stated jitter of the instruments used to measure the SL. It is surely remarkable that the successive supersonic implosions which generate SL should occur with a clock-like precision that is better than a part per million of the imposed acoustic frequency. For reference, the quality factor of the sound field is about only 1000 (Barber and Putterman, 1991).

The largest SL signal measured to date has over 10^7 photons per flash; assuming an average photon energy of 5 eV and a flash width of 50 ps yields a peak power over 100 mW. (The conversion factor of 1 joule = 6.2×10^{18} eV is useful.) Although ps lasers can be very powerful, a cheap UV picosecond light source still costs over $20 000, and has the same power as SL which can be built for $200.

The lowest frequency sound field for which SL has been observed is in the audible range under 10 kHz (Barber and Putterman, 1991). Due to the processes of fluid mechanics, this 100 μs input period results in the emission of a macroscopic pulse of light whose duration of 50 ps is shorter than the time scales that are resolved in high-energy physics experiments.

It was our measurement (Barber and Putterman, 1991) of the picosecond flash widths and synchronicity that fostered general interest in SL, even though SL had been discovered over 50 years

[1] According to this criterion, Moran et al. (1995) measured dark noise and not SL, and so their upper bound on the SL flashwidth is invalid.

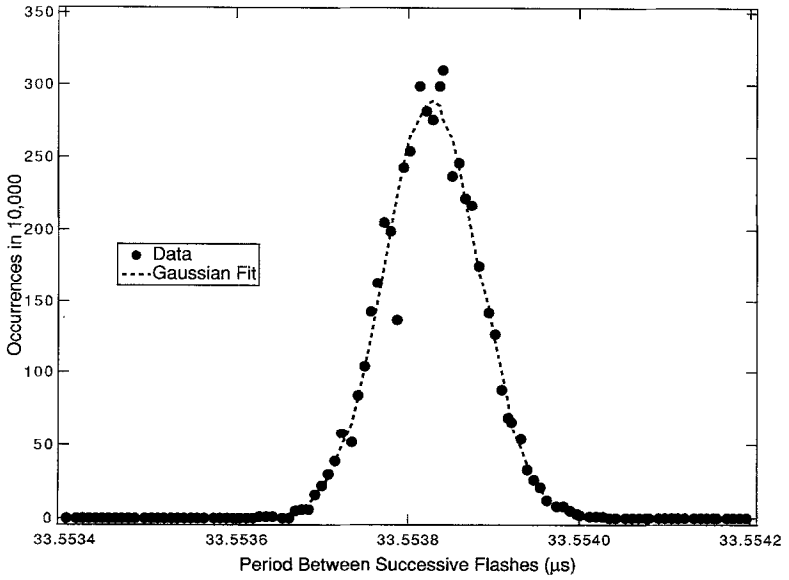

Fig. 61. Histogram of events versus period between flashes for SL. The jitter in the time between flashes is less than 50 ps.

earlier by Frenzel and Schultes (1934). In their apparatus, clouds of cavitating bubbles were generated by sound fields more intense than those quoted above. These bubbles would emit light in a transient and unpredictable fashion. It was the discovery (Gaitan, 1990; Gaitan et al., 1992) that, at least for air in water, SL could be obtained from a single bubble by degassing the water, that made our synchronicity (Barber et al., 1992) and light-scattering experiments (Barber and Putterman, 1992) possible and facilitated the measurements of the flashwidths (Barber and Putterman, 1991). The study of transient SL has a long history (Walton and Reynolds, 1984; Löfstedt, 1995; Putterman, 1995) and it remains to be seen if the physics of each bubble in the Frenzel and Schultes apparatus probes the same physics as a single bubble trapped at a velocity node. The long turn-on time for SL from a single bubble (Fig. 35) (Löfstedt et al., 1995) suggests that these phenomena are quite different. Nevertheless, a calibrated spectrum of transient SL in a resonant system has not yet been taken. The spectral lines observed in transient SL (Suslick and Flynt, 1987; Verrall and Sehgal, 1987; Matula et al., 1995) might be due to a fundamental difference between transient and synchronous SL (Crum, 1994) or perhaps to electrical discharges initiated by the tip of the cell disruptor that drives the fluid. The apparatus of Frenzel and Schultes (1934) was designed to avoid this ambiguity but, unfortunately, they abandoned this line of research after their first paper.

10. What is the light-emitting mechanism?

The transduction of sound into light was coined "sonoluminescence" by Harvey (1957). The reason for the use of the ending "luminescence" dates back to Wiedemann (1889), who defined luminescence as cold light, in contrast to hot light, such as fire. Instances of cold light included such long-established discoveries as light from frictional electricity (*Reibungselektrizitätsluminescenz*) and

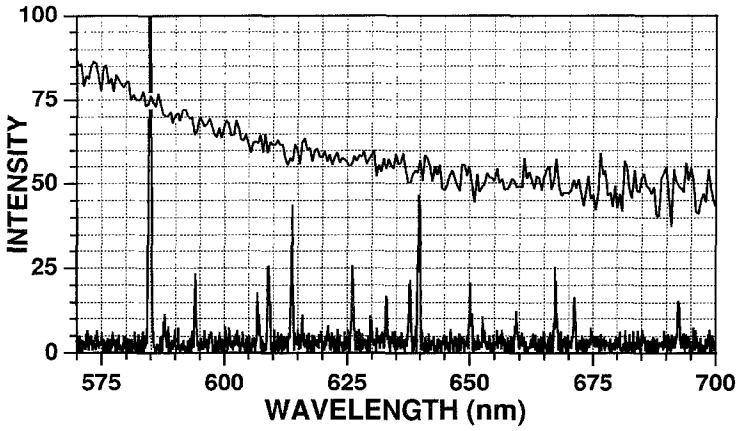

Fig. 62. A comparison of the spectrum of SL from a 3 Torr neon bubble and the spectrum of gas discharge through a 75 Torr neon atmosphere (generated by frictional electricity of mercury against glass (Picard, 1676)). Note that the dramatic peaks which give neon its characteristic orange-red color are absent for SL.

light emitted by fracturing crystals, "triboluminescence". A comparison of the spectra of frictional electricity and SL is shown in Fig. 62. The broadband spectrum is emitted by a neon gas bubble trapped in a sound field according to the procedures of Section 2. The line spectrum is emitted by the friction of mercury against glass in a neon atmosphere at a pressure of 75 mm (Budakian et al., 1996). The broadband nature of what we have been calling SL stands in strong contrast to the very bright spectral lines of the luminescence of frictional electricity. Indeed, the absence of lines in SL strongly suggests that the SL bubble is very hot and/or very stressed so that the comparison with other luminescence phenomena may be misleading. One can wonder if in fact SL is a thermal phenomenon and if its correct name would have been "sonoincandescence".

Explanations of the light-emitting mechanism of SL naturally seek to interpret the featureless spectrum in terms of emission from a hotspot, for example blackbody radiation if the radiation and matter are in near equilibrium (Noltingk and Neppiras, 1950) or *Bremsstrahlung* from accelerating unbound electrons if the light-emitting region is hot enough to be ionized yet sufficiently rarified so as to be transparent to radiation (Wu and Roberts, 1993). Another candidate mechanism, chemiluminescence, originates in molecular dissociation and recombination at a hotspot (Griffing, 1952).

The adiabatic heating which accompanies the collapse (Eqs. (5), (7)) can produce temperatures of about 5000 or 10 000 K (Noltingk and Neppiras, 1950; Löfstedt et al., 1993). Since 1 eV is about 12 000 K and since the spectrum of SL is generally rising at 6 eV (200 nm), it appears that adiabatic heating could lead to some light emission but that it does not focus energy sufficiently to explain the strongly ultraviolet SL spectrum. In Rayleigh's original investigation (1917) of the spherically imploding bubble, he assumed that the gas obeyed an isothermal equation of state, and so he missed his chance to predict SL.

The shock wave model (Jarman, 1960; Löfstedt et al., 1992; Greenspan and Nadim, 1993; Wu and Roberts, 1993, 1994; Barber et al., 1994; Moss et al., 1994) provides an extra stage of energy focusing by assuming that the supersonic inward collapse of the bubble wall launches a shock wave into the bubble's interior. This shock can run through the already compressed gas inside the bubble, increasing its amplitude and speed as it focuses towards the origin. As sketched in Fig. 63, there is now a surface of radius R_s (the radius of the shock front), within the bubble of radius R. As the

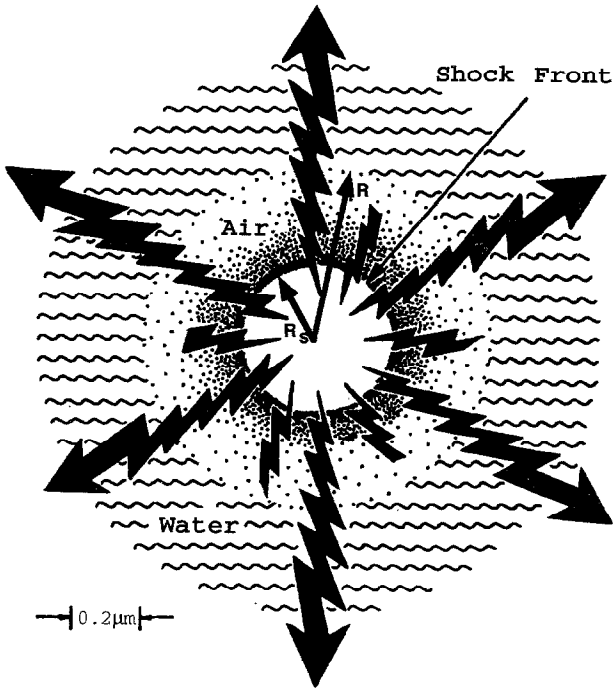

Fig. 63. Sketch of an imploding shock wave model of SL. The shock is launched by the supersonic motion of the bubble wall. The radius of the gas water interface is R and the radius of the shock is R_s. The shock first implodes to a focus and then explodes. This figure depicts the state reached about 100 ps after focusing.

shock moves towards the origin its strength increases until it becomes so strong that there exists a similarity solution to the Euler equations (i.e. the non-dissipative limit) of fluid mechanics. In this case Eq. (1) and (2) must be supplemented with (Landau and Lifshitz, 1987)

$$\frac{\partial s}{\partial t} + \boldsymbol{v} \cdot \nabla s = 0 \tag{44}$$

where s is the entropy per gram, and effects of viscosity in (3) are neglected. In spherical coordinates, these radially symmetric equations are

$$\frac{\partial \rho}{\partial t} + \frac{\partial \rho v}{\partial r} + \frac{2\rho v}{r} = 0, \tag{45}$$

$$\frac{\partial v}{\partial t} + v\frac{\partial v}{\partial r} + \frac{1}{\rho}\frac{\partial P}{\partial r} = 0, \tag{46}$$

$$\left(\frac{\partial}{\partial t} + v\frac{\partial}{\partial r}\right) \log \frac{P}{\rho^{\gamma}} = 0 \tag{47}$$

where v is the radial component of the velocity, and the last relation expresses the conservation of the entropy of a polytropic gas. The similarity solution is obtained by assuming that the shock radius takes the form (Guderley, 1942)

$$R_s = A(-t)^{\alpha} \tag{48}$$

where time is measured from the time of the convergence of the shock, and A is the "launch" condition of the shock, which couples the shock to the bubble motion. A similarity solution is then sought in the variable $\xi = r/R_s(t)$, such that $v = (\alpha r/t)\tilde{v}(\xi)$, $\rho = \rho_1\tilde{\rho}(\xi)$, and $c^2 = (\alpha^2 r^2/t^2)\tilde{c}^2(\xi)$. The solution yields an exponent α of 0.72 in air and 0.69 for noble gases. Since the exponent is less than unity, the Mach number of the shock which goes as $M = \dot{R}_s$ becomes infinitely large as the shock implodes toward the origin. The temperature immediately behind the imploding shock front is given by $T/T_0 \sim M^2$. However, when the shock converges on the origin it explodes from the origin with the same similarity solution. Thus the gas which was compressed just behind the imploding shock front now finds itself in front of the shock front again. As the shock passes through these particles a second time, there is another burst of heating and the maximum temperatures reached by the exploding shock wave now goes roughly as $T/T_0 \sim M^4$ (Barber et al., 1994). (This is an approximation for the purpose of dimensional analysis since, even though it obeys the same scaling laws, the exploding shock is not strong.) The energy focusing ability of the shock front in this model is thus controlled by the extent to which the shock wave is stable upon implosion. Since the imploding shock gets stronger as it approaches the origin, the similarity solution, valid in the limit of high amplitude, always applies eventually. The same form of solution even works for a van der Waals gas (Wu and Roberts, 1994), but is invalidated when ionization effects become important.

Determination of the launch condition, A, connects the imploding shock solution to a particular bubble motion. This condition can be estimated by the (nonrigorous) extention to 3D waves of the concept of characteristics (Landau and Lifshitz, 1987). Consider for example a "characteristic" launched by the bubble wall into its interior when its radius passes through R. The location of this characteristic at time t is $\hat{R}(R, t)$ and its motion is described by

$$\frac{\mathrm{d}}{\mathrm{d}t}\hat{R} \approx -[c_g(R) + |\dot{R}(R)|]\frac{R}{\hat{R}} \tag{49}$$

where the velocity of the characteristic is the speed of sound in the gas plus the actual velocity of the bubble wall, and is adjusted by the amplification factor $1/\hat{R}$, appropriate to a three-dimensional disturbance as it approaches the origin. This characteristic reaches the origin in a time

$$\hat{t}(R) = R/2[c_g(R) + \dot{R}(R)]. \tag{50}$$

The time for the bubble wall itself to collapse from R to 0, for an ideal gas equation of state is

$$\tau(R) = \tfrac{2}{5}R/\dot{R} \tag{51}$$

where for $R < R_m/2$, $\dot{R}$ is given by (14). One possible criterion for shock formation is that there exists an R such that $\hat{t}(R) = \tau(R)$, or

$$\frac{\dot{R}(R_0)}{c_0} \geq 4\left(\frac{R_0}{R}\right)^{3\gamma/2-3} \tag{52}$$

so when $\dot{R}(R_0)/c_0 \sim 1$ this criterion yields $R = R_0/4$. If one restricts R to the range of validity of the ideal gas equation of state, then $R > R_0/8$ and the corresponding expansion ratio is $R_m/R_0 = 7$. The smallest expansion ratio at which SL has been observed is about 8 : 1. Other criteria (such as characteristics crossing) for shock formation are also possible. A computer calculation indicates that the shock appears about 100 ps before the bubble reaches its minimum radius and that the

shock forms at 1/2 the radius of the bubble when the bubble wall is collapsing at 4–5 times the ambient speed of sound (Wu and Roberts, 1993, 1994). In each case the dimensional analysis and the brute force calculation lead to Eq. (21) as being not only the criterion for shock formation but also the criterion for SL. So we will adopt, for the estimate of A, the criterion that the bubble wall is collapsing at the speed of sound when it is passing through its ambient radius. In this case (Barber et al., 1994)

$$R_s = R_0(-t/t_0)^{\alpha}, \quad t_0 = \alpha R_0/c_0 \tag{53}$$

and in terms of the Mach number

$$M = |t_0/t|^{1-\alpha} \tag{54}$$

one can estimate

$$R_s \sim R_0(1/M)^{\alpha/(1-\alpha)}, \quad t_s \sim (\alpha R_0/c_0)(1/M)^{1/(1-\alpha)} \tag{55}$$

where t_s is the time scale for the shock to have a radius smaller than R_s. For $M = 4.3$ and $R_0 = 4.5$ μm, these scaling relations yield $T = 10^5$ K, $R_s = 0.15$ μm and $t_s = 100$ ps. For $M = 24$ these scaling relations yield $R_s = 30$ Å, $t_s = 0.3$ ps and $T = 10^8$ K (which would be hot enough for fusion if it happened in a deuterium bubble! (Barber et al., 1994)). Whether the shock can maintain itself down to such incredibly small radii remains to be seen. It should also be emphasized that, in contrast to the bubble wall, the shock surface has not yet been experimentally detected.

The temperatures reached by the shock heating suggest that the gas in the bubble forms a dense ionized region. The free electrons released by the heating will accelerate and radiate light as they collide with the ions. The Bremsstrahlung so generated has a spectral density per unit wavelength λ, per unit volume per second given by (Glasstone and Lovberg, 1960)

$$\frac{dP}{d\lambda} = \frac{16\pi^2 e^6 n_e n_i}{\sqrt{3k_B T}\, m_e^{3/2} c^2 \lambda^2} \exp(-hc/\lambda k_B T) \tag{56}$$

where e, m_e are the electron charge and mass, n_e, n_i are the density of free electrons and ions, and c is the speed of light. If we assume that the light is emitted during an interval of time t_s from a region with radius R_s and a temperature determined by the Mach number, we find for the light energy radiated per flash (per unit wavelength λ)

$$\frac{dE_\lambda}{d\lambda} = \frac{128\pi^2\alpha}{\sqrt{3}} \frac{Nk_B T}{\lambda} \frac{R_0}{\lambda} 145 q^2 \beta^2 n a_B^3 \left(\frac{e^2}{2a_B k_B T}\right)^3 \times M^2 (1/M)^{(3\alpha+1)/(1-\alpha)} \exp(-hc/\lambda k_B T) \tag{57}$$

where N is the total number of atoms in the bubble and n is their density in the region of the shock front, β is the ratio of the thermal electron velocity to the speed of light, a_B is the Bohr radius, $q = n_e/n$ is the degree of ionization, and for the ideal gas the maximal compression is $n = 145 n_0$. For q a good estimate is obtained from Saha's equation of state (Fermi, 1936)

$$q^2/(1-q) \approx 10^{-7} T^{3/2} \exp(-\chi/k_B T) \tag{58}$$

where χ is the ionization potential and the prefactor T is given in kelvin. The measured light ($\lambda > 200$ nm) is dominated by temperatures above 10^5 K. So if one substitutes the corresponding $M = 4$ into (57) and notes that the degree of ioniztion is almost unity (so that $n_e = n_i = n$) one finds that the total radiated energy per flash is about 10^7 eV in rather good agreement with experiment. In a more precise analysis, a van der Waals equation of state would be used for this calculation. Beyond that, one would employ equations of state that are themselves corrected for the degree of ionization. Finally, corrections to the Bremsstrahlung formula to account for the posibility that SL originates from a dense cold plasma should be considered.

Since the SL light emission occurs as a (mathematical) singularity is forming, any transport process which a theorist chooses to incorporate in this model can affect the result (Moss et al., 1994; Kondic et al., 1995; Vuong and Szeri, 1996). A closely related model ascribes the radiation to changes in molecular dipole moments that are induced by collisons (Frommhold and Atchley, 1994). These effects, however, would be suppressed in pure noble gas bubbles.

The launch of a shock wave by the Rayleigh-Plesset bubble dynamics with the subsequent Bremsstrahlung radiation from the hot ionized contents is the most complete candidate model of SL. This model, however, is far from satisfactory. It requires a number of key physical inputs such as the acoustic drive level and ambient radius (P_a and R_0) at which bubbles give SL and additional physical inputs are required in order to determine the minimum radius attained by the shock. Furthermore, it does not address compelling yet simply stated mysteries, such as why pure diatomic gases are bad sources of SL.

Another insight into the light-emitting mechanism is that it is relatively unaffected by a strong, 20 T, magnetic field (Young et al., 1996). Even though the cyclotron radius of 100 000 K electrons is 0.5 μm, which is close to the minimum bubble radius, and the cyclotron period is 1 ps, which is shorter than the current bound on the flashwidth, in first approximation SL appears to be unaffected.

According to (56), Planck's constant determines the high energy cutoff in the Bremsstrahlung spectrum. Since the spectrum beyond the cutoff of water has not yet been observed, the validity of this term has not been checked. Thus the shock wave-Bremsstrahlung model lies entirely within the range of classical mechanics and there still remains the exciting issue of whether Planck's constant will play a role in a phenomenon initiated by classical acoustics! In this direction Schwinger (1993) proposed that the change in electromagnetic zero point energy brought about as water filled in the gaseous cavity would show up as radiation. The "spectrum" of zero point energy in a volume V near wavenumber k is

$$\mathrm{d}E_k = \tfrac{1}{2}\hbar c k V \,\mathrm{d}^3 k. \tag{59}$$

Due to a jump in the index of refraction n at the bubble interface, the collapsing wall sweeps out a changing zero point motion which then becomes observable. The rate of change of the zero point energy of water plus bubble is then

$$\frac{\mathrm{d}}{\mathrm{d}t}\frac{\mathrm{d}\Delta E_\lambda}{\mathrm{d}\lambda} = (2\pi)^5 \hbar c \frac{\Delta n}{\lambda^5}\frac{\mathrm{d}V}{\mathrm{d}t}. \tag{60}$$

Although the power law spectrum has similarities to SL, this source of energy transduction is a maximum when the rate of change of volume is a maximum which is near the maximum radius. In contrast, the rate of change of the surface is a maximum at the moment of light emission, but

attempts to interpret SL in terms of Unruh radiation from the surface (Eberlein, 1996; Knight, 1996) yield powers that are too small by many orders of magnitude.

Another light emitting mechanism that has been proposed is an electronic discharge from charge separation inside a plasma (Lepoint et al., 1996). This picture is reminiscent of "ball lightning" (Kapitza, 1956). Also, SL has been connected to triboelectric phenomena via a postulated cracking of a solid gas shell that forms on the bubble wall (Hickling, 1994) and by the "cracking" of the water by a supersonic jet launched by the collapsing bubble (Prosperetti, 1996). The value of these various models will be judged based upon their ability to make falsifiable predictions.

11. How spherical is the collapse?

One of the defining characteristics of electromagnetism is that spherically symmetric accelerations of charge distributions do not radiate (Ehrenfest, 1910; Stratton, 1941). Yet among picosecond light sources sonoluminescence is unique in that the flash intensities are uniform over a spherical shell and furthermore this light originates from a region that is smaller than its wavelength. Based upon these observations it is clear that a probe of possible angular correlations in SL would help to characterize the properties of this light source and possibly shed light on the light-emitting mechanism. Although we have observed dipole components that reach 10% of the total emitted intensity (Weninger et al., 1996), they can be interpreted as being due to the refraction of light by a nonspherical bubble wall that separates the hot gas near the center of the bubble from the surrounding host liquid. According to this interpretation, angular correlations in SL provide a diagnostic for the sphericity of the bubble collapse (and therefore they do not reflect the light-emitting mechanism). Since a more spherical collapse is more violent, this diagnostic should prove to be useful in attempts to reach higher levels of energy concentration with sonoluminescence.

These correlations were measured with multiple photodetectors as a function of their observation angle (Weninger et al., 1996). The angular dependence in the intensity of SL is characterized by a non-zero value of the correlation,

$$\Delta Q_{AB} = \frac{1}{\bar{Q}_A \bar{Q}_B} \langle [Q_A(i) - \bar{Q}_A][Q_B(i) - \bar{Q}_B] \rangle_i \tag{61}$$

as a function of the angle θ_{AB} formed by the detectors "A" and "B" and the bubble which is reckoned to sit at the vertex. In Eq. (61), $Q_A(i)$ is the total charge recorded in detector A on the ith flash, $\bar{Q}_A$ is the running average of $Q_A(i)$ and $\langle\ \rangle_i$ denotes an average over i. In addition to tubes A and B there is a trigger tube which monitors the SL so as to gate a digital oscilloscope which then acquires the tube outputs. From the data generated by 1000 flashes, the average and the correlation (61) are calculated. Twenty such data sets generate a "result" and the average and standard deviation of 3 results generate the plotted point and "error" bar at each angle. As experimental configurations were varied, the signal recorded in each phototube ranged from 5–8 photoelectrons per flash of SL.

The solid line in Fig. 64 displays the angle dependent correlation that is observed in most runs. It can be attributed to a dipole component in the detected photon field. If $\bar{\Omega}_A$ is the fraction of solid angle subtended by detector A, and N_I and N_D are the numbers of photons arriving isotropically and as a dipole, then the total number of photons to strike the detector is

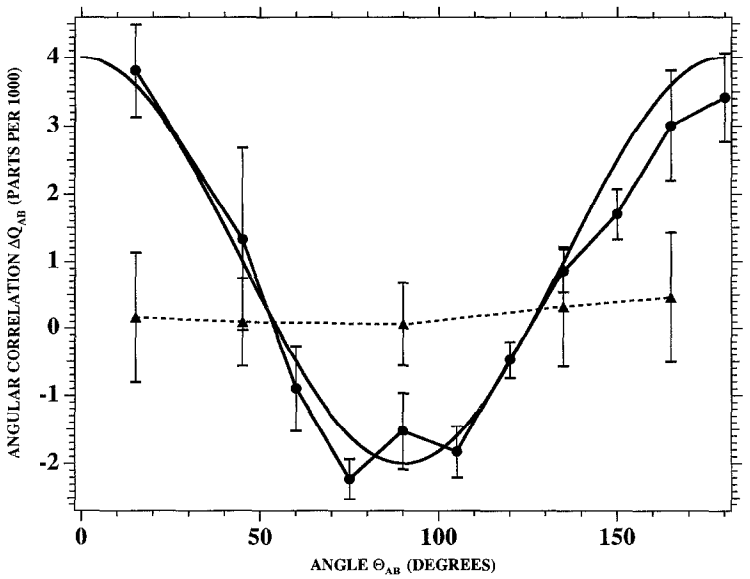

Fig. 64. Correlation of light intensity between two phototubes subtending an angle θ_{AB} with respect to a sonoluminescing bubble. The solid line corresponds to an SL bubble whose flash to flash intensity has a large variation. The flash to flash fluctuations for the dotted line are much less and are furthermore consistent with Poisson statistics. Note the appearance of a negative correlation at 90°. The maximum dipole observed is about 10 parts per thousand. If the dipole is due to refraction of light at the gas-fluid interface of the bubble then the ellipticity of the bubble in the state with large fluctuations is about 20%. The sine wave fit is $0.001(1+3\cos\theta)$.

$$N_A(i) = \bar{\Omega}(N_I + 3N_D \cos^2\theta_{iA}) \tag{62}$$

(and similarly for B), where θ_{iA} is the angle between the direction of the dipole on flash i and the detector A. If one assumes that over time there is no preferred direction, then a physical dipole of strength N_D leads to the correlation

$$\Delta N_{AB} = \frac{\langle [N_A(i) - \bar{N}_A][N_B(i) - \bar{N}_B]\rangle_i}{\bar{N}_A \bar{N}_B}$$

which upon substitution of (62) yields

$$\Delta N_{AB} = \frac{N_D^2}{(N_I + N_D)^2}\left(\tfrac{1}{5} + \tfrac{3}{5}\cos 2\theta_{AB}\right). \tag{63}$$

So according to the sine wave fit to the data in Fig. 64, this observed field has a dipolar component, N_D/N_I, of 7%.

In order to determine whether the dipole is due to the mechanism whereby the stress of implosion is converted into light, we measured the correlation (61) as a function of the time delay Δt between acquisitions in tubes A and B (Weninger et al., 1996). In the case that the dipole is due to the light-emitting mechanism each flash would be independent of the previous flash so that the correlation should fall abruptly to zero for $\Delta t \neq 0$. As shown in Fig. 65, however, the dipole correlation $\Delta Q_{AB}(\Delta t)$ has a long memory, about equal to the free decay time of the sound field.

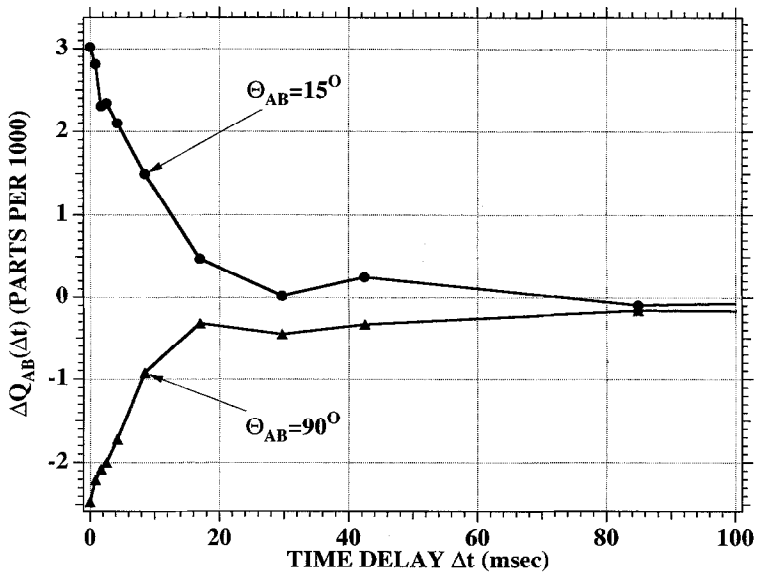

Fig. 65. The correlation of an SL flash in tube A with flashes in tube B at a later time. The time delay $\Delta t = nT_a$, where n is an integer and T_a is the acoustic period. The long-term memory of the dipolar component is comparable to the lifetime of the driving sound field. Typical quality factors for these sound fields range from 500–1500.

This long time decay of the angle-dependent correlation indicates that the dipole component is due to some aspect of the hydrodynamic motion. Such motions rearrange themselves on the same time scale for which the sound field changes. The various possibilities include (1) jitter in the location of the bubble, (2) bending of the emitted light by the sound field in the bulk of the fluid, and (3) refraction of the SL rays by the surface of a non-spherical bubble. Jitter gives the wrong sign of correlation and the effect of ray bending is too small since it goes as the Mach number of the sound field in the water squared.

The simplest explanation of the measured angular correlation is in terms of refraction, by the nonspherical bubble wall, of light that is emitted uniformly from a point source within the bubble's interior. Fig. 66 shows how light from a point source would be refracted by passage through an elliptical boundary in the ray optics limit. For an interface where the index of refraction jumps from 1.0 (on the gas side of the bubble's surface) to 1.35 (in water), a 7% dipolar component would require a 20% ellipticity. (We define ellipticity as $a/b - 1$ where a and b are the major and minor axis, respectively.) For demonstration purposes Fig. 66 was constructed for a jump in the index of refraction from 1.0 to 2.0 and a ratio of major axis to minor axis of 2.

Another insight into the origin of these correlations is provided by the observation that in some runs the dipole component vanishes, as shown by the dashed line in Fig. 64. According to Fig. 67 these states are in one to one correspondence with narrow pulse height distributions. The time record and histogram of SL flash intensities indicates that the state with a 7% dipolar component (and ellipticity of 20%) has over an order of magnitude more spread in flash intensities. (The spread is defined as the maximum divided by the width at half maximum.) For the state with a narrow pulse height distribution the dipole component (as determined by a least squares fit) is 1%, which corresponds to

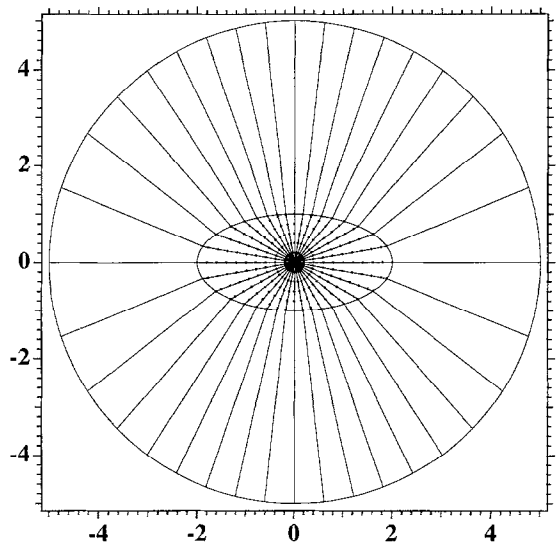

Fig. 66. Refraction of light from a point source by a surrounding elliptical interface. For purpose of demonstration this figure was generated with a major axis that is twice the minor axis. Such a surface introduces a dipole component into the far field.

an estimated upper bound on ellipticity of about 3%. Using three detector tubes we were also able to verify that the angle-dependent and angle-independent states occurred in the vertical and horizontal planes simultaneously. That is, when the longitude showed a large dipole so did the latitude, and similarly for the case of no dipole.

Control of the key parameters which determine whether the collapse is elliptical has been elusive as the system falls into and out of this state. Various candidate parameters are imperfections in the sound field such as coupling to nearby modes of the resonator, thermal drift, scattered sound biting back on the bubble, or dust particles in the vicinity of the bubble. Each of these hydrodynamic motions is coupled to the sound field and will tend to wander on the time scale determined by its bandwidth. In this way the direction of the measured dipole will change in space on the time scale shown in Fig. 65. Remarkably, we have found that the jitter (50–100 ps) in the time between flashes is the same for the two states shown in Figs. 64 and 67 (Weninger et al., 1996). So, these particular effects do not appear to explain the chaos observed in other experiments (Holt et al., 1994).

By inserting colored glass filters between the PMT and the bubble, the dependence of the angular correlations on color can be investigated (Weninger et al., 1996). Fig. 68 shows the angular correlation for "red" ($\lambda > 500$ nm) and "blue" ($260 < \lambda < 380$ nm) light for the same bubble state. The fact that the red correlation is suppressed indicates that these longer wavelengths diffract out of the bubble's interior on their way to the detector. This implies that the radius of the bubble at the moment of light emission is about equal to the wavelength of red light, consistent with light-scattering measurements (Barber and Putterman, 1992).

According to Hanbury-Brown and Twiss (HBT) (Hanbury-Brown, 1974), filtered light from an incoherent uniform emitter can display angular correlations in the intensity. This effect has been used to measure the radius of stars. If the dipole component in these broadband measurements is indeed due to the asphericity of the collapse, then this source of correlation will have to be monitored or

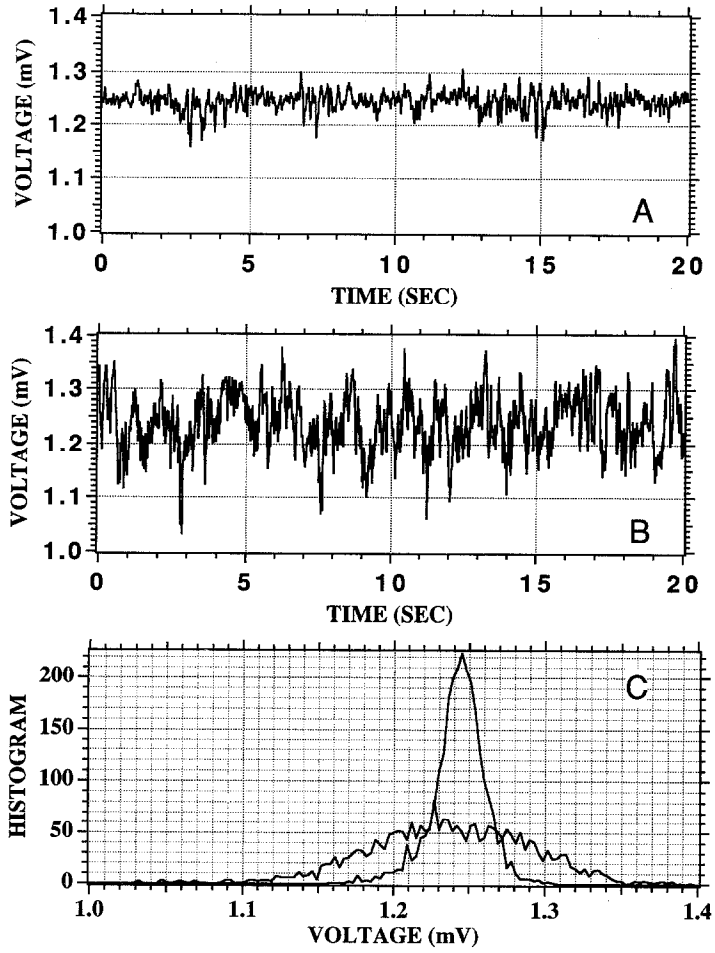

Fig. 67. Fluctuations in SL intensity for states with large and small dipolar components. Time records are displayed in (A), (B) and the pulse height distributions are compared in (C). The sound field has a frequency of 26.4 kHz, and the detectors each record an average of 5 photoelectrons per flash. The time constant for binning is 10 ms.

eliminated in an attempt to apply HBT to SL (Trentalange and Pandey, 1996).

The observed dipole in the light emission provides a probe of the degree of nonsphericity of the collapse. Ellipticity is the leading order, quadrupolar, form of a convolution instability. Such instabilities have also been studied with regard to bubble (Plesset and Mitchell, 1956; Prosperetti, 1977; Löfstedt et al., 1995; Brenner et al., 1995) and shock wave motion (Wu and Roberts, 1996a, 1996b) and inertial confinement fusion (Budil et al., 1996). For bubble motion the convolutions are expanded in terms of spherical harmonics so that

$$R(t) = \bar{R}(t) + \sum_{n=2}^{\infty} a_l(t) Y_l(\theta, \phi). \tag{64}$$

Requiring that pressure and velocity be continuous at the surface of the bubble yields to linear order in the amplitudes of convolution $a(t)$ (Prosperetti, 1977)

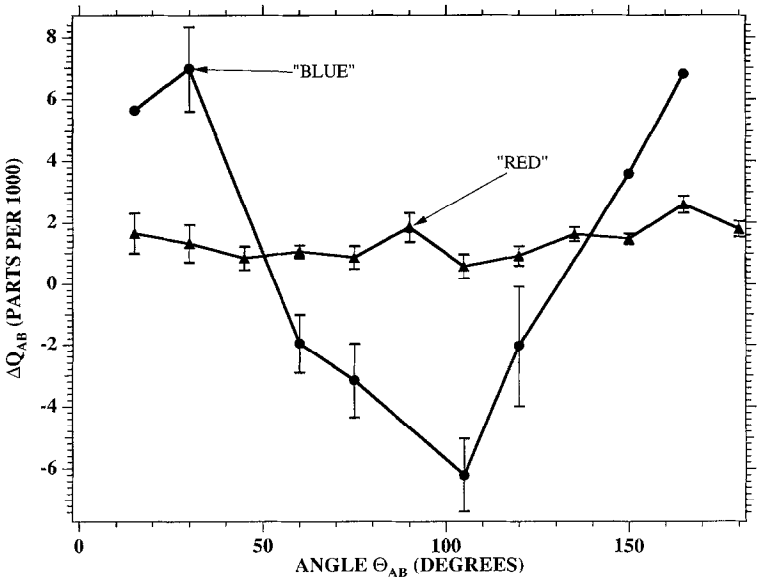

Fig. 68. Angular correlation for the long and short wavelength parts of the SL spectrum. According to the model presented in Fig. 66 the absence of correlation at long wavelength is attributed to the dominance of diffraction over refraction.

$$R\ddot{a}_l + \left(3\dot{R} + 2\frac{\nu(l+2)(2l+1)}{R}\right)\dot{a}_l - \left((l-1)\ddot{R} - \frac{2\nu(l-1)(l+2)}{R^2}\dot{R} - \frac{(l^2-1)(l+2)\sigma}{\rho R^2}\right)a_l = 0 \tag{65}$$

where the bar has been dropped from R. This equation has the form of a Hill equation being a second order linear differential equation with coefficients that are periodic functions of time. There are three cases of interest. First, on the short time scale, one can ask if this equation develops an instability which leads to the rapid growth of a convolution during one cycle of the motion. This is the issue of whether the bubble suffers from Rayleigh-Taylor (RT) instability (Rayleigh, 1883; Taylor, 1950). Next one can ask if the convolution builds up from cycle to cycle. This question which is in the spirit of the Matthieu equation (Landau and Lifshitz, 1976) for a parametrically driven swing can be applied to the bouncing and SL bubbles. For the SL bubble a theory which connects the hydrodynamics on both sides of the collapse does not exist so Eq. (65) cannot be applied to this case. We now consider the RT instability within a cycle for SL and bouncing bubbles and the Matthieu type instability for the non-SL bubble.

First, we neglect the (stabilizing) effects of viscosity. For the SL bubble the cycle is divided into the expansion the collapse and the time during which the bubble sits dead in the water. During the expansion of the bubble to R_m the growth is approximately linear and $a(t)$ decreases as $1/R^2$ from its initial value. During the collapse Eq. (14) applies so that (65) yields $a \sim (R_m/R)^{1/4}$ (Plesset and Mitchell, 1956). Up until the point where deviations from the ideal gas law come into play the enhancement of the convolutions is at most a factor of 3. That the motion is in fact RT stable can be appreciated by writing (65) in Hamiltonian form (Löfstedt et al., 1995),

$$H = \frac{p_l^2}{2\rho R^3} - \frac{\rho(l-1)}{2} R^2 \ddot{R} a_l^2 + \frac{(l^2-1)(l+2)}{2} \sigma a_l^2 \tag{66}$$

where, as mentioned, viscosity has been neglected. Since $\ddot{R}$ is negative during the collapse (see Fig. 12), the motion in the potential well of the Hamiltonian is stable, and the (factor of 3) magnification of a is due to the scaling of the effective mass and the potential through R in the spherical geometry. Following the collapse, the bubble is motionless at R_0 for half the acoustic cycle. During this part of the cycle convolutions decay due to the viscosity which we now include (Prosperetti, 1977)

$$a_l(t) = a_{l0} \cos(\omega_\sigma t + \delta_0) e^{-\alpha t} \tag{67}$$

where

$$\omega_\sigma^2 = \frac{(l-1)(l+1)(l+2)\sigma}{\rho R^3}, \quad \alpha = \frac{(l+2)(2l+1)\nu}{R^2}. \tag{68}$$

In particular, the time constant for a quadrupolar perturbation to decay for a bubble motionless at $R_0 = 4$ μm is less than 1 μs which is very short when compared to this 15 μs portion of the acoustic cycle. So we conclude that during any given cycle, i.e. from flash to flash, harmonic convolutions do not build up (Löfstedt et al., 1995). The upper threshold of SL is due either to some other hydrodynamic instability or to an event occurring at the moment of collapse which is not describable by the hydrodynamics.[2]

The decay rate $\alpha_0 = \nu_0/R_0^2$ (where ν_0 is the ambient kinematic viscosity of the gas) for acoustic energy stored inside the bubble is also on the order of a microsecond. When other sources of damping such as acoustic radiation and bulk viscosity are included this time becomes even shorter. Therefore, there no usable energy is stored inside the bubble during a cycle, in contrast with a recent suggestion (Brenner, Hilgenfeldt, et al., 1996).

Fig. 69 shows the standard deviation in light scattering from a collapsing bubble of 1% xenon in oxygen. Note that for a given radius (a given average signal) the standard deviation after the collapse is larger than before the collapse. This can be interpreted as due to the generation of a convolution in the bubble as a result of the crash. Depending upon the orientation of the convolution relative to the laser, systematic variations in the scatter can occur which would not be present for a spherical bubble. Since a macroscopic theory that connects the bubble motion before and after the collapse has not yet been developed, this ringing convolution cannot be derived. Nevertheless this bubble is stable and so this convolution dies out before the next cycle, consistent with the above analysis. These collapse induced shape oscillations are not observed in all bubbles (e.g. air). Another type of asphericity that occurs in a collapsing bubble is the formation of a jet (Kornfeld and Suvorov, 1944; Kling and Hammit, 1972; Lauterborn and Bolle, 1975; Crum, 1979). The possible role of jets in SL has been proposed by Longuet-Higgins (1996) and Prosperetti (1996).

[2] The shape instabilities derived by Brenner et al. (1995) and Hilgenfeldt et al. (1996) resulted from the use of a coefficient of damping which is much smaller than that given by Eqs. (65), (68). Their unphysical damping term is due to the application of an asymptotic expansion beyond its range of validity (Roberts and Putterman, 1996). It remains to be seen whether SL is affected by non-RT sources of shape instability such as jets, bubble pinch-off, anomalous diffusion, or resonator imperfections. We regard Eq. (65) as being consistent with Lamb (1945), Prosperetti (1977), and Prosperetti and Seminara (1978), for subsonic bubble motion.

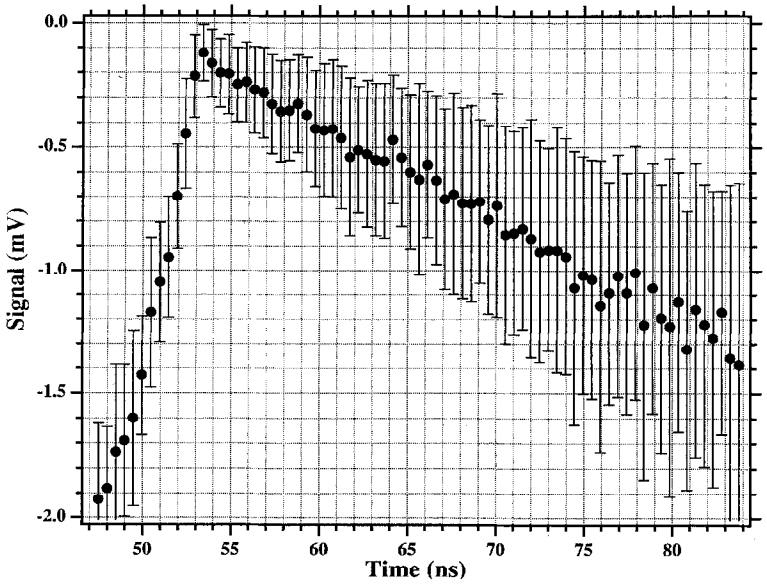

Fig. 69. Standard deviation in the intensity of light scattered from a bubble near the moment of light emission. The average value determines the radius, and the bar determines the standard deviation in a given 500 ps bin. (Note that the standard deviation of the mean is down by about a factor of 8 from the plotted values.) The larger standard deviation after collapse can be interpreted as due to nonspherical bubble oscillations whose orientation relative to the laser varies from shot to shot. For some gases the standard deviation does not increase as a result of the collapse. These data were taken for 1% xenon in oxygen at 150 mm.

12. How controllable are experiments on sonoluminescence?

There are two cultures of sonoluminescence. One culture, which includes the theorists, is intrigued by the picosecond timescales, the energetic spectrum, the upper and lower thresholds, and the effect of doping with a noble gas. There is, however, an experimental culture that expends substantial effort on the critical yet apparently disjoint issue of controlling this phenomenon. In this direction it can be said that we do not yet know the complete set of experimental parameters that must be controlled so as to render experiments on SL reproducible from lab to lab.

First on this list of challenges is the acoustic resonator. Our best resonator to date has been custom made by GM from GE quartz. We have worked with four such spheres each of which has a sphericity accurate to one percent. Three of these spheres have produced the most stable reproducible SL that we have measured. The fourth looks identical in every way to the other three yet it produces a lousy acoustic resonance and even for air in water the SL signal is highly unstable. Also the tendency of an SL bubble to walk off-center as the drive level is increased varies from resonator to resonator. Perhaps the appearance and disappearance of the dipole component is also connected with the input acoustics. Clearly, slight variations in the acoustical properties of the resonator can be critical. Substantial efforts have been expended on "resonator technology"; the next efforts will include metallic resonators with windows.

Although water is the friendliest fluid for SL it presents unique difficulties. When pure 19 MΩ cm water from the still comes into contact with air its resistance drops before your eyes as it dissolves

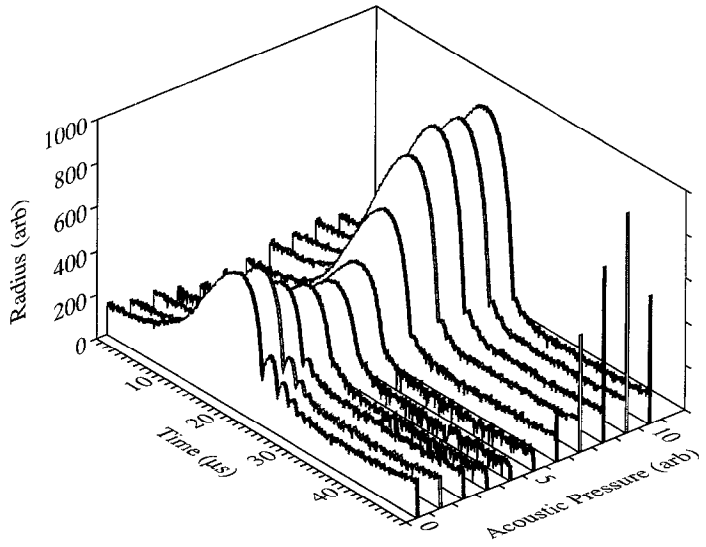

Fig. 70. Waterfall plot of a 150 mm, 1% xenon in nitrogen bubble in water with photoflow solution dissolved into the water at a concentration of 1/500. The photoflow goes to the bubble interface and changes the surface tension so that the bubble dynamics is affected. In particular the smaller bubbles reach a higher expansion ratio.

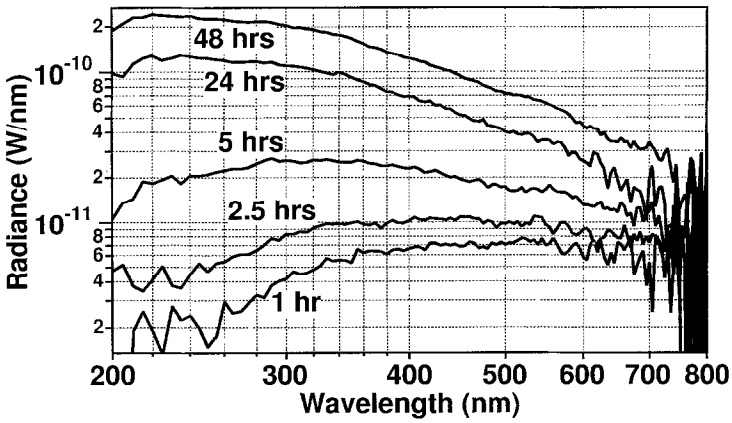

Fig. 71. Spectrum of a deuterium bubble in heavy water as a function of time from preparation of the 3 mm solution. The drift is due to an air leak either from the outside or outgassing from the RTV seals on the cylindrical resonator.

grime from the air. Within a few minutes the resistance is down to 5 MΩ cm and the effective damping and surface tension have been likewise affected. An example of how surface tension can change the bubble dynamics is shown in Fig. 70, which was taken for a 1% xenon in nitrogen bubble at 150 mm with commercial photoflow dissolved into the water at a concentration of 1/5000. The difference with Fig. 33 (no photoflow) is apparent. It would be interesting to carry out SL in a clean environment so as to achieve the lowest viscosity and highest surface tension, perhaps reproducibly.

Small gas leaks have a dramatic effect on the properties of SL. Shown in Fig. 71 is the time dependence of the spectrum of what we prepared to be a hydrogen bubble in heavy water. We do not know whether the leak is from the outside or whether it is due to outgassing RTV seals. This drift

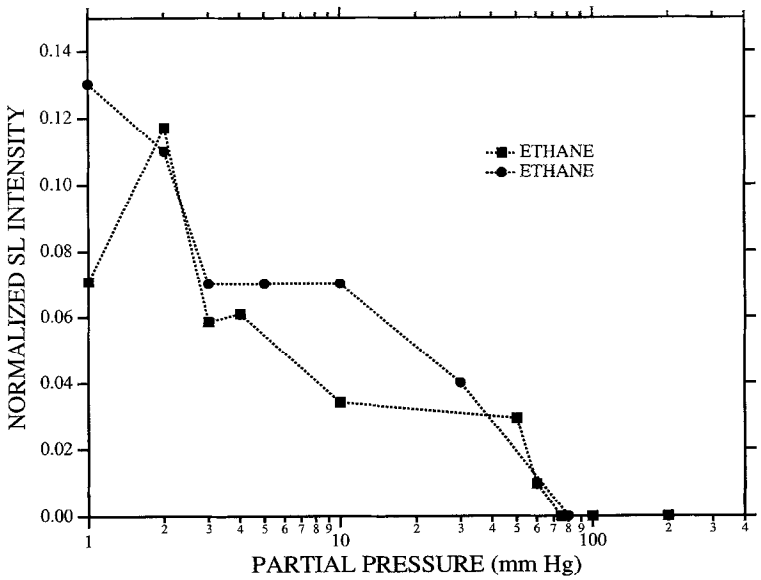

Fig. 72. Intensity of light emission from a 2 mm bubble of ethane in water. Two independent runs are shown.

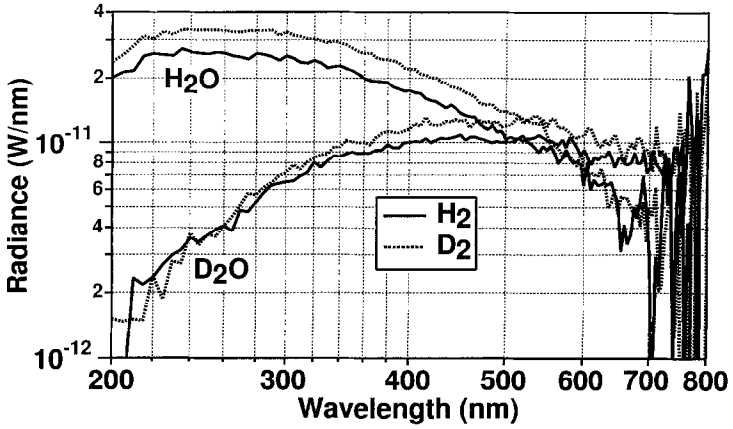

Fig. 73. Spectrum of 3 mm solutions of hydrogen and deuterium in light and heavy water. These are jittery bubbles. Whether these spectra are due to tiny levels of impurity remains to be seen. In any event the spectra in heavy water fit well to a black body spectrum at 6000 K.

is eliminated by rubber O rings. We are even ready to doubt whether *pure* diatomic gases give any light. It is possible that, as higher levels of purity are achieved, these bubbles will behave worse and worse. Fig. 72 shows the typical run to run variations in behavior that can be observed, in this case for a 2 mm ethane bubble in water.

Fig. 73 shows the spectrum of hydrogen and deuterium bubbles in light and heavy water (Hiller and Putterman, 1995). The difference can reasonably be attributed to a dramatic isotope effect due to the heavy water except that, as shown in Fig. 74, different batches of heavy water yield different spectra with xenon bubbles. Tiny impurities in the heavy water could be affecting the results.

Before all confidence is annihilated we should say that the experiments on noble gas doping have

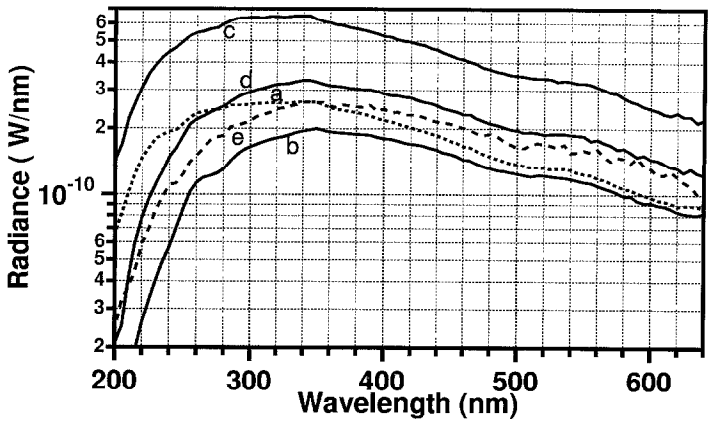

Fig. 74. Spectra of SL from xenon bubbles in light and heavy water prepared at a partial pressure of 3 mm: curves (a) and (b) are for light water and the first batch of heavy water in a spherical resonator, curves (c) and (d) are for other batches of heavy water in a cylindrical resonator and curve (e) is for water with 2.5 ppm 1-butanol, multiplied by 7.3 to align it with pure water at 340 nm.

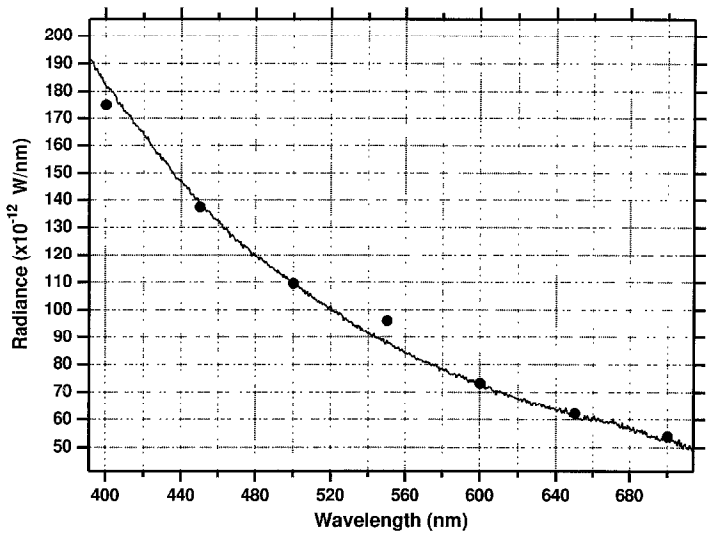

Fig. 75. High resolution spectrum of a 1% xenon in oxygen bubble (at 150 mm partial pressure) obtained via two different calibrations of the radiance. The points are determined by a calibration of the apparatus with a NIST traceable QTH lamp. The continuous line is obtained when the black body curve which provides the best fit to the QTH calibration is used to calibrate the apparatus. The expectation that the SL spectrum should be featureless suggests that the QTH calibration at 550 nm is incorrect.

been repeated from the bottom up by four different researchers, B.P. Barber, D. Chow, R. Hiller, K. Weninger on four different apparatuses with various gas mixtures (Hiller et al., 1994; Chow et al., 1996). Furthermore, some aspects of SL are so remarkably repetitive and reliable as to make SL useful in calibrating instruments! Matching bubble dynamics to hydrodynamics provides P_a and therefore a means of calibrating a hydrophone such as the one used to acquire the data in Fig. 1. The response of a PMT to SL can be used to calibrate after ringing in a picosecond light source (Section 9), and the lack of structure in the spectrum of SL can be used to check the calibration of

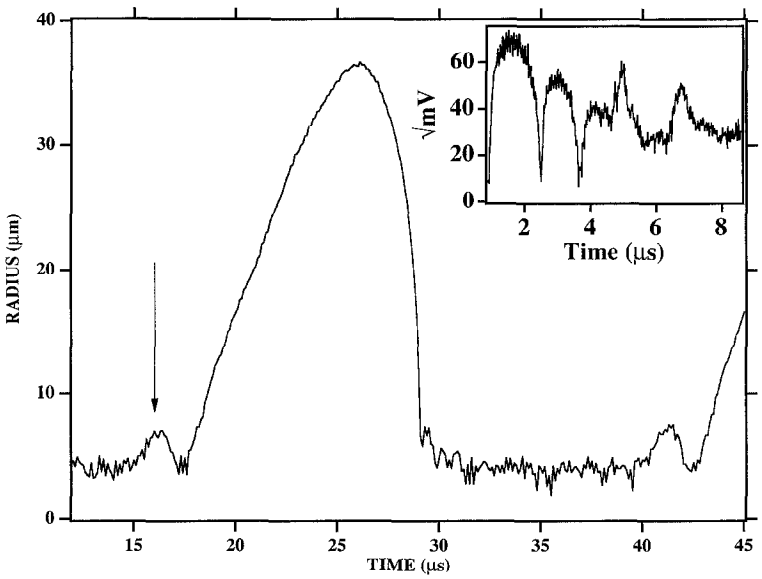

Fig. 76. Radius versus time curve at high drive level showing a glitch in $R(t)$ just as the bubble begins to expand. These data were taken for a 150 mm, 1% xenon in nitrogen bubble. The inset shows that glitches can also appear during afterbounces to SL (Chowet et al., 1996). In contrast with the complete $R(t)$ curve, the inset is not averaged.

light sources as shown in Fig. 75. In Fig. 75 the dots are the spectrum of SL as determined from a QTH lamp with a NIST traceable calibration and the continuous line is the measured SL spectrum as calibrated by the black-body curve that provides the best fit to the QTH calibration. Based upon the insight that the SL spectrum is featureless (on the scale of say 50 nm) one concludes that the light source was incorrectly calibrated at 550 nm.

Returning to the experimental difficulties we finally note that at high drive levels the light scattering experiments observe on occasion a glitch in the radius of the expanding bubble (see Fig. 76). Whether this is an insight into the key issues revolving around the mass flow mechanism, or thresholds for SL, remains to be seen.

Pending the ascendancy of a falsifiable theory, the next set of SL discoveries might instead be driven by engineering improvements that address the issues broached in this section.

Acknowledgments

We are indebted to Tom Erber and Paul H. Roberts for many valuable discussions. This research was supported by the National Science Foundation Division of Atomic, Molecular, Optical and Plasma Physics (experiment) and by the US Department of Energy, Division of Engineering and Geophysics (theory); femtosecond laser measurements were performed with equipment purchased with funds from a non-renewable grant (expired 1994) from the US DOE Division of Advanced Energy Projects. R.A. Hiller is supported in part by funds from the Schwinger post-doctoral fellowship account; R. Löfstedt's work at the ITP was supported by NSF grant 94-07194.

References

Apfel, R., 1986, IEEE-UFFC 33, 139.
D'Arrigo, J.S., S.-Y. Ho, and R.H. Simon, 1993, Investigative Radiology 28, 218.
Asaki, T.J., P.L. Marston, and E.H. Trinh, 1993, J. Acoust. Soc. Am. 93, 706.
Barber, B.P., 1992, Ph.D. Thesis (University of California, Los Angeles).
Barber, B.P., 1994, J. Acoust. Soc. Am. 96, S3252.
Barber, B.P., R.A. Hiller, K. Arisaka, H. Fetterman, and S. Putterman, 1992, J. Acoust Soc. Am. 91, 3061.
Barber, B., R. Löfstedt, and S. Putterman, 1991, J. Acoust. Soc. Am. 89, S1885.
Barber, B.P. and S.J. Putterman, 1991, Nature 352, 318.
Barber, B.P. and S.J. Putterman, 1992, Phys. Rev. Lett. 69, 3839.
Barber, B.P., K. Weninger, R. Löfstedt, and S. Putterman, 1995, Phys. Rev. Lett. 74, 5276.
Barber, B.P., K. Weninger, and S.J. Putterman, 1997, Trans. Roy. Soc. (in press).
Barber, B.P., C.C. Wu, R. Löfstedt, P.H. Roberts, and S.J. Putterman, 1994, Phys. Rev. Lett.72, 1380.
Battino, R., M. Banzhof, M. Bogan, and E. Wilhelm, 1972, Anal. Chem. 54, 806.
Battino, R., T.R. Rettich, and T. Tominaga, 1984, J. Phys. Chem. Ref. Data 13, 563.
Birks, J.B., 1964, Theory and Practice of Scintillation Counting (Pergamon, New York), p. 572.
Bjerknes, V.F.J., 1906, Fields of Force (Columbia, New York).
Brenner, M.P., D. Lohse, and T.F. Dupont, 1995, Phys. Rev. Lett. 75, 954.
Brenner, M.P., D. Lohse, D. Oxtoby, and T.F. Dupont, 1996, Phys. Rev. Lett. 76, 1158.
Brenner, M.P., S. Hilgenfeldt, D. Lohse, and R.R. Rosales, 1996, Phys. Rev. Lett. 77, 3467.
Budakian, R.O., R.A. Hiller, K.R. Weninger, and S.J. Putterman, 1996, unpublished.
Budil, K.S., B.A. Remington, T.A. Peyser, K.O. Mikaelian, P.L. Miller, N.C. Woolsey, W.M. Wood-Vasey, and A.M. Rubenchik, 1996, Phys. Rev. Lett. 76, 4536.
Chow, D., K. Weninger, and S. Putterman, 1996, unpublished.
Church, C., 1988, J. Acoust. Soc. Am. 83, 210.
Cross, M.C. and P.C. Hohenberg, 1993, Rev. Mod. Phys. 65, 851.
Crum, L.A., 1979, J. Phys. (Paris) 40, 285.
Crum, L.A., 1994, J. Acoust. Soc. Am. 95, 559.
Crum, L.A. and S. Cordry, 1994, in Bubble Dynamics and Interface Phenomena, edited by J.Blake et al. (Kluwer, Dordrecht).
Dave, J.V., 1969, IBM J. Res. Dev. 13, 302.
Delgadino, G.A. and F.J. Bonetto, 1996, preprint.
Dodd, R.K., J.C. Eilbeck, J.D. Gibbon, and H.C. Morris, 1982, Solitons and Nonlinear Wave Equations (Academic, New York).
Eberlein, C., 1996, Phys. Rev. Lett. 76, 3842.
Ehrenfest, P., 1910, Phys. Z. 11, 708.
Eller, A. and H.G. Flynn, 1965, J. Acoust. Soc. Am. 37, 493.
Epstein, P.S. and M.S. Plesset, 1950, J. Chem. Phys. 18, 1505.
Feinstein, S.B., 1989, Echocardiography 6, 27.
Fermi, E., 1936, Thermodynamics (Dover, New York).
Fogg, P.G.T. and W. Gerand, 1991, Solubility of Gases in Liquids (Wiley, New York).
Frenzel, H. and H. Schultes, 1934, Z. phys. Chem. B27, 421.
Frommhold, L. and A.A. Atchley, 1994, Phys. Rev. Lett. 73, 2883.
Fyrillas, M.M. and A.J. Szeri, 1994, J. Fluid Mech. 277, 381.
Gaitan, D.F., A.A. Atchley, S.D. Lewis, J.T. Carlson, X.K. Maruyama, M. Moran, and D. Schweider, 1996, Phys. Rev. E 54, 525.
Gaitan, D.F., 1990, Ph.D. Thesis (University of Mississippi).
Gaitan, D.F., L.A. Crum, C.C. Church, and R.A. Roy, 1992, J. Acoust. Soc. Am. 91, 3166.
Glasstone, S. and U. Lovberg, 1960, Controlled Thermonuclear Fusion (Princeton University, Princeton).
Gould, R.K., 1973, J. Acoust. Soc. Am. 56, 1740.
Greenspan, H.P. and A. Nadim, 1993, Phys. Fluids A 5, 1065.
Griffing, V., 1952, J. Chem. Phys. 20, 939.

Guderley, G., 1942, Luftfahrtforschung 19, 302.
Hallaj, I.M., T.J. Matula, R.A. Roy, and L.A. Crum, 1996, J. Acoust. Soc. Am. 100, 2717.
Hanbury-Brown, R., 1974, The Intensity Interferometer (Taylor & Francis, London).
Hansen, G.M., 1985, Appl. Opt. 24, 3214.
Harvey, E.N., 1957, A History of Luminescence from the Earliest Times until 1900 (Am. Phil.Soc. Press, Philadelphia).
Hickling, R., 1994, Phys. Rev. Lett. 73, 2853.
Hilgenfeldt, S., D. Lohse, and M.P. Brenner, 1996, Phys. Fluids 8, 2808.
Hiller, R.A., 1995, Ph.D. Thesis (University of California, Los Angeles).
Hiller, R. and B.P. Barber, 1995, Sci. Am. 272, 78.
Hiller, R.A. and S.J. Putterman, 1995, Phys. Rev. Lett. 75, 3549; 77, 2345 (E).
Hiller, R., S.J. Putterman, and B.P. Barber, 1992, Phys. Rev. Lett. 69, 1182.
Hiller, R., K. Weninger, S.J. Putterman, and B.P. Barber, 1994, Science 266, 248.
Holt, R.G., and L.A. Crum, 1992, J. Acoust. Soc. Am. 91, 1924.
Holt, R.G., D.F. Gaitan, A.A. Atchley, and J. Holzfuss, 1994, Phys. Rev. Lett. 72, 1376.
Holt, R.G. and D.F. Gaitan, 1996, Phys. Rev. Lett. 77, 3791.
van de Hulst, H.C., 1957, Light Scattering by Small Particles (Wiley, New York).
Jarman, P., 1960, J. Acoust. Soc. Am. 32, 1459.
de Jong, N., L. Hoff, T. Skotland, and N. Born, 1992, Ultrasonics 30, 95.
Kapitza, P.L., 1956, Collected Papers, edited by D. Ter Haar (Pergamon, New York).
Kerker, M., 1969, The Scattering of Light and Other Electromagnetic Radiation (Academic, NewYork).
King, L.V., 1934, Proc. Roy. Soc. A147, 212.
Kling, C.L. and F.G. Hammit, 1972, J. Basic. Eng, Trans. A.S.M.E. D94, 825.
Knight, P., 1996, Nature 381, 736.
Kondic, L., J.I. Gersten, and C. Yuan, 1995, Phys. Rev. E 52, 4976.
Kornfeld, M. and L. Suvorov, 1944, J. Appl. Phys. 15, 495.
Lamb, H., 1945, Hydrodynamics (Dover, New York).
Landau, L.D. and E.M. Lifshitz, 1976, Mechanics (Pergamon, Oxford).
Landau, L.D. and E.M. Lifshitz, 1987, Fluid Mechanics (Pergamon, Oxford).
Lauterborn, W. and H. Bolle, 1975, J. Fluid Mech. 72, 391.
Lentz, W.J., A. Atchley, and D.F. Gaitan, 1995, Applied Optics 34, 2648.
Lepoint, T., D. De Pauw, F. Lepoint-Mullie, M. Goldman, and A. Goldman, 1996, J. Acoust.Soc. Am. (in press).
Lohse, D., M.P. Brenner, T.F. Dupont, S. Hilgenfledt, and B. Johnston, 1996, "Single sonoluminescing bubbles as stable chemical reaction chambers".
Löfstedt, R., 1995, Ph.D. thesis (University of California, Los Angeles).
Löfstedt, R., B.P. Barber, and S.J. Putterman, 1992, J. Acoust. Soc. Am. 92, S2453.
Löfstedt, R., B.P. Barber, and S.J. Putterman, 1993, Phys. Fluids A 5, 2911.
Löfstedt, R. and S. Putterman, 1991, J. Acoust. Soc. Am. 90, 2027.
Löfstedt, R., K. Weninger, S. Putterman, and B.P. Barber, 1995, Phys. Rev. E 51, 4400.
Longuet-Higgins, M.S., 1996, J. Acoust. Soc. Am. 100, 2678.
Marston, P.L., 1979, J. Opt. Soc. Am. 69, 1205.
Marston, P.L., 1991, Appl. Opt. 30, 3479.
Matula, T.J., R.A. Roy, P.D. Mourad, W.B. McNamara, and K.S. Suslick, 1995, Phys. Rev. Lett. 75, 2602.
Moran, M.J., R.E. Haigh, M.E. Lowry, D.R. Sweider, G.R. Abel, J.T. Carlson, S.D. Lewis, A.A. Atchley, D.F. Gaitan, and X.K. Maruyama, 1995, Nucl. Instrum. Methods B96, 651.
Moss, W.C., J.W. White, R.A. Day, and D.B. Clarke, 1994, Phys. Fluids 6, 2979.
Noltingk, B. and E. Neppiras, 1950, Proc. Roy. Soc. B63, 674.
Penning, F.M. and C.C.J. Addink, 1934, Physica 1, 1007.
Picard, J., 1676, Mem. Acad. Roy. Science 2, 202.
Plesset, M., 1949, J. Appl. Mech. 16, 277.
Plesset, M.S. and T.P. Mitchell, 1956, Quart. Appl. Math. XIII, 419.
Pollack, G.L., J.F. Himm, and J.J. Enyeart, 1984, J. Phys. Chem. 81, 3239.
Prosperetti, A., 1977, Quart. Appl. Math. 34, 339.

Prosperetti, A., 1984, Rend. Sc. Int. Fis. XCIII, 145.
Prosperetti, A., 1996, "A new mechanism for sonoluminescence".
Prosperetti, A., L. Crum, and K. Commander, 1988, J. Acoust. Soc. Am. 83, 502.
Prosperetti, A. and G. Seminara, 1978, Phys. Fluids 21, 1465.
Putterman, S.J., 1995, Scientific American 272, 32.
Lord Rayleigh, 1883, Proc. London. Math. Soc. XIV, 170.
Lord Rayleigh, 1917, Phil. Mag. 34, 94.
Roberts, P.H. and S.J. Putterman, 1996, to be published.
Robinson Painter, L., R.D. Birkhoff, and E.T. Arakawa, 1969, J. Chem. Phys. 51, 243.
Schwinger, J., 1993, Proc. Natl. Acad. Sci. U.S.A. 90, 2105, 7285.
Stratton, J.A., 1941, Electromagnetic Theory (McGraw-Hill, New York).
Suslick, K.S. and E.B. Flint, 1987, Nature 350, 553.
Taylor, G.I., 1950, Proc. Roy. Soc. A201, 192.
Tian, Y.J., J.A. Ketterling, and R.E. Apfel, J. Acoust. Soc. Am. 100, 3976.
Tornow, W., 1996, Phys. Rev. E 53, 5495.
Trentalange S. and S.U. Pandey, 1996, J. Acoust. Soc. Am. 99, 2439.
Verrall, R. and C. Sehgal, 1987, Ultrasonics 25, 29.
Vuong, V.Q. and A.J. Szeri, Phys. Fluids 8, 2354.
Walton, A.J. and G.T. Reynolds, 1984, Adv. Phys. 33, 595.
Weninger, K., R. Hiller, B.P. Barber, D. Lacoste, and S.J. Putterman, 1995, J. Phys. Chem. 99, 14195.
Weninger, K., S.J. Putterman, and B.P. Barber, 1996, Phys. Rev. E. 54, R2205.
Wiedemann, E., 1889, Wiedemanns Ann. 37, 177.
Wiscombe, W.J., 1980, Appl. Opt. 19, 1505.
Wu, C.C. and P.H. Roberts, 1993, Phys. Rev. Lett. 70, 3424.
Wu, C.C. and P.H. Roberts, 1994, Proc. Roy. Soc. A445, 323.
Wu, C.C. and P.H. Roberts, 1996a, Phys. Lett. A 213, 59.
Wu, C.C. and P.H. Roberts, 1996b, Quart. J. Mech. Appl. Math. 49, 501.
Wu, J., R. Keolian, and I. Rudnick, 1984, Phys. Rev. Lett. 52, 1421.
Young, J.B., T. Schmiedel, and W. Kang, 1996, Phys. Rev. Lett. 77, 4816.